

Measurements of Upsilon Production in p+p, p+Au and Au+Au Collisions
at 200 GeV with the STAR Experiment

by

Zaochen Ye
B.A., Lanzhou University, 2010

THESIS

Submitted in partial fulfillment of the requirements
for the degree of Doctor of Philosophy in Physics
in the Graduate College of the
University of Illinois at Chicago, 2019

Chicago, Illinois

Defense Committee:
Zhenyu Ye (Chair and Advisor)
Olga Evdokimov
David Hofman
Ho-ung Yee
Zhangbu Xu (Brookhaven National Laboratory)

Copyright by

Zaochen Ye

2018

ABSTRACT

Quark-gluon plasma (QGP) is composed of deconfined quarks and gluons, a new state of matter, which is predicted to have existed a few millionth of a second after the Big Bang. Under normal conditions, due to the so-called “color confinement”, quarks and gluons are bound firmly as bound states such as mesons or baryons. However, at extremely high energies and densities, due to the small value of the running coupling of Quantum Chromodynamics (QCD), partons are only bound weakly so that they can move freely on their own. At the very initial times after the big bang, the temperature and energy density was extremely high, the universe was in a state of QGP where all quarks and gluons were deconfined and fly at nearly the speed of light. Today, such an extreme state of matter can be achieved experimentally at Relativistic Heavy-Ion Collider (RHIC) and Large Hadron Collider (LHC).

Measurements of quarkonium production are an important tool to study the properties of the Quark-Gluon Plasma (QGP) formed in relativistic heavy-ion collisions. Quarkonium suppression due to the color-screening effect was proposed as a direct evidence of the QGP formation [1]. Moreover, different quarkonium states may dissociate at different temperatures depending on their binding energies. This so-called sequential melting phenomenon can help constrain the temperature of the QGP. However, other effects, such as cold nuclear matter effects and regeneration, add additional complications to the interpretation of the observed suppression. Compared to charmonia, bottomonia is much less affected by regeneration contribution at RHIC energies, making them a cleaner probe to the QGP. In this thesis, the bottomonium

(Upsilon) productions are studied in p+p, p+Au and Au+Au collisions at a center of mass energy per nucleon pair of 200 GeV with the STAR experiment. In p+p and p+Au collisions, the differential production cross section and nuclear modification factor R_{pAu} as a function of transverse momentum p_T or rapidity y , are measured for $0 < p_T < 10$ GeV/c and $|y| < 1$. A significant suppression of Υ meson production in p+Au collisions with respect to p+p collisions is observed. In Au+Au collisions, the nuclear modification factor R_{AA} as a function of p_T or centrality are measured for $0 < p_T < 10$ GeV/c and centrality 0-60%. The suppression of Υ at semi-central and central collisions is stronger than peripheral collisions. The $\Upsilon(2S + 3S)$ are observed to be more suppressed than $\Upsilon(1S)$ in the most central collisions which is consistent with “sequential melting” expectation. These results are also compared to theoretical model predictions and to the experimental results from LHC energies.

(Part of results in this thesis were previously published by Zaochen Ye, “ Υ measurements in p+p, p+Au and Au+Au collisions at $\sqrt{s_{NN}} = 200$ GeV with the STAR experiment”, Nuclear Physics A, 967 (2017) 600-603.)

ACKNOWLEDGMENT

During my Ph.D life, there are so many people who have helped me, supported me or encouraged me. I would like to express my sincere gratitude to all of them.

Firstly, I would like to thank my advisor Prof. Zhenyu Ye for his continuous support for my Ph.D study and research, also for his patience and motivation. He leads me to the high energy nuclear physics and guided me in all the time of my research. Without his guidance, I cannot finish my Ph.D thesis. Besides my advisor, I would like to thank the rest of my thesis committee: Prof. Evdokimov, Prof. Hofman, Prof. Yee and Prof. Xu, for their insightful comments and encouragement, and also for their valuable suggestions for my future academic career.

My sincere thanks also goes to Dr. Bingchu Huang, Dr. Shuai Yang, Dr. Kolja Kauder who taught me a lot of knowledge about the data analysis techniques and detectors. I would also like to thank Dr. Jinlong Zhang, Dr. Long Zhou, Dr. Rongrong Ma, Dr. Takhito Todoroki, Dr. Hongwei Ke, Dr. Yi Guo, Dr. Wangmei Zha and other STAR collaborators for sharing their experiences with me. I would like to thank the UIC Heavy-Ion group: Dr. Zach Miller, Dr. Kurt Jung, Dr. Guannan Xie, Xiao Wang, Siwei Luo, Dhanush Hangal, Xiaozhi Bai (visiting student) and Shenghui Zhang (visiting student) for their discussion and company, working together with them is full of fun. I also would like to thank several UIC students: Bo Ling, Xuan Hu, Peihong Man and Shiyong Li, we had a lot of wonderful times and happy memories in the past 6 years, we always take care of each other like a big family.

Last but not the least, I must express my very profound gratitude to my family. I would like to thank my parents for providing me with unfailing support, endless love and continuous encouragement throughout all my life. I would like to thank my wife for encouraging and supporting me to follow my dreams and specially thank her for taking care of our dear daughter without any complain. Without their support, I would never be the person I am today.

Regards,

Zaochen Ye

TABLE OF CONTENTS

<u>CHAPTER</u>		<u>PAGE</u>
	Abstract	iii
1	INTRODUCTION	1
1.1	Elementary Particles and Fundamental Interactions in the Standard Model	1
1.2	Quantum Chromodynamics (QCD) and the Quark-Gluon Plasma (QGP)	6
1.2.1	Asymptotic Freedom and Confinement in QCD	8
1.2.2	Features of QGP in Perturbative QCD	10
1.2.3	Phase Transition in Lattice QCD Calculation	11
1.3	Study QGP via High Energy Heavy Ion Collisions	16
1.4	Quarkonium Suppression as a Probe of QGP	19
1.4.1	Quarkonium Production Mechanism	21
1.4.2	Physics of Quarkonium Suppression	26
1.5	Goal this Thesis	37
1.5.1	Previous Measurements	37
2	EXPERIMENTAL SETUP	41
2.1	Relativistic Heavy Ion Collider (RHIC)	41
2.2	Solenoidal Tracker at RHIC (STAR)	45
2.2.1	Time Projection Chamber (TPC)	47
2.2.2	Time-of-Flight Detector (TOF)	55
2.2.3	Barrel Electromagnetic Calorimeter (BEMC)	58
2.2.4	Heavy Flavor Tracker (HFT)	62
2.2.5	Muon Telescope Detector (MTD)	64
2.2.6	Vertex Position Detector (VPD)	65
2.2.7	Beam-Beam Counter (BBC)	66
3	MEASUREMENTS OF UPSILON PRODUCTION IN P+P AND P+AU COLLISIONS	68
3.1	Upsilon Invariant Mass Reconstruction in Real Data	68
3.1.1	Data Sets	68
3.1.2	Event Selection	69
3.1.3	Track Selection	70
3.1.4	Electron Track Selection	70
3.1.5	Make Electron Pairs	72
3.2	Efficiency Studies	73
3.2.1	Single Electron Reconstruction Efficiency	73

TABLE OF CONTENTS (Continued)

<u>CHAPTER</u>		<u>PAGE</u>
3.2.2	Momentum Resolution	77
3.2.3	Upsilon Reconstruction Efficiency	83
3.2.4	Upsilon Templates from Smearing	84
3.2.5	Physics Background Shapes of $B\bar{B}$ and Drell-Yan from Simulation	86
3.3	Upsilon Yields Extraction	88
3.3.1	Upsilon Signals in Run15 pp	91
3.3.2	Upsilon Signals in Run15 pAu	92
3.4	Number of Equivalent MB Events and Trigger Bias Calculation	93
3.4.1	Number of Equivalent MB Events Based on BBCMB	94
3.4.2	In Bunch Pileup Effects Study	98
3.4.3	Trigger Bias Factors (TB) are Studied from Simulation	102
3.4.3.1	Trigger Bias Factor in Run15 pp	102
3.4.3.2	Trigger Bias factor in Run15 pAu	107
3.4.4	A Summary for Number of equivalent MB events and Trigger Bias Factor	112
3.5	Systematic uncertainties of Υ measurements in Run15 pp and pAu	113
3.5.1	Systematic uncertainties of Υ cross section measurements in Run15 pp	115
3.5.2	Systematic uncertainties of Υ invariant yield measurements in Run15 pAu	116
3.5.3	Systematic uncertainties of ΥR_{pA} measurements	117
4	MEASUREMENTS OF UPSILON PRODUCTION IN AU+AU COLLISIONS	120
4.1	Data Sets	120
4.1.1	Event Selection	120
4.1.2	Electron track selection	124
4.2	Efficiency Study with Embedding Samples	124
4.2.1	Single Electron Reconstruction Efficiency	124
4.2.2	Momentum Resolution	128
4.2.3	Upsilon Reconstruction Efficiency	129
4.2.4	Upsilon Templates from Smearing	130
4.2.5	Physics background shapes of $B\bar{B}$ and Drell-Yan from simulation	132
4.3	How to Extract the Upsilon Signal Yields	133
4.3.1	Fitting Methods	133
4.4	Number of Equivalent MB Events	134
4.5	Upsilon Signals from Fitting	137
4.6	Systematic Uncertainties of Υ Measurements in Run11 AuAu	139
4.6.1	Systematic Uncertainties of ΥR_{AA} Measurements	143
4.7	Physics Results	145
4.7.1	Physics Results Measured in $\Upsilon \rightarrow e^+e^-$ Decay Channel	147

TABLE OF CONTENTS (Continued)

<u>CHAPTER</u>		<u>PAGE</u>
4.7.2	Cross-check between “di-electron” and “di-muon” analysis . .	150
5	PHYSICS RESULTS SUMMARY AND DISCUSSION <i>(PART OF RESULTS IN THIS CHAPTER WERE PREVIOUSLY PUBLISHED BY ZAOCHEN YE FOR STAR COLLABORATION, “γ MEASUREMENTS IN P+P, P+AU AND AU+AU COLLISIONS AT $\sqrt{s_{NN}} = 200$ GEV WITH THE STAR EXPERIMENT,” NUCL. PHYS. A 967, 600 (2017)), THESE RESULTS ARE ALSO PRESENTED IN OUR STAR COLLABORATOR-XINJIE HUANG AND WANGMEI ZHA’S SQM CONFERENCE PROCEEDINGS AT EPJ WEB OF CONFERENCES.</i>	
	152
5.1	Upsilon Cross section in p+p and Invariant Yield in p+Au . .	153
5.1.1	Nuclear Modification Factor	156
6	CONCLUSIONS	169
	APPENDIX	171
	CITED LITERATURE	174

LIST OF TABLES

<u>TABLE</u>		<u>PAGE</u>
I	Mass (m), binding energy (E_{bd}) and radius (r) of quarkonium states [32].	27
II	The total recorded luminosity and number of events triggered by BHT2*BBCMB in 2015 p+p and p+Au collisions.	68
III	Number of BHT2*BBCMB events corresponding to different requirements in 2015 p+p and p+Au collisions.	69
IV	Υ detection efficiency in different rapidity ranges with p_T integrated over $0 < p_T < 10$ Gev/c for Run15 pp and pAu.	83
V	Υ detection efficiency in different p_T ranges with rapidity integrated over $ y < 1.0$ and $ y < 0.5$ for Run15 pp and Run15 pAu. . .	84
VI	Number of equivalent BBCMB events of Run15 pp and Run15 pAu corresponding the analyzed BHT2*BBCMB events. $N_{MB}^{eqv.}$ (on-line) is the number of equivalent BBCMB events corresponding to the number of BHT2 evnets N_{BHT2} (on-line). N_{BHT2} (Ana.) is number of BHT2 events ($ Vz < 200$ cm) used for the Upsilon signal extraction. $N_{MB}^{eqv.}$ is the number of equivalent BBCMB events before the in bunch pile-up correction.	97
VII	The average value of λ , $Frac[k = 2]$ and the final number of equivalent MB events $N_{MB}^{eqv.}$ (final) of Run15 pp and pAu.	102
VIII	Run15 pp BBC single fire and double fire efficiency, the statistical uncertainty of these efficiency values is ~ 0.001	103
IX	Run15 pp BBC efficiencies for $K=1$ and $K=2$, the statistical uncertainty of these efficiency values is ~ 0.001	104
X	The average value of BBC efficiency and good Vertex efficiency for MBonly, J/ψ , Υ , D_0 events for Run15 pp. (The statistical uncertainty of these efficiency values is ~ 0.001 , so can be ignored.)	106
XI	Run15 pp Trigger Bias $\frac{\langle \epsilon_{MB}^{BBC} \rangle \langle \epsilon_{MB}^{goodvtx} \rangle}{\langle \epsilon_{Particle}^{BBC} \rangle \langle \epsilon_{Particle}^{goodvtx} \rangle}$	106
XII	Run15 pAu BBC single fire and double fire efficiency(The statistical uncertainty is 0.001, thus can be ignored.)	107
XIII	Run15 pAu BBC efficiencies for $K=1$ and $K=2$	109
XIV	The average value of BBC efficiency and good Vertex efficiency for MBonly and D_0 events for Run15 pAu.	110
XV	The estimated average values and uncertainties of BBC efficiency and good Vertex efficiency for J/ψ and Υ events for Run15 pAu. (The systematic uncertainty is estimated by $\pm(\text{UpLimit} - \text{LowLimit})/2$)	111

LIST OF TABLES (Continued)

<u>TABLE</u>		<u>PAGE</u>
XVI	Trigger Bias $\frac{\langle \epsilon_{MB}^{BBC} \rangle \langle \epsilon_{MB}^{goodvtx} \rangle}{\langle \epsilon_{particle}^{BBC} \rangle \langle \epsilon_{particle}^{goodvtx} \rangle}$ for D_0 , J/ψ and Υ measurements in Run15 p+Au collisions. (The systematic uncertainty of trigger bias factors propagated from the systematic uncertainty of BBC efficiency and good Vertex efficiency are listed in the second row. The final systematic uncertainty of Trigger Bias factor also take into account the uncertainty of 3% from different Pythia versions, are listed in the last row.)	112
XVII	The final number of equivalent MB events, good vertex efficiency and the trigger bias factor for J/ψ and Υ measurements with Run15 pp and pAu BHT2*BBCMB triggered data.	112
XVIII	Number of NPE18 triggered events in Run11 AuAu data	121
XIX	The average number of participants ($\langle N_{part} \rangle$) and the average binary collisions ($\langle N_{coll} \rangle$) in different centrality bins [76].	122
XX	The reconstruction efficiency of $\Upsilon(1S)$, $\Upsilon(2S)$, $\Upsilon(3S)$ in centrality bins of 0-10%, 10-30%, 30-60% and 0-60%. For rapidity integrated within $ y < 1$ and p_T integrated over $0 < p_T < 10$ GeV/c.	130
XXI	The reconstruction efficiency of $\Upsilon(1S)$, $\Upsilon(2S)$, $\Upsilon(3S)$ in different p_T bins. For rapidity integrated within $ y < 1$ and centrality integrated over 0-60%.	130
XXII	The number of equivalent MB events corresponding to the analyzed NPE18 triggered events in 2011 Au+Au collisions at $\sqrt{s_{NN}} = 200$ GeV.	137

LIST OF FIGURES

<u>FIGURE</u>		<u>PAGE</u>
1	A summary of elementary particles as well as the fundamental forces in the Standard Model. For each particle, its mass, charge and spin values are listed in colored box. The three generations of quarks are shown in blue: (u, d), (c, s), (t, b). The three leptons and their associated neutrinos are in green: (e, ν_e), (μ , ν_μ), (τ , ν_τ). All quarks and leptons are Fermions while gluons, photons, W^\pm and Z are Bosons, which act as force carriers, are shown in red. The recently discovered Higgs boson, the so called “god particle” is shown in yellow at the top right. Three black open squares enclose those particles which could participate the corresponding fundamental forces. This figure is cited from sciencesptrings [2]	3
2	A diagram summarizing the tree-level interactions between elementary particles in the Standard Model. Photon, W^\pm and Z bosons are the force mediating particles. Higgs boson generate the mass of elementary particles. This figure is cited from wikipedia [3]	5
3	An illustration of the expansion of the universe. According to the Big Bang theory, the universe expanded and cooled down shortly after the Big Bang. After $\sim 10^{-6}$ seconds, the universe experienced a state of Quark-Gluon Plasma (QGP) where all quarks and gluons are de-confined. When the temperature of Universe (T_{universe}) cooled down to $\sim 10^{12}$ K, quarks coalesced into protons and neutrons. As time progressed, the light nucleus such as deuterium, helium and lithium were formed by protons and neutrons. Then, electrons, protons and neutrons formed low-mass neutral atoms. As clouds of atoms attracted each other through gravity and formed initial stars, where more massive elements can be fused by hydrogen and helium. The most massive elements of the universe were formed from the explosion of stars. After the explosion, massive debris dispersed into space, among which, our earth was formed. The figure is cited from [4]	7
4	The running coupling constant in QCD as a function of the energy scale from both experimental and theoretical studies. This figure is cited from [6]	9
5	A thermodynamic quantity ϵ/T^4 as a function of temperature T/T_C predicted by the lattice QCD calculations (simulations) [7] These calculations are carried out with three different flavor combinations: 3 light flavors, 2 light flavors + 1 heavy flavor, 2 light flavors.	12

LIST OF FIGURES (Continued)

<u>FIGURE</u>		<u>PAGE</u>
6	The pressure of the system as a function of temperature predicted by the lattice QCD calculations (simulations) [7]. These calculations are done with four different cases: 3 light flavors, 2 light flavors + 1 heavy flavor, 2 light flavors, pure gauge.	13
7	The chiral symmetry restoration and deconfinement calculated by lattice QCD [7]. The left panel shows order parameter $\langle \bar{\psi}\psi \rangle$ (blue curve) for chiral symmetry breaking with while $m_q \rightarrow 0$ (chiral limit). The right panel shows the order parameter of $\langle L \rangle$ (blue curve) for deconfinement while $m_q \rightarrow \infty$ (pure gauge limit). Also shown in the two figures are their corresponding susceptibilities as a function of coupling coefficient $\beta = 6/g^2$	15
8	An illustration of system evolution in relativistic heavy-ion collisions [8].	16
9	An illustration of the relationship between the measured charged particle multiplicity N_{ch} , the impact parameter b , the average number of participating nucleons N_{part} and the centrality in percentage. This figure is cited from [19]	18
10	The charmonium family feed-down pattern [20]. (Those “X” states are experimental observed particles but their nature is still unknown.)	20
11	The bottomonium family feed-down pattern [20]. (Dashed bold lines denote unconfirmed states)	21
12	An illustration of sequential suppression pattern of charmonium states (left) and bottomonium states (right) [32].	28
13	A summary of quarkonium dissociation temperatures T_{diso} predicted from different theoretical calculation [33] . The horizontal bars denote a temperature ranges where the quarkonium state experiencing a mass or size evolution. Quarkonium states are predicted to completely melt when temperatures are above the right end of the bars.	29
14	An illustration of J/ψ production probability (thermal dissociation and regeneration) as a function of energy density [32].	31
15	An illustration [36] of nuclear shadowing function R_i^A . Where, y_0 is the value shadowing level goes to as $x \rightarrow 0$; x_a , y_a are the coordinates of the anti-shadowing maximum ; x_e , y_e are coordinates of the EMC minimum.	33
16	The EPS09 [36] nuclear modifications for Lead at the parameterization scale $Q^2 = 1.69 \text{ GeV}^2$ (upper) and $Q^2 = 100 \text{ GeV}^2$ (bottom). The left, central and right columns are corresponding to the valence quarks, sea quarks and gluons, respectively. Where the best-fit results are shown in black lines, the error sets are shown in dotted green curves.	34

LIST OF FIGURES (Continued)

<u>FIGURE</u>		<u>PAGE</u>
17	The left panel shows the Υ R_{AA} as a function of centrality (or N_{part}) measured in Pb+Pb collisions at $\sqrt{s_{NN}} = 2.76$ TeV by CMS [43,44] and ALICE experiments [45]. The right panel shows the ratios of $\Upsilon(2S)$, $\Upsilon(3S)$ over $\Upsilon(1S)$ measured in p+p ($\sqrt{s} = 2.76$ TeV), p+Pb ($\sqrt{s} = 5.02$ TeV), Pb+Pb ($\sqrt{s} = 2.76$ TeV) collisions by CMS experiment [46]. . .	38
18	The left panel shows the $R_{AA}^{\Upsilon(1S+2S+3S)}$ and $R_{AA}^{\Upsilon(1S)}$ measured in Au+Au [47] [33] ($\sqrt{s_{NN}} = 200$ GeV), U+U [48] ($\sqrt{s_{NN}} = 193$ GeV) collisions at RHIC compared to that from CMS experiment at LHC [44]. The right panel shows the $R_{dAu}^{\Upsilon(1S+2S+3S)}$ measured at RHIC [47] [49] compared different model calculations.	40
19	The pre-injection facility of the Tandem Van de Graaff (Tandem), the Electron Beam Ion Source (EBIS) and the BNL Linear Accelerator (Linac) [50].	42
20	The Relativistic Heavy-Ion Collider (RHIC) and its complex supporting infrastructure [51].	44
21	The left panel is the twin accelerators of RHIC [52], and the right panel is the Arc dipole coil and yoke, the curves are illustration of magnetic flux lines [53].	45
22	STAR detectors [54].	46
23	The schematic view of Time Projection Chamber (TPC) [55]. . . .	47
24	Drift velocity versus the reduced electric field E/p ($E \sim$ electric field, $p \sim$ gas pressure) [55].	49
25	One anode pad sector of TPC. The full sector contains the inner subsector (1,750 smaller pads) and out subsector (3,942 larger pads) [56].	51
26	A side view of an TPC outer sub-sector pad plane. It shows the spacing of the anode wires relative to the gated grid, the ground shield grid and the pad plane. The additional details about the wire spacing are shown in bubble diagram. (All dimensions are draw in millimeters) [56].	53
27	The truncated mean of the ionization energy loss $\langle dE/dx \rangle$ versus the rigidity p/q (p is the momenta, q is the charge) of different particles measured by TPC in Au+Au collisions at $\sqrt{s_{NN}} = 200$ GeV [60]. . . .	55
28	The front and back side views of Multi-gap Resistive Plate Chamber (MRPC) module [62,63]. The STAR barrel Time-of-Flight detector (TOF) are comprised of MRPC modules.	56
29	The inverse velocity $1/\beta$ measured by STAR TOF detector versus the rigidity p/q in Au+Au collisions at $\sqrt{s_{NN}} = 200$ GeV [60].	58
30	The perspective view of the Barrel Electromagnetic Calorimeter (BEMC) [64].	59
31	The side view (left) and end view (right) of a single BEMC module [64].	60
32	The side view of a single BEMC tower [64].	61

LIST OF FIGURES (Continued)

<u>FIGURE</u>		<u>PAGE</u>
33	STAR Heavy Flavor Tracker (HFT) [65].	63
34	The performance of STAR HFT [66]. The left panel shows the transverse DCA of π^\pm measured by STAR compared to that from LHC experiments. The right panel shows the invariant mass of D^0 reconstructed in 2014 Au+Au collisions at $\sqrt{s_{NN}} = 200$ GeV. The small box shows the comparison of D^0 signals reconstructed with and without HFT.	63
35	STAR Muon Telescope Detector (MTD) [67]. The MTD tray is installed on top of the BEMC electronic boxes. The right figure shows the schematic view of MTD system.	64
36	STAR Vertex Position Detector (VPD) [68].	65
37	STAR Beam Beam Counter (BBC) [69].	67
38	The left panel shows an example of $n\sigma_e$ distribution of photonic electrons within a transverse momentum window: $4.0 < p_T < 4.5$ GeV/c. The black points corresponds to the unlike-sign pairs, the red points corresponds to the like-sign pairs, the purple points are obtained by subtracting the like-sign distribution from the unlike-sign distribution. The right panel shows the fitted mean and width (sigma) of $n\sigma_e$ distributions as a function of p_T	75
39	An example of single electron reconstruction efficiency as a function of p_T in Run15pp (left) and Run15pAu (right) within a pseudorapidity window of $0.2 < \eta < 0.4$	77
40	The top left panel shows the momentum resolution $\sigma(\frac{\delta p_T}{p_T})$ as function of p_T , fitted with a function of $f(p_T) = \sqrt{a^2(p_T)^2 + b^2}$. The top right panel shows the normalized $\delta p_T/p_T$ fitted by Double Crystal Ball function. The bottom panel shows the tuning of parameter “a” to best match the J/ψ width in Run15 pp and Run15 pAu BHT2 triggered data (The solid line is the fitted J/ψ width and the dotted lines shows the uncertainty of the fitted J/ψ width. The J/ψ p_T range is 4-10 GeV/c).	80
41	Comparison of smeared J/ψ to real data of 2015 pp and 2015 pAu	82
42	Υ templates for Run15 pp	85
43	Υ templates for Run15 pAu	86
44	Background shapes of $B\bar{B}$ and Drell-Yan from Simulation	87
45	Upsilon signals in Run15 pp. The top three panels are Upsilon signals in different rapidity bins: $ y < 1$, $ y < 0.5$, $0.5 < y < 1$ with p_T integrated over $0 < p_T < 10$ GeV/c; The bottom three panels are Upsilon signals in different p_T bins: $0 < p_T < 2$ GeV/c, $2 < p_T < 4$ GeV/c, $4 < p_T < 10$ GeV/c with rapidity integrated over $ y < 1$	91

LIST OF FIGURES (Continued)

<u>FIGURE</u>		<u>PAGE</u>
46	Upsilon signals in Run15 pAu. The top panel is the inclusive Upsilon signal. The middle three panels are Upsilon signals in different rapidity bins: $ y < 0.5$, $0.5 < y < 1$, $-1 < y < -0.5$ with p_T integrated over $0 < p_T < 10$ GeV/c; The bottom three panels are Upsilon signals in different p_T bins: $0 < p_T < 2$ GeV/c, $2 < p_T < 4$ GeV/c, $4 < p_T < 10$ GeV/c with rapidity integrated over $ y < 1$	92
47	The left panel shows the TPC V_z distributions of BBCMB and BHT2*BBCMB events in Run15 p+p data. The right panel shows the ratio of reconstructed V_z over MC V_z ($\frac{rcV_z}{mcV_z}$) from the PYTHIA8+GEANT+ZeroBias simulation for Run15 pp.	94
48	The left panel shows the TPC V_z distributions of BBCMB and BHT2*BBCMB events in Run15 p+Au data. The right panel shows the ratio of reconstructed V_z over MC V_z ($\frac{rcV_z}{mcV_z}$) from the PYTHIA8+GEANT+ZeroBias simulation for Run15 pAu.	95
49	The left panel shows the TPC V_z (ranking > 0) distributions of Run15pp BBCMB events corrected by the efficiency shown in right panel of Figure 47. The right panel shows the TPC V_z (ranking > 0) distributions of Run15pAu BBCMB events corrected by the efficiency shown in right panel of Figure 48.	96
50	The number of equivalent BBCMB events vs RunId (Run number) corresponding to the BHT2*BBCMB events in Run15 pp and Run15 pAu.	96
51	The λ and fraction[k = 2] distribution in Run15 p+p (top two panels) and pAu (bottom two panels) BBCMB events. Each entry of the histogram is corresponding to one run.	101
52	Efficiency corresponding to the following cuts: $dV_zCut = " mcV_z - rcV_z < 1.5 \text{ cm} "$, RankingCut = "ranking > 0 ", good Vertex = "dV_z-Cut*RankingCut", BBCAnd = "BBC both sides fired" for MBonly events and J/ ψ or Υ events are calculated and compared in the figures.	105
53	BBC efficiency and the good vertex efficiency in J/ ψ and Υ events.	105
54	Efficiencies comparison between MB-only events and D_0 events with different cuts in the Hijing+GEANT+ZeroBias simulation	108
55	Systematic uncertainties from different sources for $\Upsilon(1S+2S+3S)$ cross section as function of p_T in Run15pp within rapidity ranges: $ y < 1$, $ y < 0.5$, $0.5 < y < 1$	116
56	Systematic uncertainties from different sources for $\Upsilon(1S+2S+3S)$ invariant yield as function of p_T measurement in Run15pAu within rapidity ranges: $ y < 1$, $ y < 0.5$, $0.5 < y < 1$	117
57	Systematic uncertainties from different sources for R_{pA} of $\Upsilon(1S+2S+3S)$ as function of p_T within rapidity ranges: $ y < 1$, $ y < 0.5$, $0.5 < y < 1$, and $-1.0 < y < -0.5$	119

LIST OF FIGURES (Continued)

<u>FIGURE</u>		<u>PAGE</u>
58	The left panel shows V_z^{TPC} distribution and the right panel shows the difference between V_z^{TPC} and V_z^{VPD} of NPE18 triggered events in Run11 AuAu data.	121
59	The black line shows the multiplicity distribution in TPC for NPE18 triggered events in Run11 AuAu data, and the blue line shows the corrected multiplicity distribution in TPC based on the Glauber Monte Carlo simulation.	123
60	The centrality distribution and the re-weighted centrality distribution of NPE18 triggered events in Run11 AuAu data	123
61	The fitted mean and width of $n\sigma_e$ as function of p_T in Run11 AuAu 200 GeV data	125
62	Efficiencies of single electron as function of p_T corresponding to different requirements (“TPC”, “EMC”, “Trg BHT2”) in different centralities of Run11 200 GeV AuAu data.	127
63	The top left panel shows the momentum resolution $\sigma(\frac{\delta p_T}{p_T})$ as function of p_T , fitted with a function of $f(p_T) = \sqrt{a^2(p_T)^2 + b^2}$. The top right panel shows the normalized $\delta p_T/p_T$ fitted by Double Crystal Ball function. The bottom panel shows the tuning of parameter “a” to best match the J/ψ mass width in Run11 AuAu BHT2 triggered data (The solid line is the fitted J/ψ width and the dotted lines shows the uncertainty of the fitted J/ψ width. The J/ψ p_T range is 4-10 GeV/c).	128
64	Comparison of smeared J/ψ to real data in Run11 200 GeV AuAu data.	129
65	$\Upsilon(1S)$, $\Upsilon(2S)$, $\Upsilon(3S)$ templates for 0-60% centrality of Run11 AuAu	131
66	Background shapes of $B\bar{B}$ and Drell-Yan from PYTHIA simulation with all efficiency of single electron embedded.	132
67	The centralities versus the number of ZDC MB events corresponding to the NPE18 triggered events in each run, before (left panel) and after (right panel) the pre-scale and live time correction.	135
68	The number of ZDC MB events corresponding to the NPE18 triggered events in each run, before (left panel) and after (right panel) the pre-scale and live time correction, for all centralities.	136
69	The invariant mass distribution of reconstructed Υ candidates, unlike-sign electron pairs (US) subtracted by like-sign electron pairs (LS), in different centrality bins of 0-60%, 30-60%, 10-30%, 0-10% with p_T integrated over $0 < p_T < 10$ and rapidity integrated over $ y < 1$ in 2011 Au+Au collisions at $\sqrt{s_{\text{NN}}} = 200$ GeV.	138

LIST OF FIGURES (Continued)

<u>FIGURE</u>		<u>PAGE</u>
70	The invariant mass distribution of reconstructed Υ candidates, unlike-sign electron pairs (US) subtracted by like-sign electron pairs (LS), in different p_T bins: $0 < p_T < 10$, $0 < p_T < 2$, $2 < p_T < 4$, $4 < p_T < 10$ GeV/c with centrality integrated over 0-60% and rapidity integrated over $ y < 1$ in 2011 Au+Au collisions at $\sqrt{s_{NN}} = 200$ GeV.	139
71	Systematic uncertainties from different sources for the invariant yields of $\Upsilon(1S+2S+3S)$, $\Upsilon(1S)$, $\Upsilon(2S+3S)$ and the Ratio of $\frac{2S+3S}{1S}$ as a function of p_T in 0-60% centrality within rapidity ranges: $ y < 1$ in 2011 Au+Au collisions	142
72	Systematic uncertainties from different sources for R_{AA} of $\Upsilon(1S+2S+3S)$, $\Upsilon(1S)$, $\Upsilon(2S+3S)$ as a function of p_T in 0-60% centrality within rapidity ranges: $ y < 1$ from 2011 Au+Au collisions and 2015 p+p collisions	145
73	The nuclear modification factor R_{AA} of $\Upsilon(1S)$, $\Upsilon(2S+3S)$, $\Upsilon(1S+2S+3S)$ (the first 3 panels) and the ratio (the last panel) of excited Upsilon states over ground state as a function of p_T with rapidity integrated over $ y < 1$ and centrality integrated over 0-60% are shown in red solid stars. The red open stars represent for the p_T integrated results. The vertical bar and the horizontal bar around each data point denote the bin width and statistical uncertainty of that point. The systematic uncertainties of each data point are drawn in red open boxes around the data points. The red solid box around the unity represents the common normalization uncertainty.	148
74	The nuclear modification factor R_{AA} of $\Upsilon(1S)$, $\Upsilon(2S+3S)$, $\Upsilon(1S+2S+3S)$ (the first 3 panels) and the ratio (the last panel) of excited Upsilon states over ground state as a function of N_{part} with rapidity integrated over $ y < 1$ and p_T integrated over $0 < p_T < 10$ GeV/c are shown in red solid stars. The red open stars stand for the results of 0-60% centrality. The vertical bar around each data point represent the statistical uncertainty of that point. The systematic uncertainties of each data point are drawn in red open boxes around the data points, where the systematic uncertainty from N_{coll} is drawn separately in gray solid boxes. The red solid box around the unity represents the common normalization uncertainty.	149

LIST OF FIGURES (Continued)

<u>FIGURE</u>		<u>PAGE</u>
75	<p>The comparison of Upsilon ground state and the excited states. The left panel is the R_{AA} of $\Upsilon(1S)$ and $\Upsilon(2S + 3S)$ as a function of N_{part} with rapidity integrated over $y < 1$ and centrality integrated over 0-60%. The right panel is ratio of $\Upsilon(2S + 3S)$ over $\Upsilon(1S)$ as a function of N_{part} with rapidity integrated over $y < 1$ and p_T integrated over $0 < p_T < 10$ GeV/c. The red open stars stand for the centrality integrated results. The vertical bar around each data point represent the statistical uncertainty of that point. The systematic uncertainties of each data point are drawn in red open boxes around the data points, where the systematic uncertainty from N_{coll} is drawn separately in gray solid boxes. The red solid box around the unity represents the common normalization uncertainty.</p>	150
76	<p>The left panel shows the comparison of R_{AA}^{1S} between di-electron (blue stars) and di-muon (red stars) analysis, the red solid box around unity line denotes the common normalization uncertainty. The right panel shows the comparison of ratio $\frac{\Upsilon(2S+3S)}{\Upsilon(1S)}$ between di-electron and di-muon analysis, the down arrows represent the upper limit with a confidence level of 90%. The open boxes around data points denote the systematic uncertainty and the gray solid boxes denote the systematic uncertainty coming from the $\langle N_{coll} \rangle$.</p>	151
77	<p>$\Upsilon(1S+2S+3S)$ cross section (red star) in 2015 p+p collisions at $\sqrt{s} = 200$ GeV is compared to STAR published result (open star), the preliminary result in p+p collisions (blue star) at $\sqrt{s} = 500$ GeV, the world-wide experimental data and the theoretical curve predicted by the NLO CEM calculaton [79]. (The previous published data from STAR collaboration are also compared to the world-wide data in PHYSICAL REVIEW D 82, 012004 (2010). This figure is also shown in the previous publication by Xinjie Huang, on EPJ Web of Conferences 171, 18015 (2018)) . . .</p>	154
78	<p>$\Upsilon(1S + 2S + 3S)$ cross section (red stars) as a function of transverse momentum (left) and rapidity (right) in 2015 p+p collisions at $\sqrt{s} = 200$ GeV are compared to the pQCD Color Evaporation Model (CEM) calculations (blue bands) [79] . The cross section of $\Upsilon(1S + 2S + 3S)$ as a function of p_T is measured within a rapidity range of $y < 1$. While the results in rapidity ranges of $0.5 < y < 1.0$ and $-1.0 < y < -0.5$ are combined as $0.5 < y < 1$, the open circle in $-1.0 < y < -0.5$ is the mirror image point of $0.5 < y < 1$. The vertical and horizontal bar around data points denotes the statistical uncertainty and the bin with, respectively. The azure boxes around data points represent the systematic uncertainty.</p>	155

LIST OF FIGURES (Continued)

<u>FIGURE</u>		<u>PAGE</u>
79	<p>$\Upsilon(1S+2S+3S)$ invariant yield as a function of transverse momentum (left) and rapidity (right) in 2015 p+Au collisions at $\sqrt{s} = 200$ GeV are shown in red stars. The vertical and horizontal bar around data points denotes the statistical uncertainty and the bin with, respectively. The azure boxes around data points represent the systematic uncertainty.</p>	156
80	<p>The nuclear modification factor R_{pAu} of $\Upsilon(1S+2S+3S)$ as a function of transverse momentum (left) and rapidity(right). The vertical and horizontal bar around data points denotes the statistical uncertainty and the bin with, respectively. The azure boxes around data points represent the systematic uncertainty. The red band on the right side around unity represents the common normalization uncertainties.</p>	157
81	<p>The R_{pAu} of $\Upsilon(1S+2S+3S)$ as a function of p_T and y from our measurements (red stars) are compared to results from ATLAS experiment [80] (open circles) measured in p+Pb collisions at $\sqrt{s_{NN}} = 5.02$ TeV within a rapidity range of $-2 < y < 1.5$. The boxes around data points represent the systematic uncertainty.The colored bands on the right side around unity represent the common normalization uncertainties.</p>	158
82	<p>The cold nuclear modification factor R_{pA} of $\Upsilon(1S+2S+3S)$ as function of p_T from our measurements at 200 GeV are shown in red stars, and compared to results from ALICE experiment (filled squares for $-4.46 < y < -2.96$ and open squares for $2.03 < y < 3.53$) at $\sqrt{s_{NN}} = 8.16$ TeV [81], the shaded boxes around data points represent the systematic uncertainty.The colored bands on the right side around unity represent the common normalization uncertainties.</p>	159
83	<p>The new R_{pAu} (red stars) of $\Upsilon(1S+2S+3S)$ as a function of transverse momentum are compared to the theoretical prediction based on EPS09 nPDF done by R. Vogt [79] (blue shaded band) and the latest calculation from TAMU model [82] considering the nuclear absorption effects on top of nPDF effects (black shaded band). The statistical and systematic uncertainties are shown as vertical bars and shaded boxes respectively around the data points. The red band on the right side around unity represents the common normalization uncertainties.</p>	161

LIST OF FIGURES (Continued)

<u>FIGURE</u>		<u>PAGE</u>
84	<p>The new R_{pAu} (red stars) of $\Upsilon(1S+2S+3S)$ as a function of rapidity are compared to different theoretical model calculations. The blue hatched band shows predictions based on EPS09 nPDF done by R. Vogt [79]. Prediction only considering the initial-state energy loss effect is shown as a gray dashed line, while the prediction considering both initial-state energy loss and the EPS09 nPDF are shown as the red dot-dashed line [84]. The latest calculations from TAMU model [82] considering the nuclear absorption on top of nPDF effects is shown as black shaded band. The statistical and systematic uncertainties are shown as vertical bars and shaded boxes respectively around the data points. The colored band on the right side shows the common normalization uncertainties.</p>	163
85	<p>R_{AA}^{1S} (black stars) and R_{AA}^{2S+3S} (black stars) as a function of N_{part}, combined from di-electron and di-muon channels. The vertical bars shows the statistical uncertainty. The open boxes around data points shows the systematic uncertainty. The light gray bands represent the uncertainty from N_{coll}. The red band around unity on the right side shows the common normalization uncertainty from the Υ measurements in p+p collisions.</p>	164
86	<p>The left panel shows the comparison of R_{AA}^{1S} in Au+Au collisions at $\sqrt{s_{NN}} = 200$ GeV from STAR (red stars) and in Pb+Pb collision at $\sqrt{s_{NN}} = 2.76$ TeV from CMS [44] (black rhombus). The right panel shows the comparison of Υ excited states R_{AA} between STAR ($\Upsilon(2S+3S)$ shown in red stars) and CMS ($\Upsilon(2S)$ shown in black rhombus, $\Upsilon(3S)$ shown in down arrow denoting an upper limit with 95% C.L.). The vertical bars shows the statistical uncertainty. The open boxes around data points shows the systematic uncertainty. The light gray bands around STAR data points represent the uncertainty from N_{coll}. The colored bands around unity on the right side represent the common normalization uncertainty.</p>	166
87	<p>The R_{AA}^{1S} (left panel) and R_{AA}^{2S+3S} (right panel) from STAR measurements are compared to the Rothkopf Model [87] developed by Krouppa, Rothkopf and Strickland (green band), and to the Rapp Model [88] developed by Du, He and Rapp (blue band).</p>	168
88	<p>The screen-shot of the online copyright statement of Nuclear Physics A.</p>	171
89	<p>The screen-shot of the online copyright statement of EPJ Web of Conferences.</p>	172
90	<p>The screen-shot of the online copyright statement of EPJ Web of Conferences.</p>	173

CHAPTER 1

INTRODUCTION

1.1 Elementary Particles and Fundamental Interactions in the Standard Model

All known elementary particles and the known fundamental forces (the electromagnetic, weak, and strong interactions) except the gravitational force, can be described by one quantum theory, the Standard Model. A summary of the elementary particles and fundamental forces in the Standard Model is shown in Figure 1. In the Standard Model, all elementary particles can be classified as Fermions and Bosons according to their spin, where spin is an intrinsic form of angular momentum of elementary particles. Particles with spins in half-integer multiples (e.g, $1/2$, $3/2$, $5/2$, etc.) are Fermions; particles with spins in integer multiples (e.g, 0, 1, 2, etc.) are Bosons.

Fermions obey the Pauli exclusion principle, and each Fermion has its own antiparticle. Fermions include 6 quarks (up-**u**, down-**d**, charm-**c**, strange-**s**, top-**t**, bottom-**b**), and 6 leptons (electron-**e**, electron neutrino- ν_e , muon- μ , muon neutrino- ν_μ , tau- τ , tau neutrino- ν_τ). Quarks are grouped into 3 generations: up and down as the first generation, charm and strange as the second generation, top and bottom as the third generation. A member of a higher generation is heavier than that from the lower generations. The first generation (up and down quarks) never decay so that most of matter in the world are made of them; atoms are composed of electrons and nuclei where nuclei is constituted of up and down quarks. The second and third

generations could decay within an extremely short life time, thus they only exist in very high-energy environments but not in the normal conditions.

Besides the spin, quarks also carry color charges, which allows them join the interactions via the strong force. The strong interactions between quarks could bind them tightly together as a bound state, such as mesons or baryons. Two commonly mentioned examples of baryons are proton and neutrons. The electric charge and weak isospin of quarks allow them interact with other fermions by the Electromagnetic and Weak forces. Unlike quarks, leptons do not carry a color charge, thus they cannot participate in the strong interaction. Among these leptons, electron, muon and tau carry an electric charge, which allows them to join the electromagnetic interactions. However the 3 neutrinos do not carry electric charge, so they can only participate the weak interaction, that is also the main reason that they are very difficult to be detected experimentally.

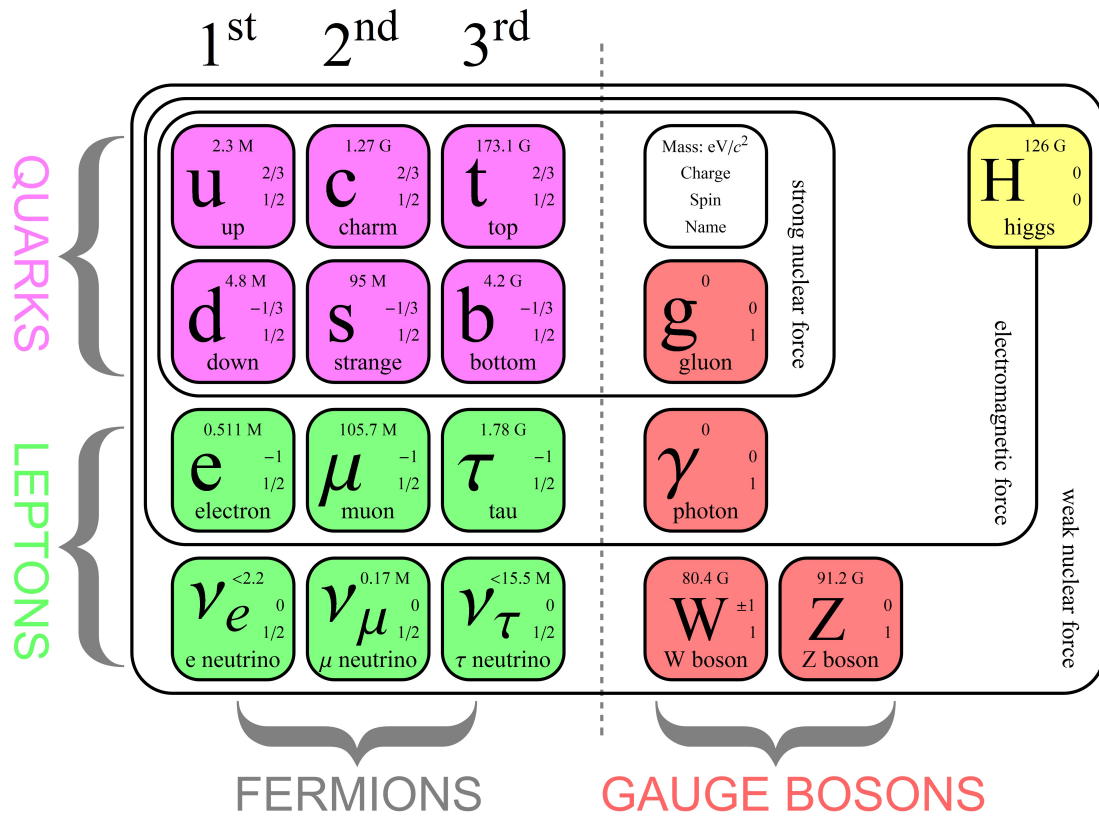


Figure 1: A summary of elementary particles as well as the fundamental forces in the Standard Model. For each particle, its mass, charge and spin values are listed in colored box. The three generations of quarks are shown in blue: (u, d), (c, s), (t, b). The three leptons and their associated neutrinos are in green: (e, ν_e), (μ , ν_μ), (τ , ν_τ). All quarks and leptons are Fermions while gluons, photons, W^\pm and Z are Bosons, which act as force carriers, are shown in red. The recently discovered Higgs boson, the so called “god particle” is shown in yellow at the top right. Three black open squares enclose those particles which could participate the corresponding fundamental forces. This figure is cited from sciencesptrings [2]

Bosons obey the Bose-Einstein statistics. Bosons can be classified as Gauge bosons and Scalar bosons according to their spin values. Gauge bosons has a none-zero spin, and can act as the force carriers while Scalar bosons with a zero spin, cannot be the force carrier. Gauge bosons mediate the electromagnetic, weak and strong interactions in the Standard Model. At the macro level, the electromagnetic force allows particles to interact with others via electric and magnetic fields, while gravity allows particles with mass to attract others following Einstein's theory of general relativity. In the Standard Model, the fundamental forces can be explained as originating from the exchanging of bosons between matter particles, generally the bosons are called the force mediating particles. When particles exchanged a force-mediating particle (a boson), it is equivalent to a force influencing both of them at a macroscopic level, and the boson is therefore can be taken as to have mediated that force.

There are 3 types of gauge bosons which are the force carriers of 3 fundamental interactions:

- Photons: the force carrier for the electromagnetic (EM) interaction. Photons are massless particles.
- W^\pm and Z : the force carrier for the weak interaction. Mass of W^\pm is 80.4 GeV and mass of Z is 91.2 GeV. As W^\pm carries electric charge, they participate the EM interaction, while the neutral Z gauge boson does not.
- Gluons: the force carrier for the strong interaction. Gluons are massless. Different to photons in Quantum Electrodynamics, gluons carry color charge by themselves, thus also interact among themselves by the strong force.

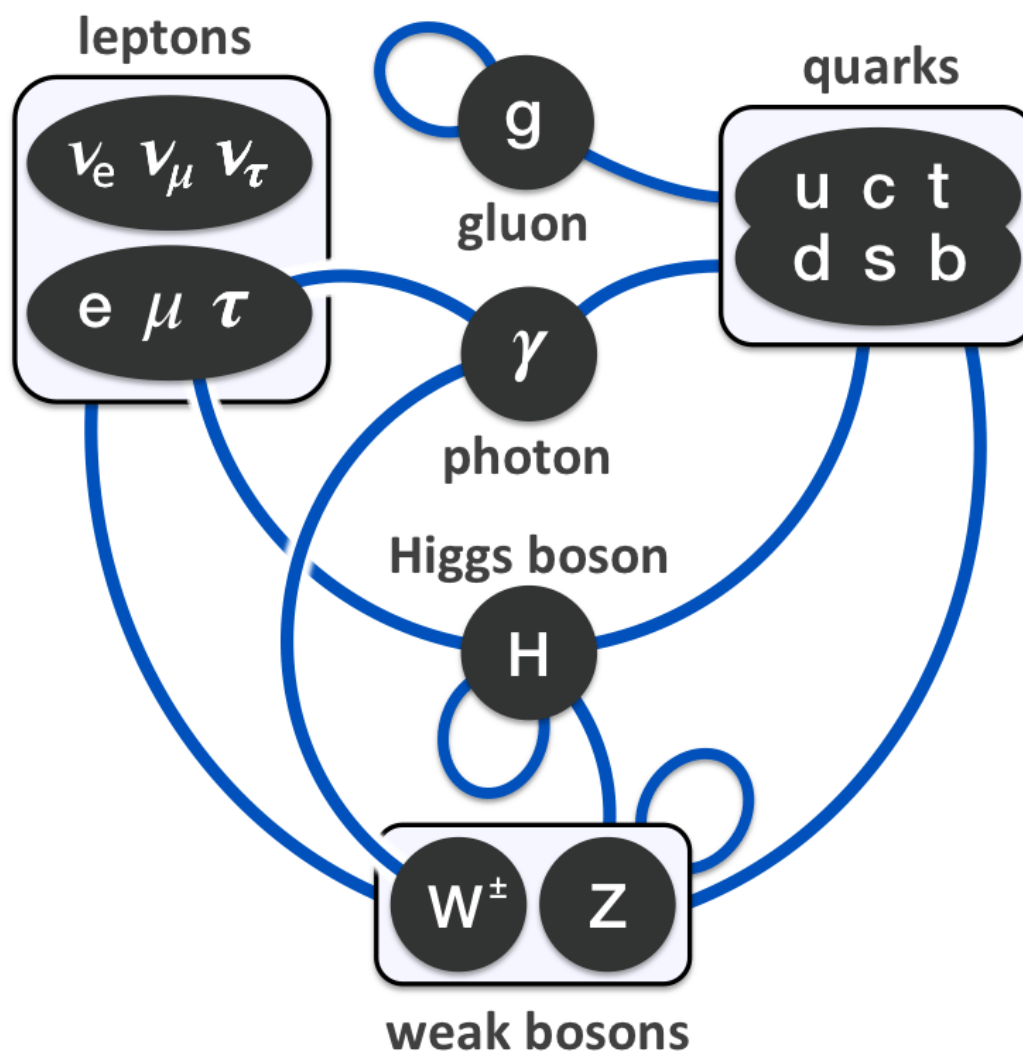


Figure 2: A diagram summarizing the tree-level interactions between elementary particles in the Standard Model. Photon, W^\pm and Z bosons are the force mediating particles. Higgs boson generate the mass of elementary particles. This figure is cited from wikipedia [3]

Higgs boson is a massive scalar elementary particle, which has been discovered recently by experiments at the Large Hadron Collider (LHC). Unlike other bosons, Higgs boson has no intrinsic spin, or has zero spin, thus it cannot be a force carrier like other bosons. However, Higgs boson plays a very important role in the Standard Model. The “Higgs mechanism” where the Higgs field and its corresponding Higgs boson could give mass (note that, the mass here is not the gravitational mass but the inertial mass) to all elementary particles including all the quarks and leptons. It could explain why photon is massless while W and Z bosons are heavy, thus explain the difference between the electromagnetic force and the weak force in a fundamental level.

1.2 Quantum Chromodynamics (QCD) and the Quark-Gluon Plasma (QGP)

Today, evidences suggest that the universe began from the “Big-Bang”. A millionth of a second after the Big Bang, the universe was filled with extremely hot and dense matter, including quarks-fundamental constituents of the visible matter, and gluons-carriers of the fundamental strong force. Under normal conditions, quarks and gluons are confined inside protons, neutrons or other hadrons. However, at the extremely high temperature and high energy density, such as the very early universe, all the known elementary particles are extremely relativistic that even those “strongly interacting” particles (quarks and gluons) would only interact relatively weaker due to the famous phenomenon of asymptotic freedom. Such a system of hot, dense and weakly interacting elementary particles make a new state of matter, Quark-Gluon Plasma (QGP). An illustration of the expansion of the universe is shown in Figure 3.

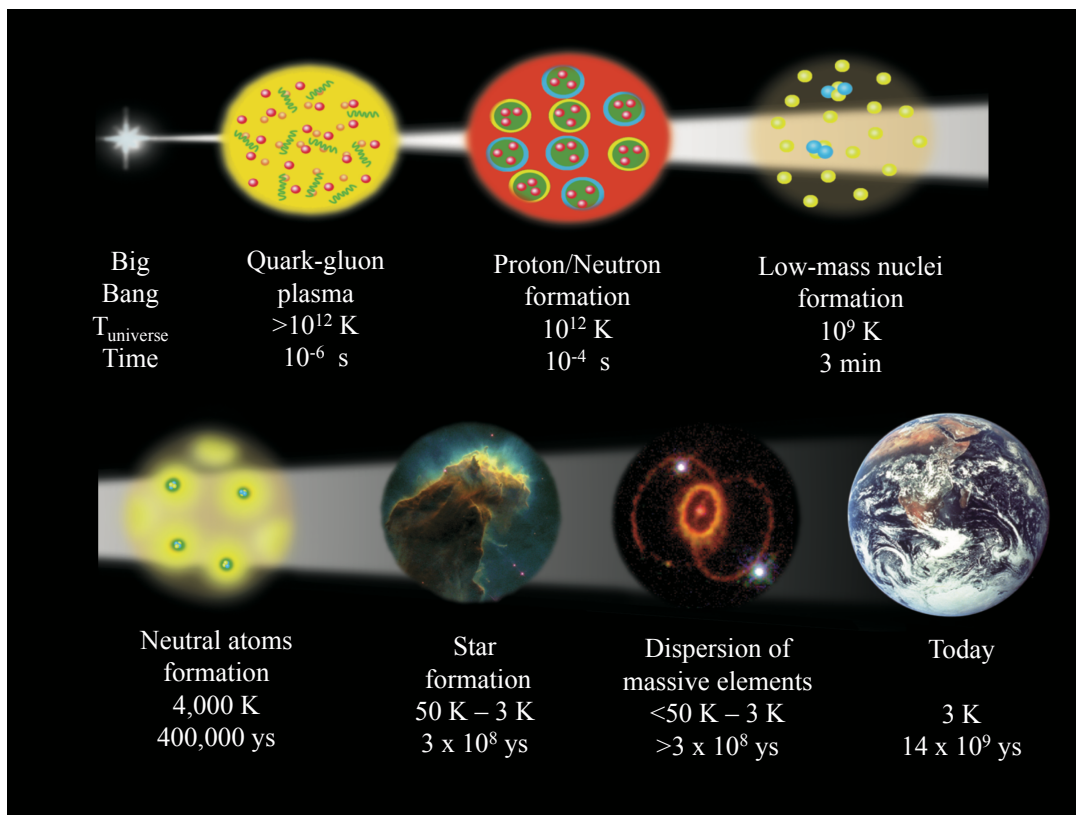


Figure 3: An illustration of the expansion of the universe. According to the Big Bang theory, the universe expanded and cooled down shortly after the Big Bang. After $\sim 10^{-6}$ seconds, the universe experienced a state of Quark-Gluon Plasma (QGP) where all quarks and gluons are de-confined. When the temperature of Universe (T_{universe}) cooled down to $\sim 10^{12}$ K, quarks coalesced into protons and neutrons. As time progressed, the light nucleus such as deuterium, helium and lithium were formed by protons and neutrons. Then, electrons, protons and neutrons formed low-mass neutral atoms. As clouds of atoms attracted each other through gravity and formed initial stars, where more massive elements can be fused by hydrogen and helium. The most massive elements of the universe were formed from the explosion of stars. After the explosion, massive debris dispersed into space, among which, our earth was formed. The figure is cited from [4]

1.2.1 Asymptotic Freedom and Confinement in QCD

Asymptotic freedom is one of the striking properties of QCD, it states that “the interaction strength (α_s) between quarks becomes smaller as the distance between them gets shorter” [5]. The running coupling constant in QCD calculated by the first order perturbative QCD calculations is given as:

$$\alpha_s(Q) = \frac{g_s^2(Q)}{4\pi} \approx \frac{2\pi}{\beta_0 \ln(Q/\Lambda_{\text{QCD}})} \quad (1.1)$$

where, the constant $\beta_0 = (11 - \frac{2}{3}n_f)$ with $n_f = 6$ is the number of active quark flavors. Λ_{QCD} is a parameter of QCD scale determined by experiment ($\Lambda_{\text{QCD}} \sim 250$ MeV). Q is the four-momentum transfer, usually taken as the energy scale. For higher values of Q (probing at smaller distances), α_s is smaller. In the limit of very large Q , $\alpha_s \rightarrow 0$ which means the coupling vanishes, thus quarks and gluons can move freely. This property of QCD is called the asymptotic freedom. This interesting behavior of the strong coupling has been predicted by different theoretical calculations and been verified by experimental measurements as shown in Figure 4. Due to the asymptotic freedom, perturbative QCD (pQCD) is applicable when the momentum transfer is large. Today, pQCD has made great achievements on the predictions and explanations of experimental measurements in high energy physics.

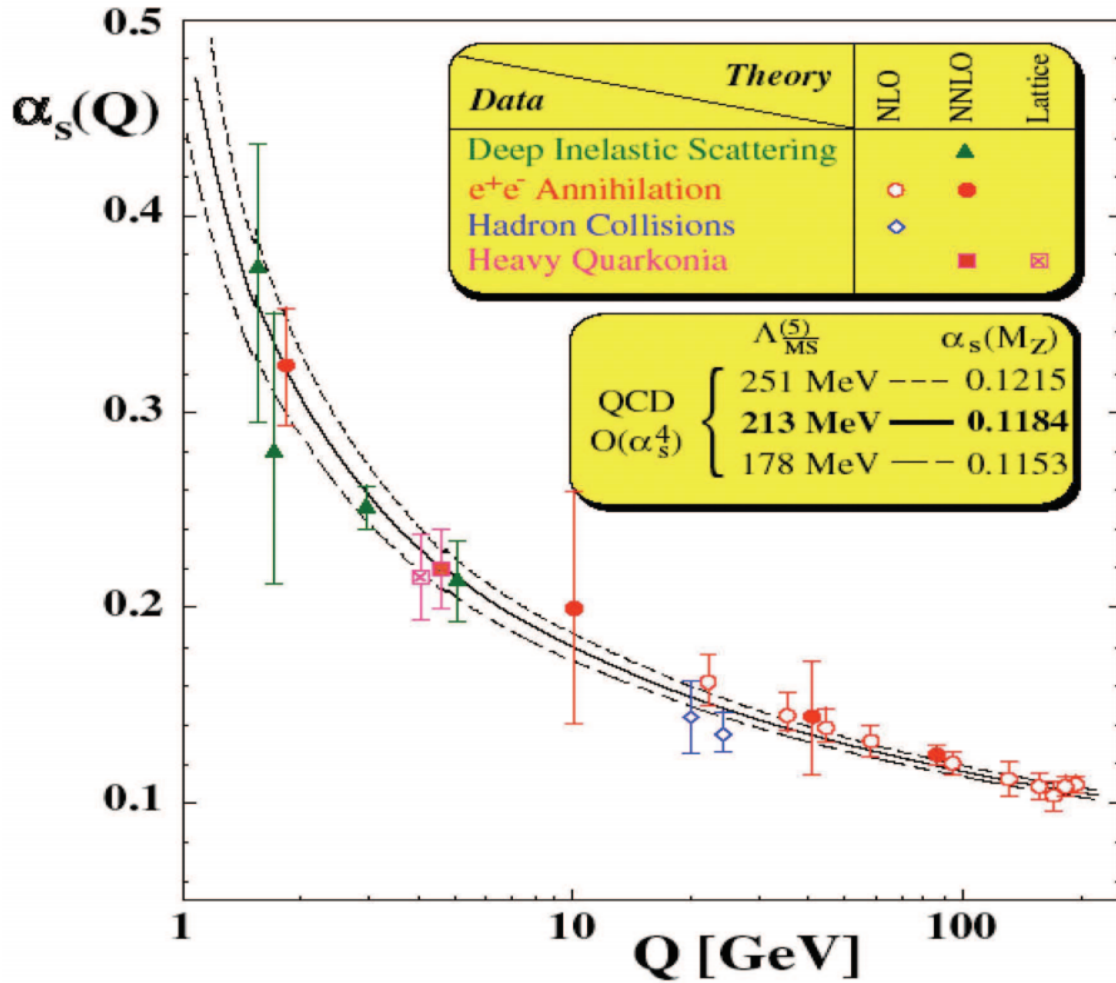


Figure 4: The running coupling constant in QCD as a function of the energy scale from both experimental and theoretical studies. This figure is cited from [6]

Another prominent property of QCD is the color-confinement, which states: no any colored particle can be isolated, instead, they will form a color neutral hadron under the normal condi-

tion. When two quarks ($q_1\bar{q}_2$) are separated to an observable distance, the energy of the system will be above the quark-antiquark pair production energy threshold, thus instead of successfully separating these two quarks, a new quark-antiquark pair ($q_0\bar{q}_0$) will be generated, and then two new mesons ($q_1\bar{q}_0, q_0\bar{q}_2$) will be formed. That is also the reason that no isolated free quark was observed in experiment. Today, the color confinement is still a theoretical conjecture that is consistent with experimental observations, however, its strict proof is still a challenge task.

1.2.2 Features of QGP in Perturbative QCD

An important feature of the QGP is the color deconfinement. By the perturbation QCD, partons, quarks and, gluons are treated as free particles thus can be described by the plane waves. The high momentum transfer interactions between these partons are expected to be weak by the asymptotic freedom. The small-momentum transfer scattering involving long distance interactions will be screened by the QGP. So that, all the quarks and gluons can move inside the QGP without being confined. When a colored particle is put inside QGP, the surrounding particles will screen it so that the interactions between colored particles is damped exponentially. The corresponding screening length can be calculated by starting from a colored particle and color field induced by itself. The result of this calculation is given as a correlation function of gluon fields. Based on the perturbation theory calculation at extremely high-temperature, a screening mass can be obtained as $m_D^2 = g^2T^2$, where the screening length, the so-called “Debye Screening Length” is defined as $1/gT$ or $1/m_D$. When the temperature goes higher, the Debye screening length becomes shorter. When the colored particles are screened, they will have a finite energy so that they can be taken as free moving particles. Note that, there

is another interaction that still needs to be considered, the magnetic interaction since it is only weakly screened as it has a screening mass $\sim g^2 T$. So the magnetic interactions inside the QGP is still non-perturbative. Fortunately, the contribution from magnetic sector on the physical observables only becomes important for the higher-order of QCD coupling at the high temperature, thus the property of QGP remains dominantly as free motion.

1.2.3 Phase Transition in Lattice QCD Calculation

The rapid rise in computational power and implementation of better algorithms lead to a significant progress of lattice calculations of QCD thermodynamics in the last decade. The theoretical predictions from the lattice QCD calculations are shown in Figure 5. A clear transition of ϵ/T^4 is found at a fairly well-defined temperature “Critical Temperature” $T_C \sim 150 - 180$ MeV. Where, T is the temperature, ϵ is the energy density, ϵ/T^4 is a thermodynamic observable which is proportional to the number of degrees of freedom in a statistical system. When temperature is lower, ϵ/T^4 increases with T/T_C by a mediate slope, however when temperature gets closer to the critical temperature T_C , this slope undergoes a rapid enhancement. Such an rapid change indicates the fundamental degrees of freedom are different when lower and higher than T_C .

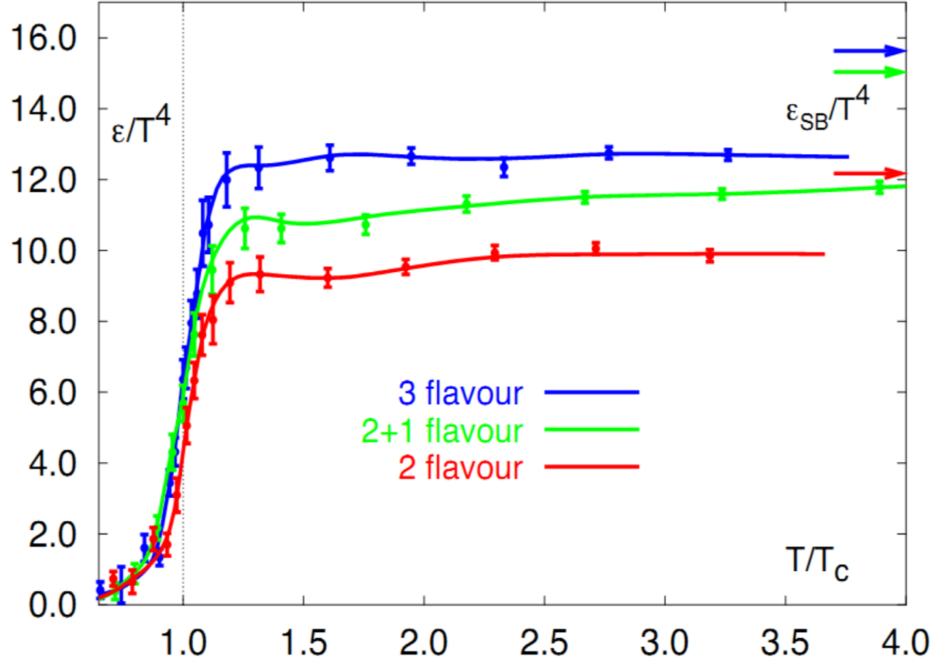


Figure 5: A thermodynamic quantity ϵ/T^4 as a function of temperature T/T_c predicted by the lattice QCD calculations (simulations) [7] These calculations are carried out with three different flavor combinations: 3 light flavors, 2 light flavors + 1 heavy flavor, 2 light flavors.

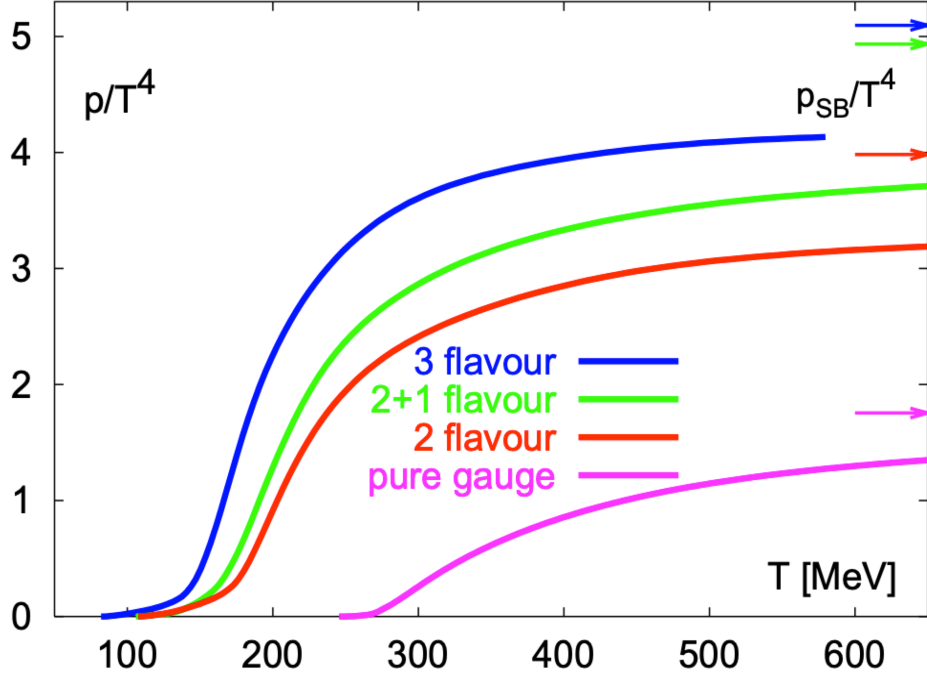


Figure 6: The pressure of the system as a function of temperature predicted by the lattice QCD calculations (simulations) [7]. These calculations are done with four different cases: 3 light flavors, 2 light flavors + 1 heavy flavor, 2 light flavors, pure gauge.

The pressure of the system as a function of temperature predicted by the lattice QCD calculation is shown in Figure 6. When the temperature is low, the pressure increases slowly with the temperature. When temperature gets closer to the T_C , the pressure will increase with temperature drastically. This change in the behavior of pressure, similar to the energy density, corresponds to the changes in the number of degrees of freedom, indicates a QCD

phase transition is happening. As temperature increases from T_C to $2T_C$, the pressure goes up gradually. Note that when the temperature stay only up to a few times T_C , the system can not be simply treated as weakly interacting partons while calculating the dynamical properties. When temperature keeps going higher $2T_C$, the pressure curve becomes flat which is consistent with the ideal gas limit.

When chiral symmetry is included into the lattice QCD calculations, an interesting property of the phase transition is observed. The chiral symmetry of the QCD Lagrangian is spontaneously broken due to the emerge of flavor dependent quark mass. If quarks are massless particles, the QCD Lagrangian is invariant under the flavor rotations between left and right handed quarks, thus allows the chiral symmetry. In the QGP phase where $T > T_C$, the chiral symmetry is found to be restored according to the lattice QCD calculations. Figure 7 shows the order parameter for chiral symmetry restoration $\langle \bar{\psi}\psi \rangle$ in chiral limit and the order parameter for deconfinement $\langle L \rangle$ in the pure gauge limit. The $\langle L \rangle$ is the expectation value of Polyakov Loop, which characterizes the property of the heavy quark free energy at large distances. The $\langle \bar{\psi}\psi \rangle$ is scalar quark density, which characterizes the effective mass of a quark in the medium. In the same figures, their corresponding susceptibilities ($\chi_L = N_c^3(\langle L^2 \rangle - \langle L \rangle^2)$, $\chi_m = \partial \langle \bar{\psi}\psi \rangle / \partial m_q$) are also shown. This clearly shows that order parameters of $\langle \bar{\psi}\psi \rangle$ and $\langle L \rangle$ coincide with each other at the similar rapid changing point where the corresponding susceptibilities attain their peaks. This observation means the chiral symmetry restoration and the deconfinement are strongly correlated.

The behavior of Polyakov loop susceptibility is a clear observable for the first order QCD phase transition under the large quark mass limit, in other words, this observable can characterize the transition between confinement-deconfinement in the pure gauge limit. The behavior of the chiral condensate and the susceptibility is a most remarkable character for the transition in the chiral limit.

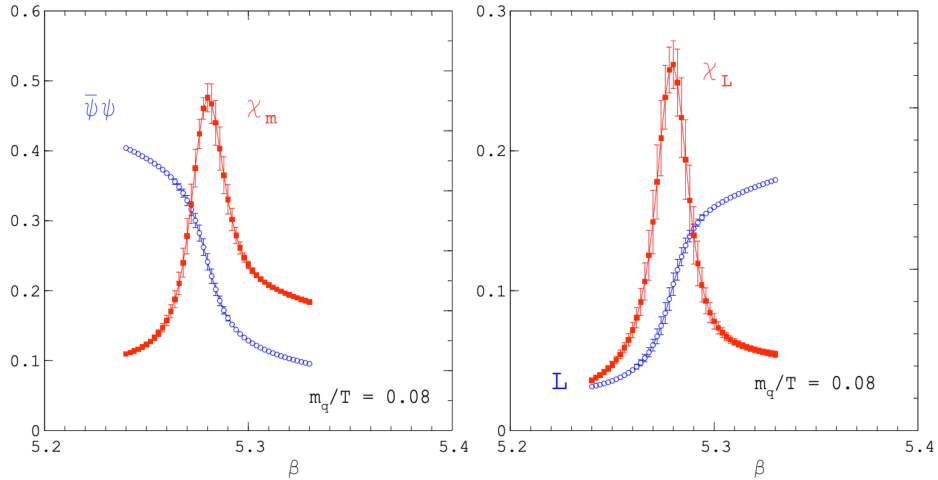


Figure 7: The chiral symmetry restoration and deconfinement calculated by lattice QCD [7]. The left panel shows order parameter $\langle \bar{\psi}\psi \rangle$ (blue curve) for chiral symmetry breaking with while $m_q \rightarrow 0$ (chiral limit). The right panel shows the order parameter of $\langle L \rangle$ (blue curve) for deconfinement while $m_q \rightarrow \infty$ (pure gauge limit). Also shown in the two figures are their corresponding susceptibilities as a function of coupling coefficient $\beta = 6/g^2$.

1.3 Study QGP via High Energy Heavy Ion Collisions

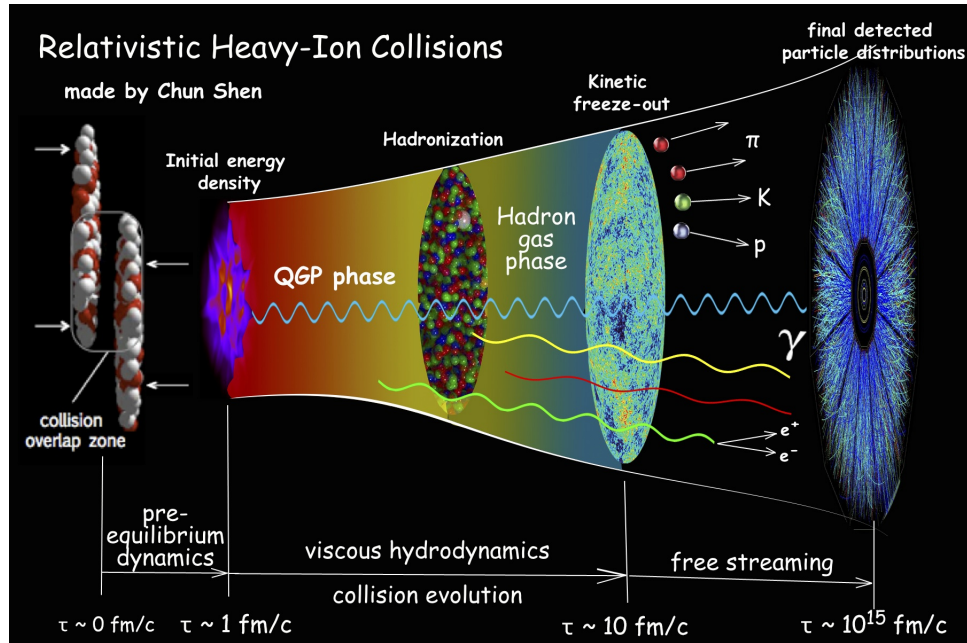


Figure 8: An illustration of system evolution in relativistic heavy-ion collisions [8].

To better understand the evolution of the early universe as well as the strong force, collisions between massive ions are made in laboratory in order to reproduce the similar conditions as the early universe. Hundreds of protons and neutrons of two nuclei are accelerated to at nearly the speed of light and then smash into one another, and form a miniscule “fireball” in which

protons and neutrons “melts” into a QGP. After the QGP cools almost instantly after its creation, quarks and gluons recombine into hadrons.

To study the conditions similar to the early universe, high energy collisions between massive ions, such as lead or gold nuclei are performed in the very powerful accelerators. In these heavy-ion collisions, a miniscule fireball is formed, in which all matters “melts” into the so-called quark-gluon plasma. This plasma is extremely hot, about 250,000 times hotter than the center of the sun. When the fireball cools down, the individual quarks and gluons, collectively called partons, recombine into hadrons. After a bunch of decay processes, many particles fly into the detector system in all directions. By analyzing the signals of these particles, the properties of QGP can be studied.

An important feature of the particle production and the medium evolution in heavy-ion collisions is their dependence on the initial geometry of the collision system. The initial geometric overlap of two colliding heavy ions for a given collision energy determines the initial energy density and geometry of the medium created in a collision, thus determines the evolution of the medium and their interactions with the particles produced in the collisions. The initial collision geometry typically is characterized by three geometrical variables (or centrality variables): the impact parameter (b), the number of participating nucleons (N_{part}) and the number of binary nucleon-nucleon collisions (N_{coll}). However these geometrical variables can not be measured directly by experiments, instead, they are obtained by mapping to other measurable physics quantities, typically the particle multiplicity, which grows up monotonically with the more central collisions. This mapping can be realized under the centrality determination frame work

of Glauber Model simulations [9–18]. Figure 9 illustrates the relationship between the measured charged particle multiplicity N_{ch} , the average impact parameter b , the average number of participating nucleons N_{part} and the centrality in percentage, in the Au+Au collisions at $\sqrt{s_{\text{NN}}} = 200$ GeV. The reason to use the average value of b and N_{part} is that they are obtained by averaging within a particular centrality bin (e.g. 0-5%, 5-10%). The lowest value of N_{part} is corresponding to the most peripheral collision events while events with increasing N_{part} are corresponding to the semi-peripheral, semi-central and central collisions events, respectively.

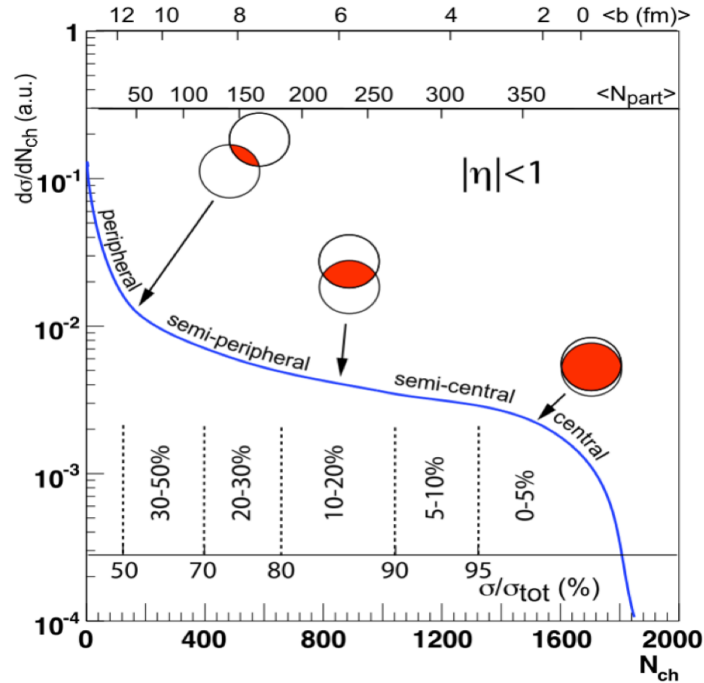


Figure 9: An illustration of the relationship between the measured charged particle multiplicity N_{ch} , the impact parameter b , the average number of participating nucleons N_{part} and the centrality in percentage. This figure is cited from [19]

1.4 Quarkonium Suppression as a Probe of QGP

Quarkonia are mesons composed of heavy quark (c quark or b quark) and anti-quark, including charmonia ($c\bar{c}$, such as J/ψ , ψ , ...) and bottomonia ($b\bar{b}$, such as $\Upsilon(1S)$, $\Upsilon(2S)$, ...). The summary of the charmonium family and bottomonium family and their decay patterns are shown in Figure 10 and Figure 11, respectively. At low temperatures or low energy densities, the heavy quark and anti-quark are bounded tightly together as a quarkonium state, however when the system temperature or energy density becomes higher than the critical temperature T_C , the binding energy between the heavy quark and anti-quark will be color screened by the surrounding partons, thus results in the suppression of quarkonium production.

Measurements of quarkonium production are an important tool to study the properties of the Quark-Gluon Plasma (QGP) formed in relativistic heavy-ion collisions. Quarkonium suppression due to the color-screening effect was proposed as a direct evidence of the QGP formation [1]. Different quarkonium states with different binding energies, thus are predicted to melt at different medium temperatures. Therefore, the measurement of such a “sequential melting” can help constrain the temperature of the created medium in the heavy ion collisions.

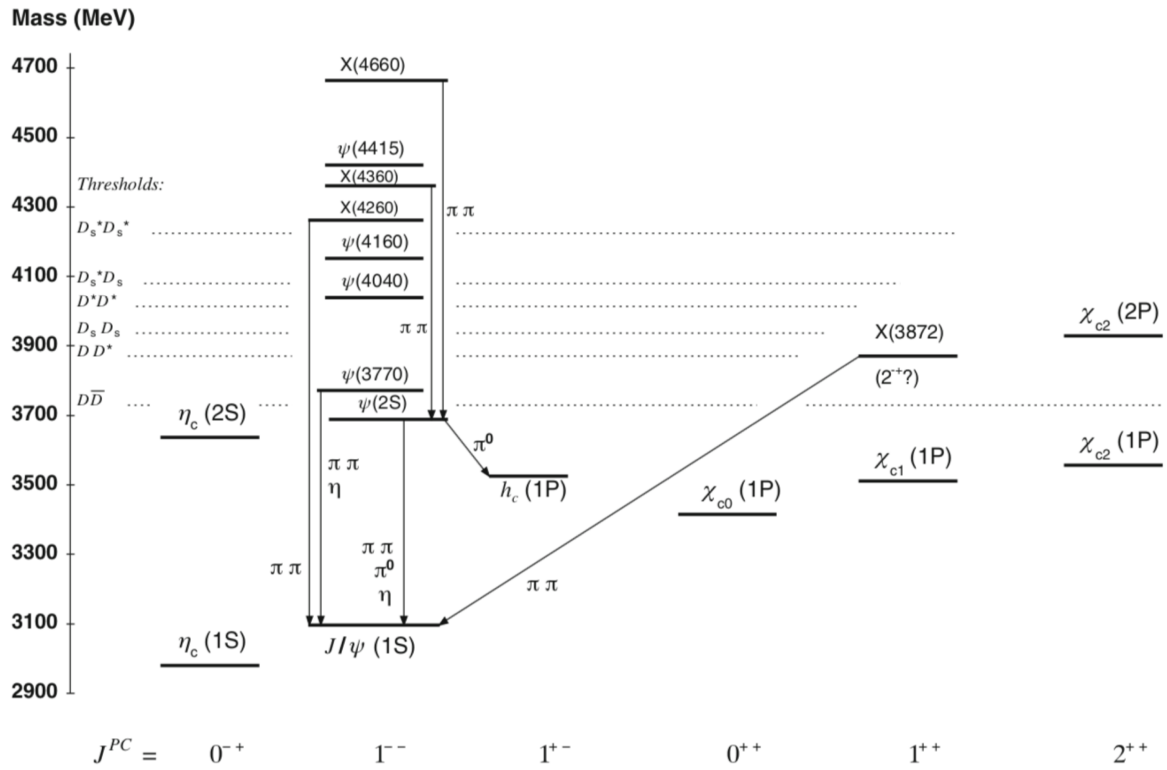


Figure 10: The charmonium family feed-down pattern [20]. (Those “X” states are experimental observed particles but their nature is still unknown.)

of heavy quark-antiquark pairs and the formation of quarkonium states from these heavy quarks. The calculation of heavy quark pair production can be well described by the perturbative QCD since it involves large momentum transfers (heavy quark mass $> \Lambda_{\text{QCD}}$) during the initial hard scattering between partons. The probability densities to find a parton carrying a fraction x of the longitudinal momentum of a nucleon, at a squared energy scale Q^2 , can be described by the parton distribution functions, “PDFs”. Today, the PDFs can be precisely measured in the scattering processes like Deep Inelastic Scattering (DIS) of leptons off nucleons. The calculation of the formation of quarkonium states from these heavy quarks and antiquarks, as this process is mainly soft (typical momentum scales $Q = mv$, where $v_c \sim 0.3$, $v_b \sim 0.1$), is expected to be non-perturbative. Today, different models were developed to describe the mechanism of quarkonium productions, among which the basic ideas are similar, by combining the factorization of heavy quark pair production and the hadronization. The main differences between these models are their assumptions of the hadronization process. In the following part of this section, several models will be introduced.

Color-Evaporation Model (CEM) : The main assumption of CEM [21–23] is that if the invariant mass of produced $Q\bar{Q}$ pair is above the kinematic threshold ($m_{Q\bar{Q}} > 2m_Q$), at the meantime below the corresponding lightest open heavy flavor mesons mass ($m_{Q\bar{Q}} < 2m_H$, where H denotes D meson for charmonium or B meson for bottomonium), the probability of this $Q\bar{Q}$ pair forming a quarkonium state does not depend on their spin or color configuration.

The inclusive cross section of quarkonium production predicted by the leading order CEM calculations in $p + p$ collisions is given by:

$$\sigma_{\text{QM}}^{\text{CEM}}(p + p \rightarrow \text{QM} + X) = F_{\text{QM}} \sum_{i,j} \int_{4m_{\text{Q}}^2}^{4m_{\text{H}}^2} d\hat{s} \int dx_1 dx_2 f_i(x_1, \mu) f_j(x_2, \mu) \hat{\sigma}_{ij}^{\text{Q}\bar{\text{Q}}}(\hat{s}) \delta(\hat{s} - x_1 x_2 s) \quad (1.2)$$

Where, F_{QM} is a universal phenomenological constant parameter that needs to be determined by experimental measurements. F_{QM} denotes for the probability of each quarkonium state “QM” been formed from these produced heavy quark pairs. f is the parton distribution function, x is the momentum fraction of a parton inside a nucleon, μ is the factorization scale. $\hat{\sigma}_{ij}^{\text{Q}\bar{\text{Q}}}$ denotes the partonic cross section for heavy quark pair production while running over all parton species ($q\bar{q}$ or gg). \hat{s} is the square of the parton-parton center-of-mass energy.

CEM may be the simplest model of quarkonium production which successfully describes the main features of quarkonium productions measured by the world-wide high energy experiments. However, the assumption of the subsequent probability of quarkonium production as a constant parameter is too simple, which is not consistent with experimental observations. Another weakness of CEM is that it has no power to give any prediction on the polarization of quarkonium.

Color-Singlet Model (CSM): The main idea of CSM [24–26] is that the quantum state of the heavy quark-antiquark ($Q\bar{Q}$) pair never change between its production and hadronization. The $Q\bar{Q}$ pair has to be produced in a color singlet state, and the final quarkonium state should have the same spin and angular momentum quantum numbers as the initial $Q\bar{Q}$ pair. CSM also

assumes that the quarkonium states can be treated as non-relativistic bound states, as follows, the parton-parton cross section for quarkonium production should then be constructed with negligible relative velocity between the heavy quark and its antiquark, and the probability for the transition from $Q\bar{Q}$ pair to a quarkonium state is determined by the wave function of the $Q\bar{Q}$ pair at the spatial origin. The inclusive parton-parton cross section for the quarkonium production is given as:

$$\sigma_{\text{QM}}^{\text{CSM}}(\mathbf{p} + \mathbf{p} \rightarrow \text{QM}[{}^{2S+1}\text{L}_J] + \text{X}) = \left| \frac{d^L \Psi_{\text{nl}}(0)}{d\mathbf{r}^L} \right|^2 \hat{\sigma}_{ij}(ij \rightarrow Q\bar{Q}[{}^{2S+1}\text{L}_J]) \quad (1.3)$$

Where, Ψ_{nl} is the wave function of $Q\bar{Q}$, $\hat{\sigma}_{ij}$ is parton-parton cross section for the partons i and j to evolve into a color singlet $Q\bar{Q}$ pair possessing same quantum numbers of ${}^{2S+1}\text{L}_J$ as the final quarkonium state “QM”. In CSM, the input parameters of wave function Ψ_{nl} can be extracted from the decay width measurements of quarkonium states, thus CSM in principle becomes a very predictive model. However, it was found that CSM significantly underestimated the cross section of prompt charmonium production in p+p collisions at $\sqrt{s} = 1.8$ TeV [27]. Another issue with CSM is that it can not predict the production and decay of P-wave quarkonium states, because of such calculation will inevitable introduce the color-octet contributions.

Color-Octet Model (COM): COM [28–30] is developed based on the effective theory non-relativistic QCD (NRQCD), and assuming the probability of a $Q\bar{Q}$ pair hadronized into a quarkonium state can be expressed in a rigorous way via the long-distance matrix elements

(LDMEs). Considering the fact that heavy quarks are so massive that their velocity are much smaller than the speed of light. Therefore, NRQCD employs the expansion in powers of velocity v besides the normal expansion in powers of α_s . It accounts for the effect of higher-Fock states (w.r.t. v) where $Q\bar{Q}$ pair is in an octet state with different quantum states of L and S, which thus provides a way to describe the non-perturbative transition between the colored states (octet state) to a meson (color neutral). The cross section of quarkonium production in COM is given as:

$$d\sigma_{QM}^{\text{COM}}(p + p \rightarrow QM + X) = \sum_{i,j,n} \int dx_i dx_j f_i(x_i, \mu_F) f_j(x_j, \mu_F) d\hat{\sigma}_{i+j \rightarrow (Q\bar{Q})^n + X}(\mu_R, \mu_F, \mu_\Lambda) \langle O_Q^n \rangle \quad (1.4)$$

Where, n denotes sets of quantum numbers including color, angular momentum and spin. f is the parton distribution function, x is the momentum fraction of a parton inside a nucleon, μ_R is the renormalization scale, μ_F is the factorization scale and μ_Λ is a NRQCD scale. $\langle O_Q^n \rangle$ is the long-distance matrix elements (LDMEs) which tells the probability to find the point-like $Q\bar{Q}$ pair in the wave function of quarkonium state. The elements of $\langle O_Q^n \rangle$ need to be determined via fitting the the next-to-leading order calculations under the NRQCD framework to experimental data. COM includes the contribution of $^3S_1^{[8]}$ (octet) states in P-wave (angular momentum $L=1$) productions, which cancels the divergences in CSM. However too many parameters of this model make it has a weaker predictive power.

1.4.2 Physics of Quarkonium Suppression

Quarkonium suppression is considered as one of the signatures of the QGP formation in heavy-ion collisions. The heavy quark and its own antiquark are bound tightly together inside a quarkonium state under normal conditions. The binding potential between heavy quark and antiquark is expected to be screened, in the hot medium of QGP, by the surrounding deconfined partons (light quarks, gluons). Therefore, the quarkonium production in nucleon-nucleon collisions are expected to be suppressed with respect to that in proton-proton collisions. Moreover, different quarkonia states with different binding energies thus “melt” at different temperatures, so that a sequential suppression pattern of quarkonium states is expected. As a consequence, measurements of such a sequential suppression pattern provide a opportunity to estimate the temperature of QGP created in the heavy ion collisions. However, besides the color screening effect, several other effects also need to be considered for a full interpretation of the measured quarkonium suppression. These other effects include contributions of feed-down decays from higher mass quarkonium states or from the b-hadron (in case of charmonium), contributions of recombination (regeneration) of dissociated heavy quarks, and the cold nuclear matter effects.

Color screening effect: The main idea of color screening effect is that the range of the strong interaction which bind the $Q\bar{Q}$ pair can be reduced by the surrounding colored partons inside the hot medium (QGP) [31]. This range is called the color screening radius or Debye screening radius, r_D , which is inversely proportional to the medium temperature and the color charge density. The hotter and denser medium means a smaller r_D . A phonologically description

is that the fate of a quarkonium state in the hot medium depends on the relationship of size between its radius and the r_D . If the quarkonium radius is larger than r_D , these two heavy quarks are “blind” to each other, “color screened”, hence it will melt. However, if quarkonium radius is smaller than r_D , the interactions between this $Q\bar{Q}$ pair will not be screened by the medium, thus will survive as a meson. In the QGP, the survival probability of quarkonium state relies on its binding energy and radius. The information including mass, binding energy and radius of each quarkonium state are listed in Table I. As different quarkonium state has different radius and different binding energy, a sequential suppression of them is naturally expected, as illustrated in Figure 12. The dissociation temperatures “ T_{diso} ” of quarkonium states have been evaluated via different theoretical approaches and models including the lattice QCD, QCD sum rules, AdS/QCD, potential models and effective field theory based models, a summary of predicted “ T_{diso} ” from these calculations are shown in Figure 13.

State	J/ ψ	$\chi_c(1P)$	$\psi(2S)$	$\Upsilon(1S)$	$\chi_b(1P)$	$\Upsilon(2S)$	$\chi_b(2P)$	$\Upsilon(3S)$
m (GeV/ c^2)	3.07	3.53	3.68	9.46	9.99	10.02	10.26	10.36
E_{bd} (GeV)	0.64	0.20	0.05	1.10	0.67	0.54	0.31	0.20
r (fm)	0.25	0.36	0.45	0.14	0.22	0.28	0.34	0.39

TABLE I: Mass (m), binding energy (E_{bd}) and radius (r) of quarkonium states [32].

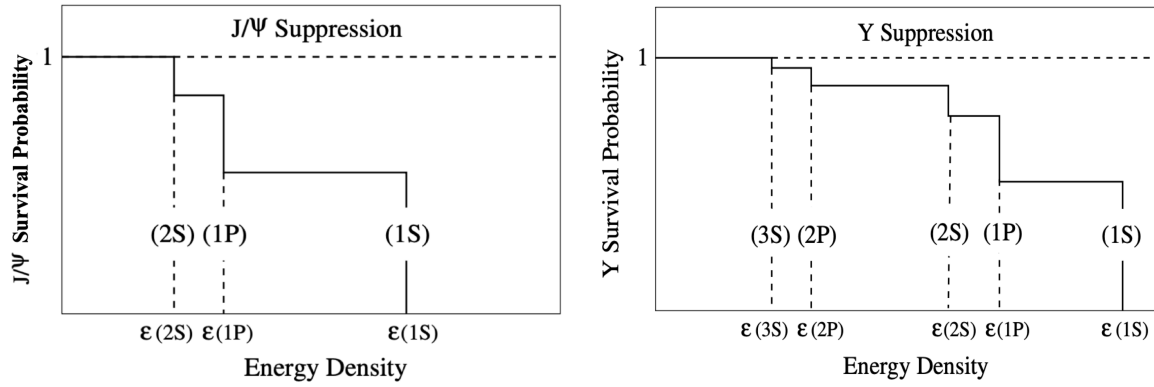


Figure 12: An illustration of sequential suppression pattern of charmonium states (left) and bottomonium states (right) [32].

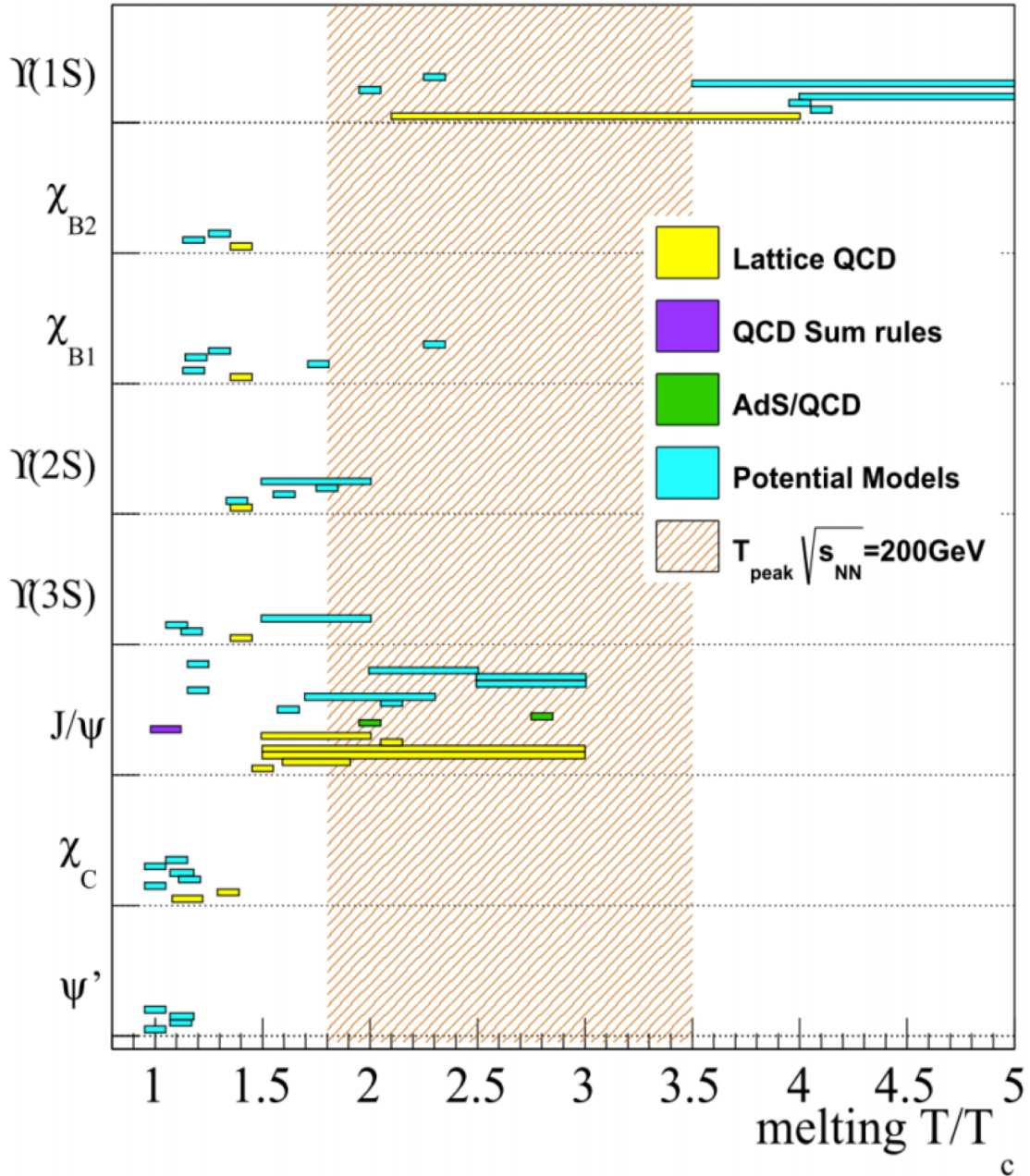


Figure 13: A summary of quarkonium dissociation temperatures T_{diso} predicted from different theoretical calculation [33]. The horizontal bars denote a temperature ranges where the quarkonium state experiencing a mass or size evolution. Quarkonium states are predicted to completely melt when temperatures are above the right end of the bars.

Regeneration (Recombination): The regeneration phenomenon mainly considers a possibility that heavy quarks may recombine together and form a quarkonium state while the system cools down. In nuclear-nuclear collisions, heavy quark production rate increases with the number of binary nucleon-nucleon collisions (N_{coll}), while the light quark production rate increases with the number of participant nucleons (N_{part}). Where N_{coll} grows much faster than N_{part} with the centrality of nuclear-nuclear collisions. Therefore the relative production ratio of heavy quarks over light quarks is much higher in more central nuclear-nuclear collisions. Such an excess of heavy quarks over light quarks leads to an enhancement of quarkonium production due to the regeneration or recombination possible. Besides the density of heavy quarks, the regeneration rate should also depend on geometrical expansion of QGP and the kinematic distributions of these heavy quarks. The final quarkonium production, due to the presence of hot medium, thus relies on the competition between the mechanisms of dissociation and regeneration, as illustrated in Figure 14.

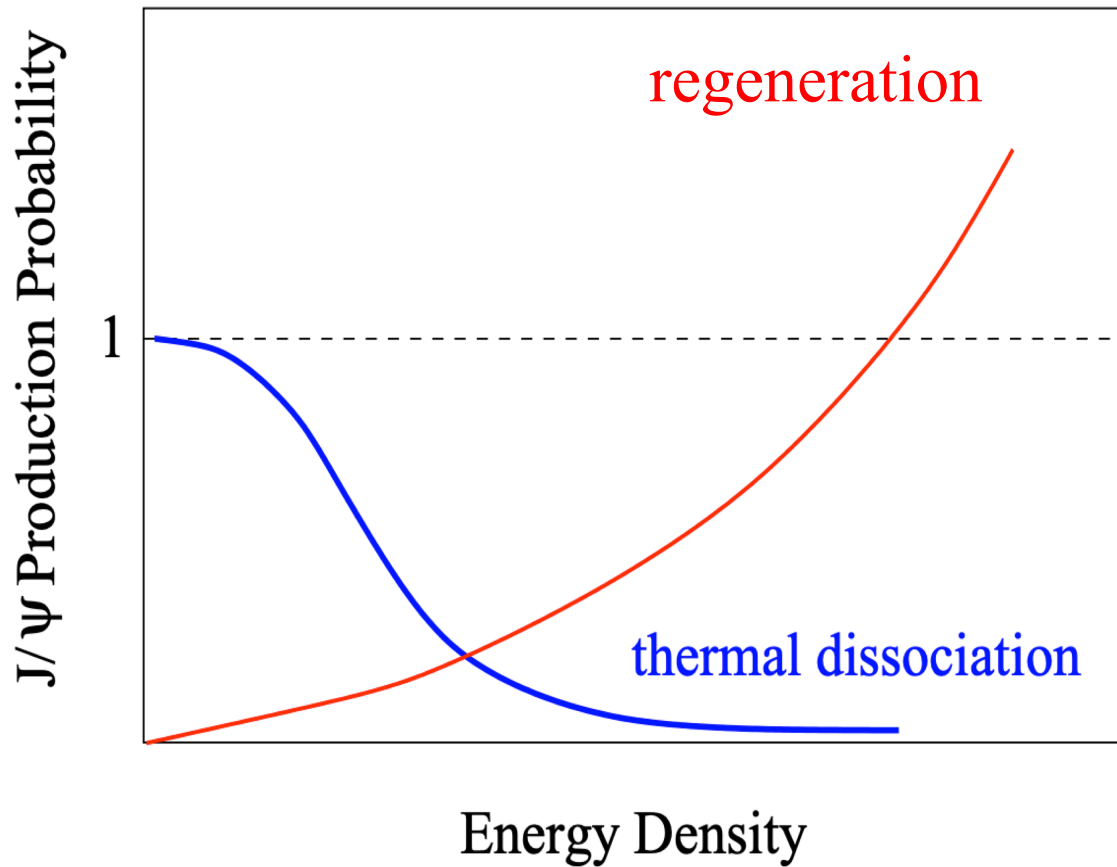


Figure 14: An illustration of J/ψ production probability (thermal dissociation and regeneration) as a function of energy density [32].

Cold nuclear matter effects: While we are focusing on quarkonium suppression due to the hot nuclear matter effects, on the other hand, the cold nuclear matter effects also play an important role on the quarkonium production. The cold nuclear matter effects include nuclear

PDF (nPDF) effects, Cronin effect and Nuclear absorption. The nPDF effect originates from the modification of the parton distribution functions in the nucleus (nPDFs) relative to the free nucleons. The effect of nPDFs including shadowing, anti-shadowing, EMC and Fermi motion effects. A ratio of PDFs between nuclear and proton can be used to characterize these effects, which is called the nuclear shadowing functions R_i^A (i denotes parton, A is the nuclear type), as illustrated in Figure 15. Typically, the shadowing effect corresponds to the small x range ($x < 0.025$) with $R_i^A < 1$; the anti-shadowing effect corresponds to the intermediate x range ($0.025 < x < 0.3$) with $R_i^A > 1$; EMC effect corresponds to the large x range ($0.3 < x < 0.8$) with $R_i^A < 1$; and the Fermi motion effect corresponds to the high x range ($x > 0.8$) with $R_i^A > 1$. The parameterization of nuclear modifications has been performed under the different models: HKN07 [34], EKS98 [35], EPS09 [36]..., an example of nuclear modifications for Lead under EPS09 frame is shown Figure 16.

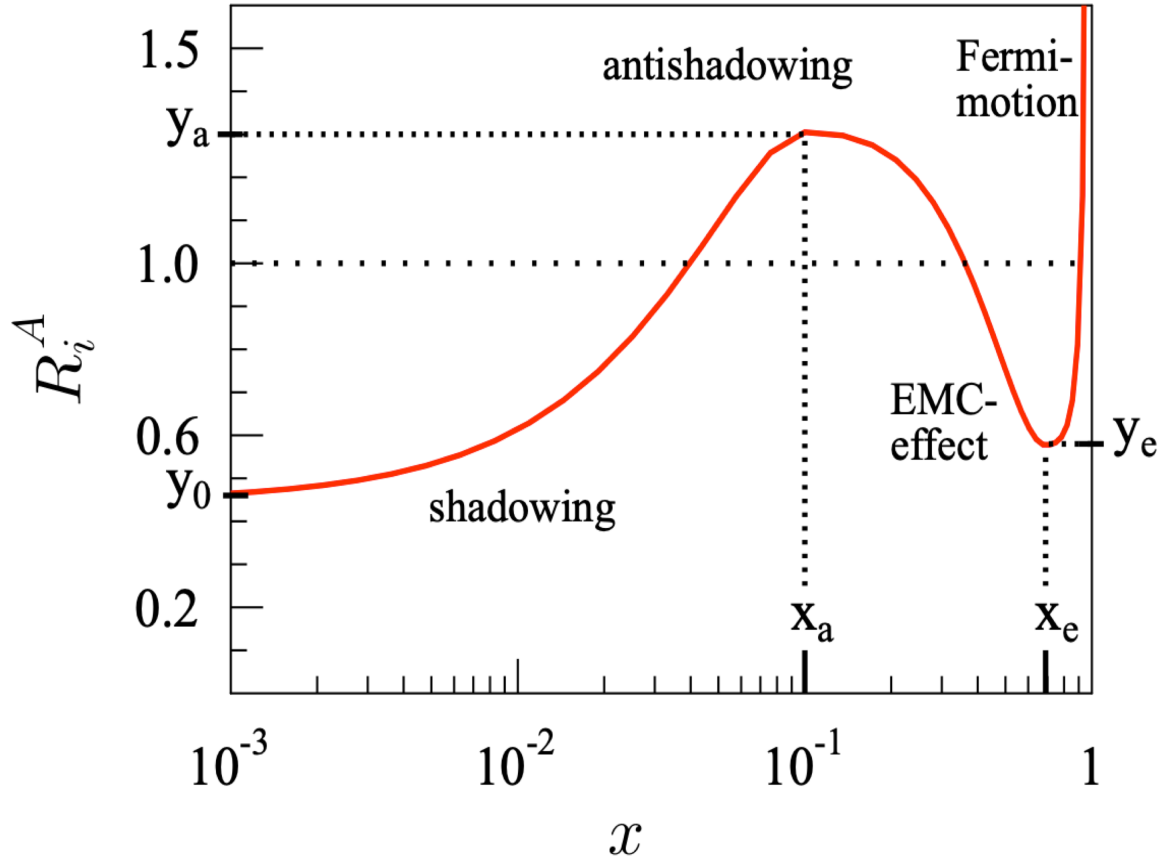


Figure 15: An illustration [36] of nuclear shadowing function R_i^A . Where, y_0 is the value shadowing level goes to as $x \rightarrow 0$; x_a , y_a are the coordinates of the anti-shadowing maximum ; x_e , y_e are coordinates of the EMC minimum.

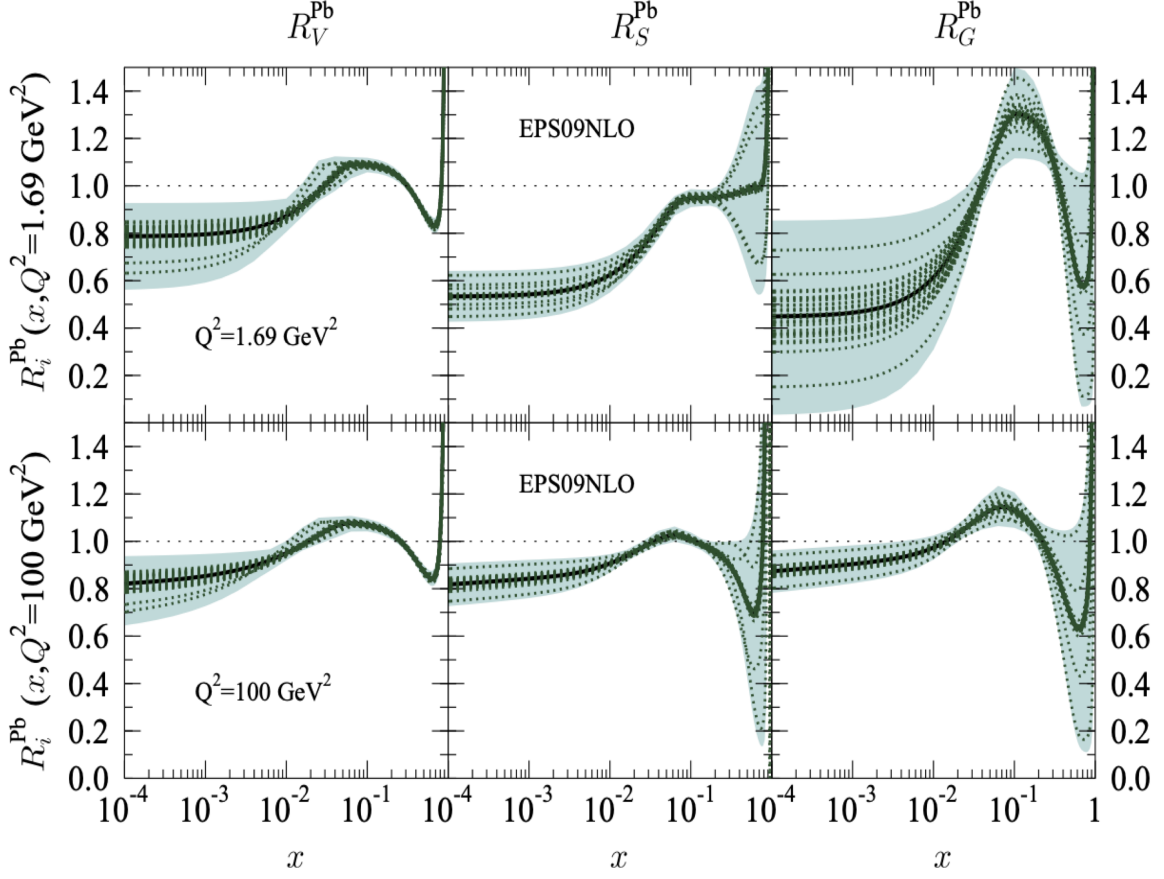


Figure 16: The EPS09 [36] nuclear modifications for Lead at the parameterization scale $Q^2 = 1.69 \text{ GeV}^2$ (upper) and $Q^2 = 100 \text{ GeV}^2$ (bottom). The left, central and right columns are corresponding to the valence quarks, sea quarks and gluons, respectively. Where the best-fit results are shown in black lines, the error sets are shown in dotted green curves.

At RHIC and LHC energies, the main source for the creation of heavy quark pairs is the gluon fusion $g+g \rightarrow Q\bar{Q}+g$. Before two gluons fuse into a stable quarkonium state, they acquire additional transverse momentum via the multi-scattering with their surrounding nucleons, such an extra transverse momentum would be inherited by the later formed quarkonium, thus leads to a broadening of transverse momentum distributions of quarkonium in proton+nucleus and nucleus+nucleus collisions with respect to what in proton+proton collisions. Such an effects are called the Cronin effect [37]. Another cold nuclear matter effect named “Nuclear” absorption [38,39] may also play a role on the quarkonium suppression. It states that pre-quarkonia states or quarkonia states could dissociate through the interactions with their neighbor nuclei right after their formation. The probability P_{abs}^s for a quarkonia state to survive in a nucleus, for a p+A collision, can be expressed as $P_{\text{abs}}^s = \exp(-\rho_{\Lambda}\sigma_{\text{abs}}L)$, where ρ_{Λ} is the nuclear density; σ_{abs} is the absorption cross section which stands for the probability of a quarkonia been broke up through the inelastic scattering with a nucleon; and L is the path length of a quarkonia inside the nuclear.

In order to explain the suppression of charmonium production and the enhancement of strangeness production in the nucleus+nucleus collisions at SPS, a theoretical approach named “Comover model” was developed in 1990s [40–42]. This model takes into account both mechanisms of dissociation and recombination for the quarkonium production, where the quarkonium

dissociation is assumed to be resulted from the interactions with the co-moving medium. The evolution of quarkonia can be expressed by a gain-and-loss differential equations:

$$\tau \frac{dN_{QM}}{d\tau}(\mathbf{b}, s, \mathbf{y}) = -\sigma_{co}[\rho_{med}^{co}(\mathbf{b}, s, \mathbf{y})N_{QM}(\mathbf{b}, s, \mathbf{y}) - N_Q(\mathbf{b}, s, \mathbf{y})N_{\bar{Q}}(\mathbf{b}, s, \mathbf{y})], \quad (1.5)$$

where, τ is proper evolution time, \mathbf{b} is the impact parameter, s is the squared center-of-mass energy, \mathbf{y} is rapidity, σ_{co} is the cross section of quarkonium dissociation due to their interactions with the co-moving medium, ρ_{med}^{co} is the medium density. The first term of above equation corresponds to the quarkonium dissociation while the second term refers to the recombination of a $Q\bar{Q}$ pair into a quarkonium state.

The survival probability of quarkonia can be obtained from the approximate solution of the above equation as:

$$P_{co}^S = \exp\left\{-\sigma_{co}\left[\rho_{med}^{co}(\mathbf{b}, s, \mathbf{y}) - \frac{N_Q(\mathbf{b}, s, \mathbf{y})N_{\bar{Q}}(\mathbf{b}, s, \mathbf{y})}{N_{QM}}\right]\ln\left[\frac{\rho_{med}^{co}(\mathbf{b}, s, \mathbf{y})}{\rho_{pp}(\mathbf{y})}\right]\right\} \quad (1.6)$$

The interactions with medium will stop when the medium density is diluted to be same as the proton density. The suppression of quarkonium under the comover model frame thus depends on the medium density and the proper time of dilution. Without introducing any QGP effects, the comover model consistently described experimental measurements from RHIC to LHC energies. Although, today we learned that QGP played a dominant role on the quarkonium dissociation in heavy-ion collisions, the dissociation due to interactions with co-moving medium may still need to be taken into account.

1.5 Goal this Thesis

In this thesis, Υ are measured in p+p, p+Au and Au+Au collisions with the STAR experiment at RHIC energy. The goal is to explore properties of QGP created at RHIC, via the measuring the suppression of Υ production in Au+Au collisions with respect to the Υ production in p+p collisions. The Υ measurements in p+p collisions serves as a reference, where no any hot medium (QGP) effects or cold nuclear matter are expected to exist. However, before the fully understanding of the Υ suppression in Au+Au collisions, the contribution from cold nuclear matter essentially needs to be studied. In order to disentangle the contributions of cold nuclear matter effects from the hot nuclear matter effects, the Υ production in p+Au collisions is also measured.

1.5.1 Previous Measurements

The first suppression of three individual Υ states was measured by CMS experiment [43,44], in Pb+Pb collisions at $\sqrt{s_{NN}} = 2.76$ TeV within a rapidity range $|y| < 2.4$. The centrality integrated nuclear modification factors (R_{AA}): $R_{AA}^{\Upsilon(1S)} = 0.56 \pm 0.08(\text{stat.}) \pm 0.07(\text{syst.})$, $R_{AA}^{\Upsilon(2S)} = 0.12 \pm 0.04(\text{stat.}) \pm 0.02(\text{syst.})$, and $R_{AA}^{\Upsilon(3S)} = 0.03 \pm 0.04(\text{stat.}) \pm 0.01(\text{syst.}) < 0.10$ (95%CL) (an upper limit of $R_{AA}^{\Upsilon(3S)}$ with 95% confidence level is given for $\Upsilon(3S)$, due to its strongly suppression), which show a clear ordering with their binding energies and is consistent with the sequential melting expectation. The $\Upsilon(nS)$ R_{AA} as a function of centrality is shown in Figure 17. As one can see, the $\Upsilon(1S)$ and $\Upsilon(2S)$ are suppressed more towards the more central collisions, while $\Upsilon(3S)$ are completely suppressed. The $\Upsilon(1S)$ R_{AA} measured within a rapidity range $2.5 < y < 4$ (forward rapidity) by ALICE experiment [45] is shown in black rhombus

which are slightly lower than CMS data points, suggesting that $\Upsilon(1S)$ is more suppressed at forward rapidity than at mid rapidity.

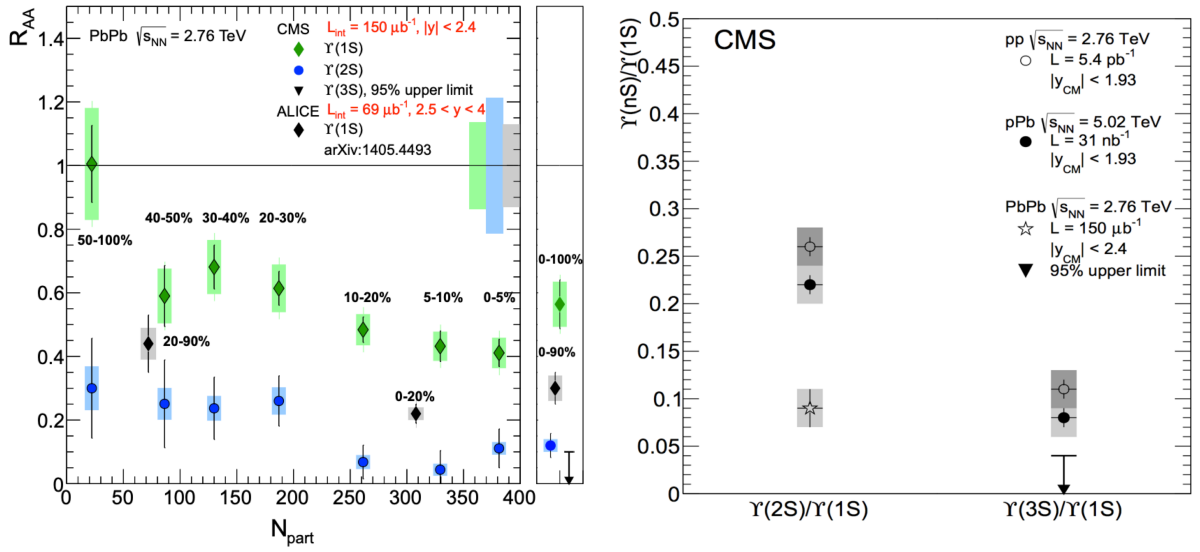


Figure 17: The left panel shows the ΥR_{AA} as a function of centrality (or N_{part}) measured in Pb+Pb collisions at $\sqrt{s_{NN}} = 2.76$ TeV by CMS [43,44] and ALICE experiments [45]. The right panel shows the ratios of $\Upsilon(2S)$, $\Upsilon(3S)$ over $\Upsilon(1S)$ measured in p+p ($\sqrt{s} = 2.76$ TeV), p+Pb ($\sqrt{s} = 5.02$ TeV), Pb+Pb ($\sqrt{s} = 2.76$ TeV) collisions by CMS experiment [46].

The right panel of Figure 17 shows the ratios of $\Upsilon(2S)$, $\Upsilon(3S)$ over $\Upsilon(1S)$ measured in p+p, p+Pb, Pb+Pb collisions with CMS experiment [46]. The ratios in pPb collisions are slightly lower than that in pp collisions, as the initial-state effects are canceled, may suggest

the final-state effects in pPb collisions affect more strongly on the excited states compared to ground state than in pp collisions. The ratios in PbPb collisions are clearly lower than that in pPb collisions, it may help to extract the contributions of final-state mechanism from cold and hot nuclear medium effects. Note that all current $\Upsilon(1S)$ measurements include both the directly production and the feed-down contributions from higher bottomonium states, a further understanding of the feed-down contributions is needed to evaluate the suppression of direct $\Upsilon(1S)$.

The previous Υ suppression at RHIC are studied in Au+Au collisions (by STAR [47] and PHENIX [33]) at $\sqrt{s_{NN}} = 200$ GeV, U+U (by STAR) [48] at $\sqrt{s_{NN}} = 193$ GeV, d+Au collisions (by STAR [47] and PHENIX [49]) at $\sqrt{s_{NN}} = 200$ GeV. The previous R_{AA} from these measurements are shown in left panel of Figure 18, the uncertainties of R_{AA} from PHENIX in Au+Au collisions and STAR in U+U collisions are too large, it is hard to draw any conclusion from them. The R_{AA} from STAR in Au+Au collisions have the best precision tend to indicate a less suppression than that at LHC, however it is still hard to see any centrality dependence while considering the uncertainties. In the right panel, the R_{dAu} from STAR [47] and PHENIX [49] are compared to different model calculations. As one can see, the uncertainties of all these data points are too large to give a clear message.

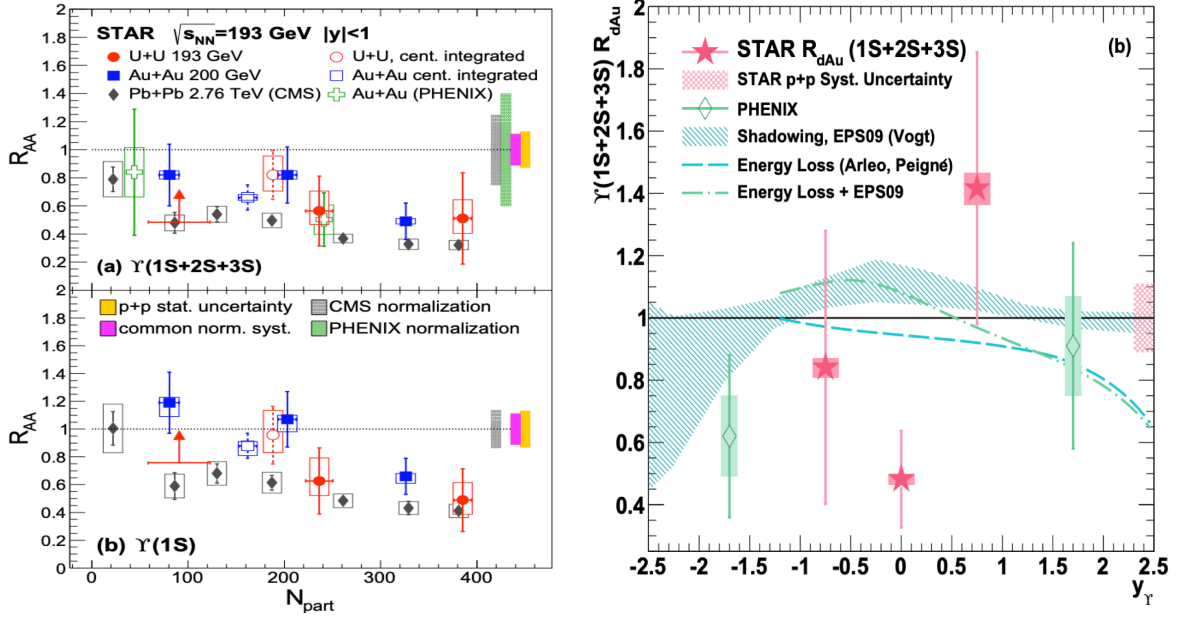


Figure 18: The left panel shows the $R_{AA}^{\gamma(1S+2S+3S)}$ and $R_{AA}^{\gamma(1S)}$ measured in Au+Au [47] [33] ($\sqrt{s_{NN}} = 200$ GeV), U+U [48] ($\sqrt{s_{NN}} = 193$ GeV) collisions at RHIC compared to that from CMS experiment at LHC [44]. The right panel shows the $R_{dAu}^{\gamma(1S+2S+3S)}$ measured at RHIC [47] [49] compared different model calculations.

CHAPTER 2

EXPERIMENTAL SETUP

2.1 Relativistic Heavy Ion Collider (RHIC)

The Relativistic Heavy-Ion Collider (RHIC) at Brookhaven National Laboratory (BNL), Upton City, New York, USA is one of the most powerful heavy-ion colliders in the world. The studies at RHIC attract world-wide interests among physicists from nuclear physics, particle physics, astrophysics, condensed matter physics and cosmology. One of the most important goal of RHIC is to study the properties of Quark Gluon Plasma for the understanding of how matter behaved at the initial stage of our universe shortly after the Big Bang. Another important goal of RHIC is to explore the mystery of the proton spin. Since it is well known that protons are made of three light quarks and are held tightly together by gluons, the spin of proton has long been believed to be simply sum of its three component quarks. However, the contribution from three component quarks on the total proton spin are found to only account for about 25 ~ 30% of the proton spin by experiment. RHIC is the only high energy collider in the world which could collide the spin-polarized protons, thus it provide an unique and excellent opportunity to study what accounts for the other 70 ~ 75% of proton spin. At RHIC, different types of particle collisions can be performed: proton+proton (p+p), proton+aluminum (p+Al), proton+gold (p+Au), deuterium+gold (d+Au), helium+gold ($^3\text{He}+\text{Au}$), copper+copper (Cu+Cu), copper+gold (Cu+Au), zirconium+zirconium (Zr+Zr), ruthenium+ruthenium (Ru+Ru), gold+gold

(Au+Au) and uranium+uranium (U+U). The collision energy per nucleon pair can be accelerated to from lowest 7.7 GeV up to 510 GeV.

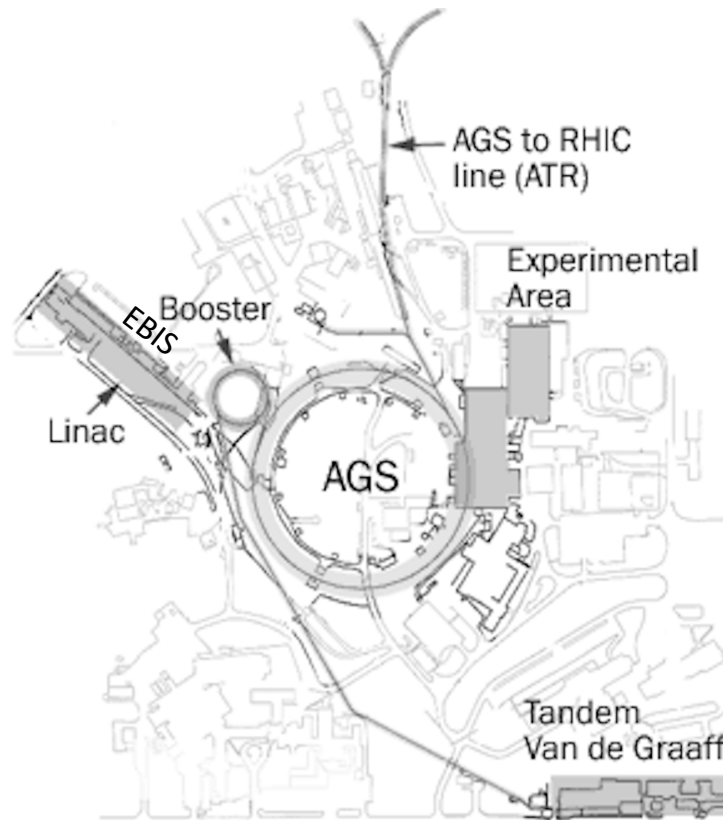


Figure 19: The pre-injection facility of the Tandem Van de Graaff (Tandem), the Electron Beam Ion Source (EBIS) and the BNL Linear Accelerator (Linac) [50].

Before these heavy ions are injected into RHIC rings, they start their journey from the Tandem Van de Graaff which is an electrostatic accelerator (15 million volt) facility at BNL

serving as an ion source for RHIC. At the Tandem Van de Graff facility, atoms are thermally ejected to pass through a low electronegative material, a grid made of cesium, which will donate electrons to the atoms. These negatively charged atoms could be accelerated by electric field. After accelerated to a higher speed, these atoms will pass through the stripping foils where electrons of these atoms will be removed. These ions will then be delivered to the Alternating Gradient Booster through the Tandem to Booster Line (a 700 meter long tunnel). The Alternating Gradient Booster will remove more electrons from heavy ions and accelerate them before sending them to the Alternating Gradient Synchrotron (AGS). The AGS has earned researchers three Nobel Prizes and today serve as the injector for RHIC.

After 2012, the Electron Beam Ion Source (EBIS) replaced the Tandem Van de Graff as a new pre-injection source. EBIS has significantly better performance than the Tandems. Different from the Tandem, in EBIS the electrons are stripped away from nuclei by the kinetic scattering with the electron beams, thus it does not suffer from the constrain of electronegativity of atoms and it can provide all stable ion species from deuterons to uranium. Moreover, EBIS can switch different ion beams to the Booster on a timescale of one second providing a much better operational flexibility than Tandems. Different to the other heavy ions, protons are pre-accelerated by the Brookhaven Linear Accelerator (Linac) before injected to the AGS. Linac include ion sources, a radiofrequency quadropole, and nine accelerator radiofrequency cavities. The protons can be accelerated to an energy of 0.2 GeV and then directly delivered to AGS.

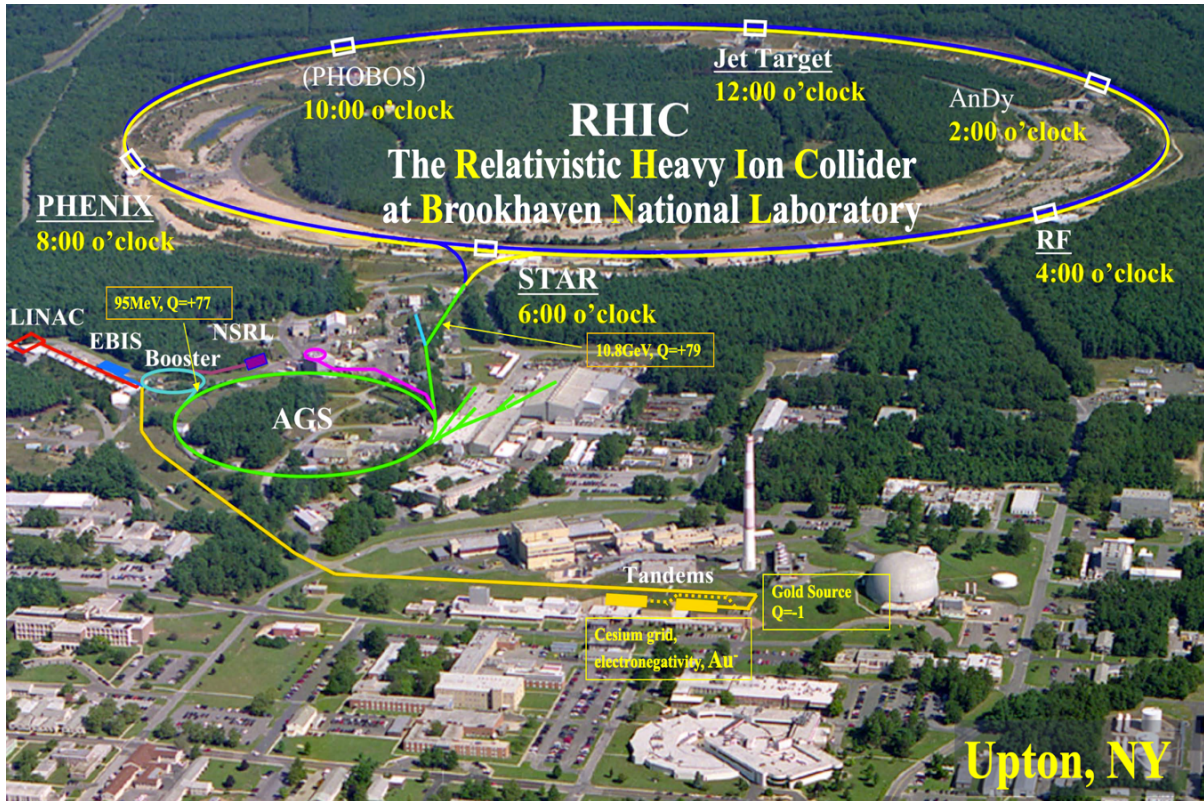


Figure 20: The Relativistic Heavy-Ion Collider (RHIC) and its complex supporting infrastructure [51].

Figure 20 is an overlooking of RHIC, there are two independent rings named “Blue Ring (clockwise)” and “Yellow Ring (counter-clockwise)” as shown in left panel of Figure 21. Each ring is about 3.834 km hexagonally shaped storage ring. The curved edges along each storage ring could deflect and focus the particles by the superconducting magnets. The magnets could provide a modest field of about 3.45 Teslas in the arc dipoles. The magnetic flux within the arc dipole coil and yoke are shown in the right panel of Figure 21.

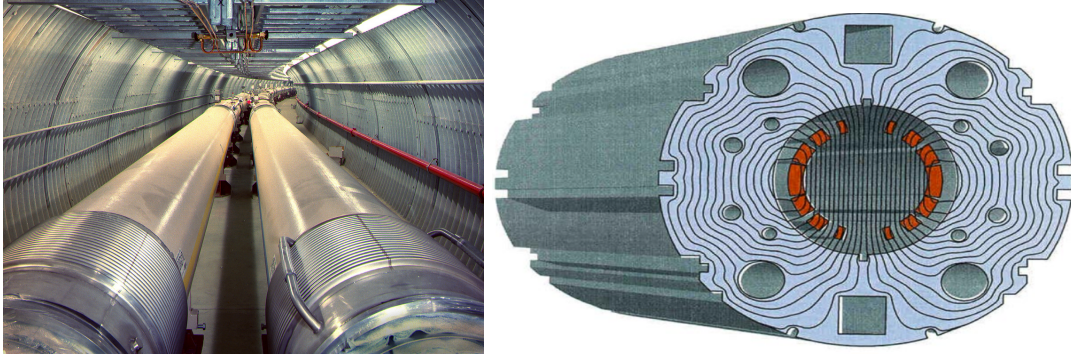


Figure 21: The left panel is the twin accelerators of RHIC [52], and the right panel is the Arc dipole coil and yoke, the curves are illustration of magnetic flux lines [53].

The heavy ions or polarized protons can be accelerated to nearly the speed of light and circulate in opposite directions in the two storage rings. They can collide with each other at the 6 interaction points along the RHIC rings. Among these interaction points, four experiments were built: STAR, PHENIX, PHOTOS and BRAHMS. If enumerate the positions of these experiments by the clock positions, STAR experiment is located at 6 o'clock position and near the injection points of AGS to RHIC transfer line, PHENIX at 8 o'clock, PHOBOS at 10 o'clock and BRAHMS at 2 o'clock. Today, STAR experiment is the only RHIC experiment that operates.

2.2 Solenoidal Tracker at RHIC (STAR)

The Solenoidal Tracker at RHIC (STAR) [54] is a massive detector weighing about 1,200 tons, comprised of multiple sub-detector systems, each detector specializing in detecting certain types of particles or measuring the kinematic information. These STAR detector systems work together can collect key features of thousands of particles produced by each heavy ion collision,

provide an excellent environment to search for and study the properties of the Quark Gluon Plasma (QGP).

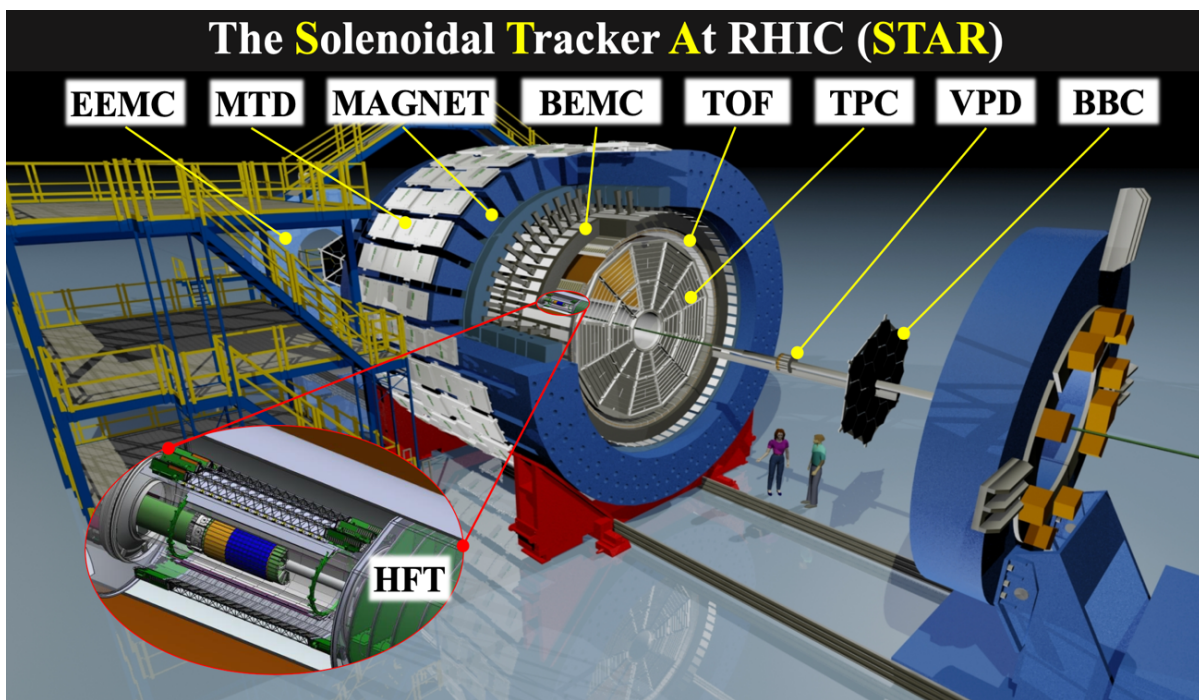


Figure 22: STAR detectors [54].

Figure 22 shows a schematic view of the STAR experiment. Each of the sub-detector systems are marked in the figure. The sub-detector system (TPC: Time Projection Chamber, TOF: Time-of-Flight detector, BEMC: Barrel Electromagnetic Calorimeter, EEMC: End-cap Electromagnetic Calorimeter, MTD: Muon Telescope Detector, HFT: Heavy Flavor Tracker,

BBC: Beam Beam Counter, VPD: Vertex Position Detector) are introduced in the following sections.

2.2.1 Time Projection Chamber (TPC)

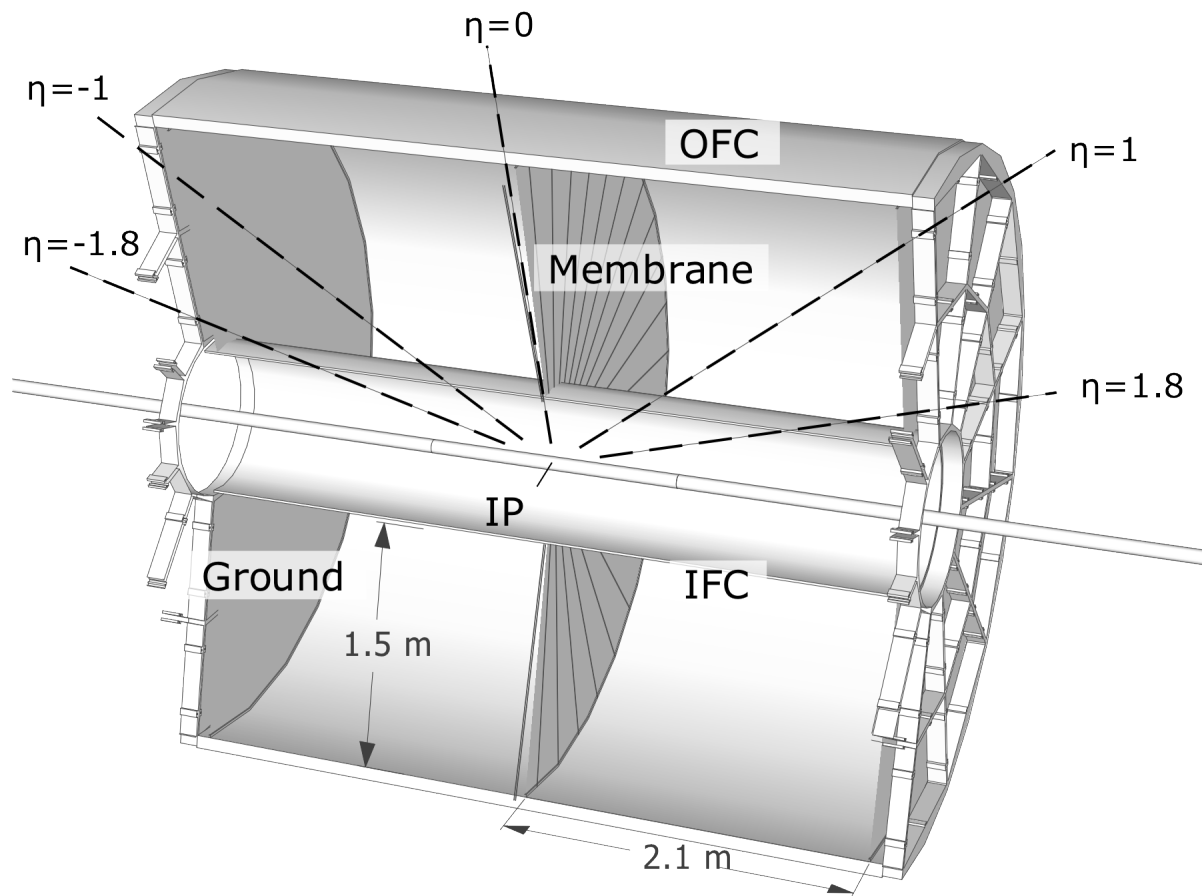


Figure 23: The schematic view of Time Projection Chamber (TPC) [55].

The Time Projection Chamber (TPC) is the main detector of the STAR experiment. The TPC provides excellent tracking, momentum and the ionization energy loss information of particles, covering a pseudo-rapidity range of $|\eta| < 1.8$ in the center-of-mass frame and full azimuthal (ϕ direction). The TPC sits inside a large, solenoidal magnet which can produce a 0.5 Tesla magnetic field oriented along the beam direction. Charged particles are deflected by this strong magnetic field, the transverse momentum of these particles thus can be obtained by looking at the curvatures recorded by TPC.

A schematic view of TPC is shown in Figure 23. TPC has a length of 4.2 meters along the beam line and a diameter of 4 meters. The TPC volume is filled with P10 gas (90% Argon + 10% Methane by volume) at ~ 2 mbar above the atmospheric pressure. As TPC is very large, the ionized electrons from a primary track may drift up to 2.2 meters before they finally arrive at the anode plane. So the the gas must not attenuate these electrons and it must be kept pure to prevent other modes of electron loss due to absorption on oxygen and hydrone. Noble gases are found to be good candidates. STAR choose to use the P10 gas, where the argon (Ar) gas has a very low affinity for free electrons while methane (CH_4) the could help to quench the propagation of ultraviolet (UV) photons. When a charged particle travel through the TPC gas, it will ionize the TPC gas atoms per few tens of a mm along its path and leave a cluster of electrons behind. These electron clusters will drift to the anode plane, driven by an external electric field provided by the field cage and the high voltage central membrane. The field cage includes the outer field cage (OFC) and inner field cage (IFC), could provide a perfect uniform electric field to drift electrons. Any distortions of the electric field will result in a distortion of

recorded trajectories of these charged particles. The field cage also help to prevent the TPC gas from being contaminated by the outside air. The high voltage membrane (CM) is placed in the middle of the TPC perpendicular to the Beam line, held at a high voltage of $\sim 28\text{kV}$. At the end of TPC are the anode and pad planes as shown in Figure 25, where the pads are held at ground potential.

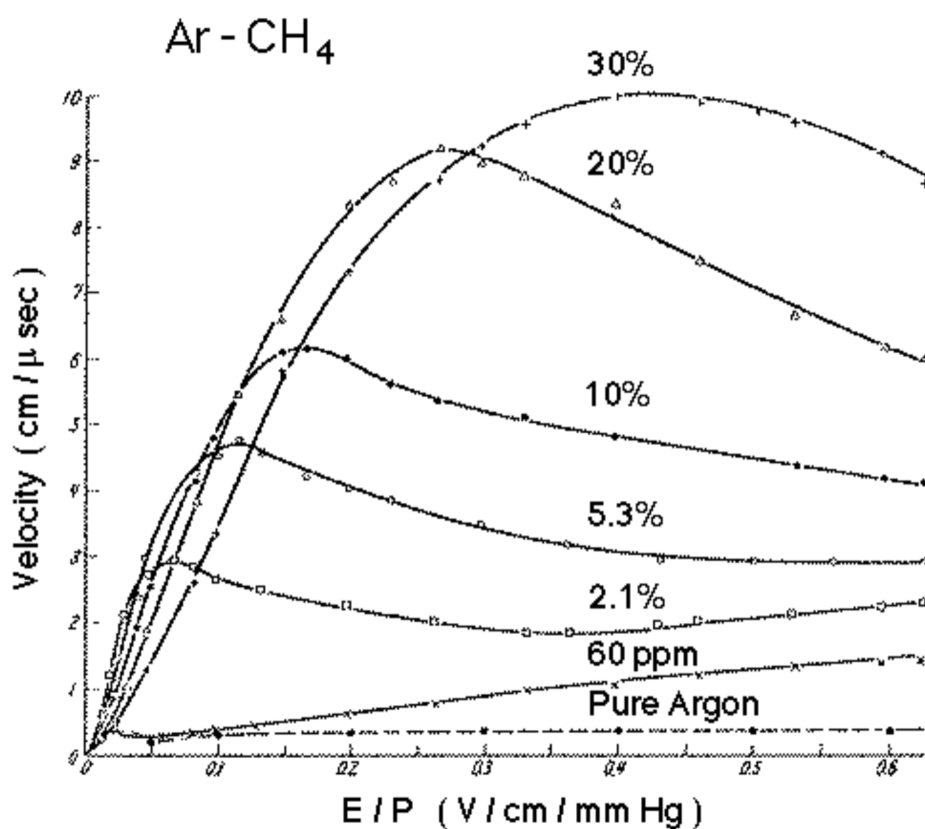


Figure 24: Drift velocity versus the reduced electric field E/p ($E \sim$ electric field, $p \sim$ gas pressure) [55].

The drift velocity depends on the strength of electric field and the gas composition, however it is not a linear dependence as shown in Figure 24. The magnitude of electric field is chosen to be close to the saturated drift velocity so that the drift velocity will be least sensitive to the variations of gas pressure or local temperature. To keep a stable drift velocity, TPC has an automatic stabilization feedback loop to adjust the electric field for any time dependent variations of TPC gas properties. It is realized by monitoring the drift of the laser tracks whose origin in time and space are known in advance. To better observe the changes of drift velocity and avoid the double valued solution problem, the operating drift velocity is therefore expected to be slightly off the peak. The operating drift velocity of TPC is ~ 5.45 cm/ μ s, and the corresponding electric field are set to be around 135 V/cm slightly higher than the peak value ~ 120 V/cm. After drifting the full length (210 cm) of TPC chamber in P10 gas under a magnetic field $B = 0.5$ Tesla, the transverse and longitudinal diffusion of electrons are measured to be $\sigma_T = 3.3$ mm and $\sigma_L = 5.2$ mm, respectively. The transverse diffusion sets a scale for $x - y$ plane of the readout system. The longitudinal diffusion on the other hand sets a scale for the tracking resolution in the drift direction.

At the end of TPC are the 12 sectors arranged as on a clock in each readout end cap. Figure 25 shows one TPC sector, which includes one outer sub-sector and one inner sub-sector. The outer sub-sector is composed of 3,942 large pads which are continuously arranged so that it could provide a good resolution for the energy loss (dE/dx). The inner sub-sector locates at a larger pseudo-rapidity where track density is much higher, is composed of 1,750 small pads for better two-hit resolution. Due to the constraint of available packing density of the front-end

electronic channels, these pads of inner sub-sectors are discontinuously arranged in separate rows.

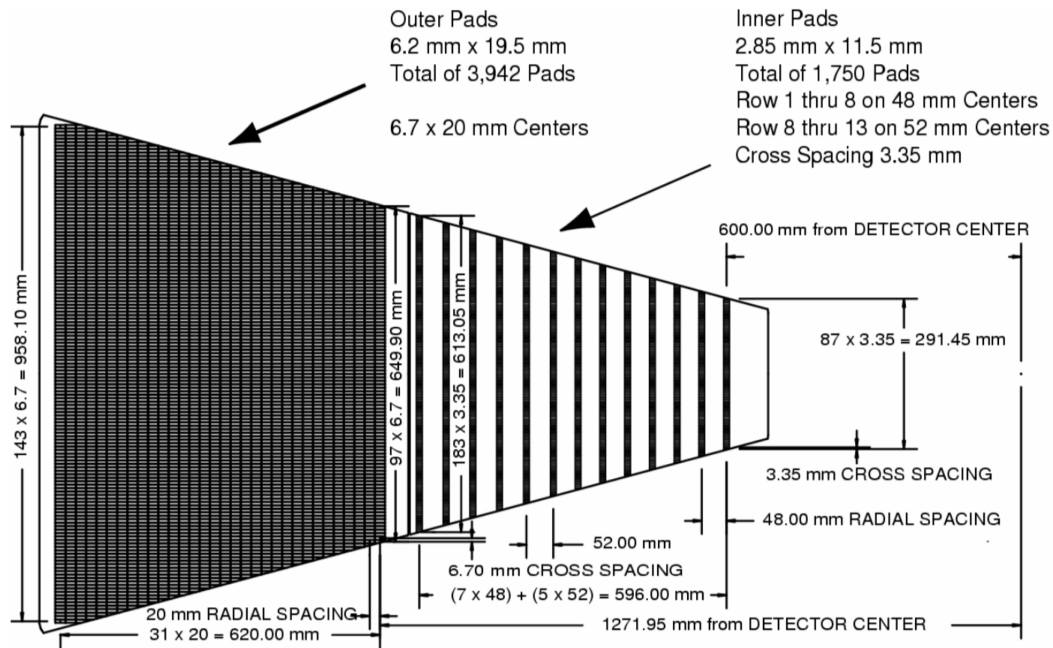


Figure 25: One anode pad sector of TPC. The full sector contains the inner subsector (1,750 smaller pads) and out subsector (3,942 larger pads) [56].

When the TPC gas are ionized by the charged particles, large number of electrons and positive ions will be released along the path of these charged particles. These electrons will drift to the end cap and be collected by the Multi-Wire Proportional Chamber (MWPC) composed of three wire planes (gating grid, ground plane and anode wires) and a pad plane. The gating

grid has two modes “close mode” and “open mode”. When the gating grid is on “open mode”, all of the wires are biased to the same potential ~ 110 V. When the gating grid is on “close mode”, these voltages are alternately changing between ± 75 V from the nominal value. As the ions are much heavier, they are too slow to escape during the “open mode” period, thus are captured during the “close mode” period. Once the electrons approaching the strong electric field region of MWPC, an avalanche will be triggered and produce more electrons which will then induce a signal on the readout plane. The position of ionization clusters along the trajectories of charged particles can be extracted from these induced signals. The x and y coordinates can be determined from the geometric distribution of induced signals on the pads, while the z coordinate can be determined by the product of drift velocity and drift time of the cluster from ionization position to the anode.

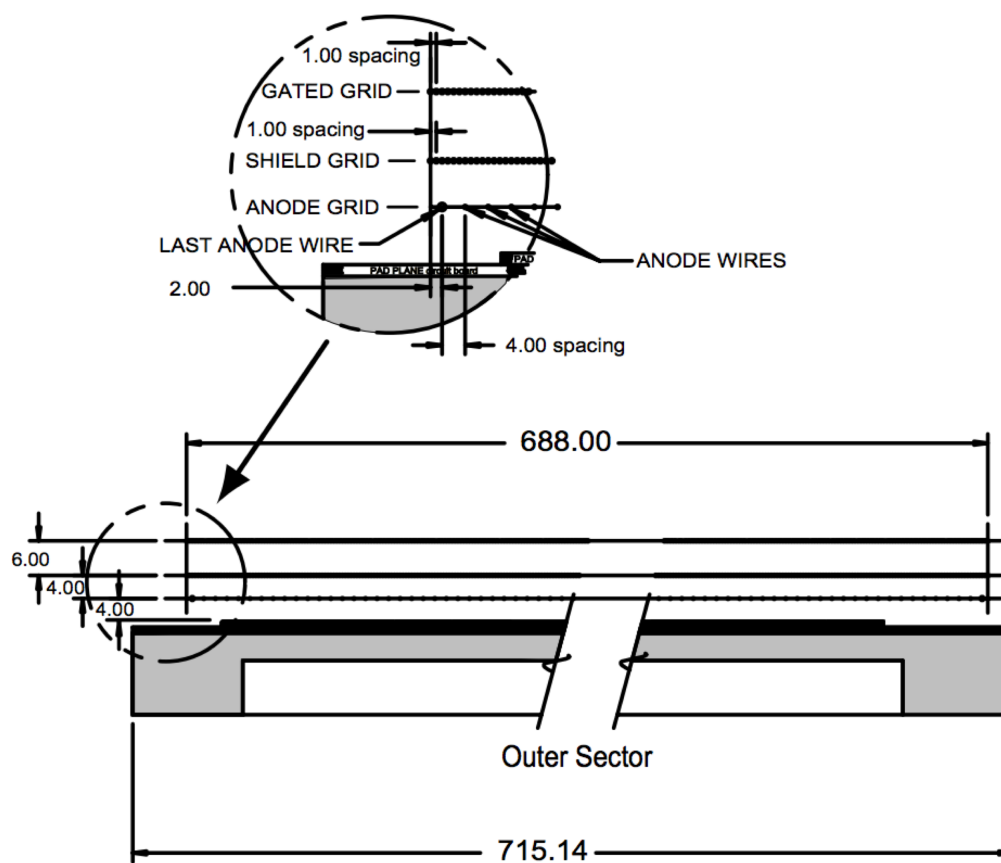


Figure 26: A side view of an TPC outer sub-sector pad plane. It shows the spacing of the anode wires relative to the gated grid, the ground shield grid and the pad plane. The additional details about the wire spacing are shown in bubble diagram. (All dimensions are draw in millimeters) [56].

The whole track of a particle is finally reconstructed from these individual clusters (usually named “hits” at STAR) via the Kalman filter algorithm [57–59]. These tracks are called global tracks. Once tracks are reconstructed, we can calculate the transverse momenta (p_T) of particles based on the curvatures of tracks and the magnetic field in the TPC volume. The initial primary vertex can be fitted based on those global tracks reconstructed with more than 10 hits. The Distance of Closest Approach (DCA) of each global track to the fitted primary vertex can be calculated. Based on those tracks with $DCA < 3\text{cm}$, another primary vertex position can be obtained by a new fit. Iterate the above procedures until the fitted vertex position converges. Finally those tracks with $Dca < 3\text{ cm}$ to primary vertex are defined as primary tracks, and the momentum associated with these tracks are re-fitted again while including the primary vertex point. The primary vertex resolution is proportional to $1/\sqrt{N_{\text{track}}}$ (N_{track} is the total number of available tracks in the fitting), a resolution of $\sim 350\ \mu\text{m}$ can be achieved for those events with ~ 1000 tracks.

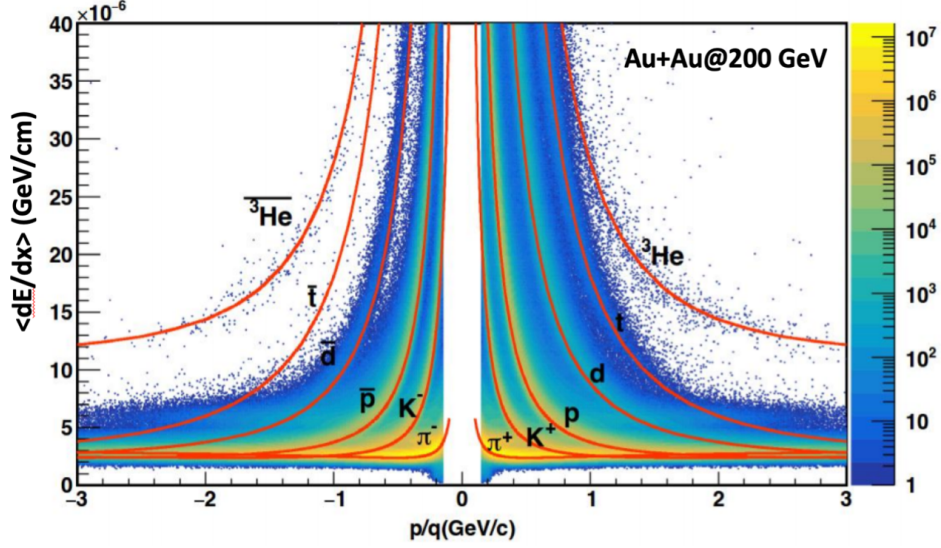


Figure 27: The truncated mean of the ionization energy loss $\langle dE/dx \rangle$ versus the rigidity p/q (p is the momenta, q is the charge) of different particles measured by TPC in Au+Au collisions at $\sqrt{s_{NN}} = 200$ GeV [60].

The ionization energy loss can be obtained by integrating the induced electrical signal amplitude of each cluster or hit. The information of ionization energy loss (dE/dx) of tracks measured can be used to perform the particle identification, as different particle has a different energy loss characteristics while interacting with TPC gas. An illustration of the truncated mean of the ionization energy loss $\langle dE/dx \rangle$ versus the rigidity p/q of different particles measured by TPC in Au+Au collisions are shown in Figure 27.

2.2.2 Time-of-Flight Detector (TOF)

The barrel Time-of-Flight (TOF) detector [61], consists of 120 trays, is installed just outside of STAR TPC, as one see in Figure 22. The barrel TOF detector covers a pseudo-rapidity range

of $|\eta| < 1$ and the full azimuthal angle. Each tray of TOF detector covers one unit of η and 6 degrees in azimuthal angle. Each TOF tray contains 32 Multi-gap Resistive Plate Chamber (MRPC) modules [62, 63] which is shown in Figure 28. There are 6 pads corresponding to 192 channels for each TOF tray, thus the full barrel TOF detector has 23040 (192x120) channels.

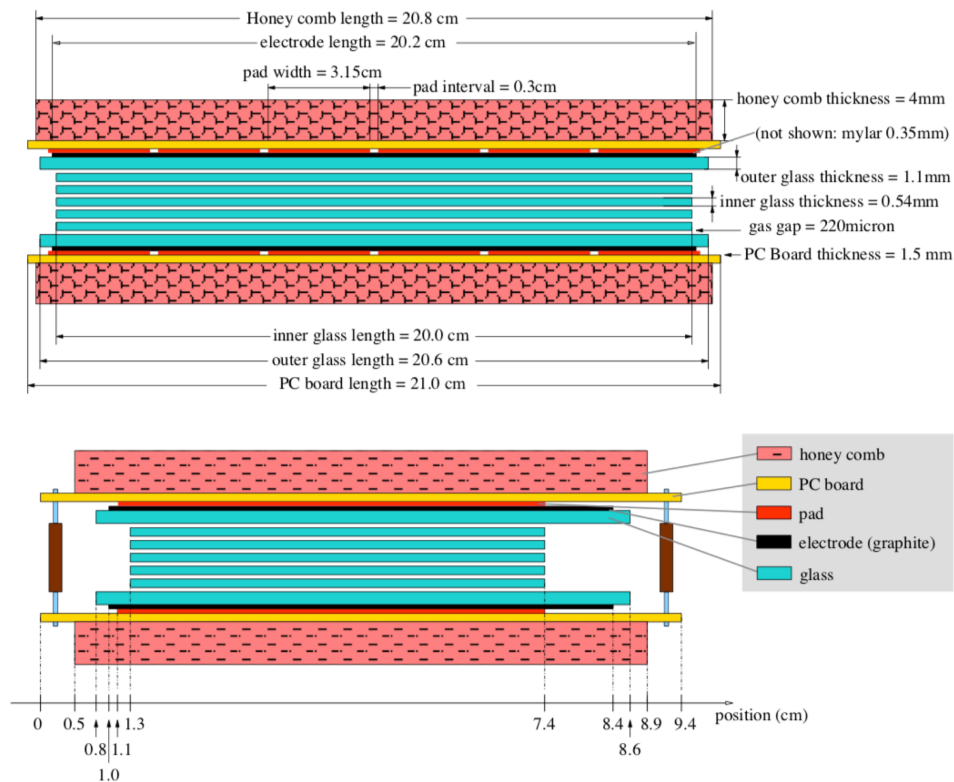


Figure 28: The front and back side views of Multi-gap Resistive Plate Chamber (MRPC) module [62, 63]. The STAR barrel Time-of-Flight detector (TOF) are comprised of MRPC modules.

The full TOF system consists of the barrel TOF detector and the VPD detector. The “start time”- t_0 is measured by VPD detector while the “stop time”- t_1 is measured by the barrel TOF detector. The time interval “time-of-flight” can be obtained as $\Delta t = t_1 - t_0$. The hits on the barrel TOF trays are then matched to the tracks constructed via TPC. By making use of the information of momentum p and track length Δs , the inverse velocity of $1/\beta$ can be calculate by $c \frac{\Delta t}{\Delta s}$, where c is the light speed. The mass of this charged particle can be calculated by $m = \frac{p}{c} \sqrt{1/\beta^2 - 1}$. Thus the particle identification (PID) via mass can be achieved with TOF detector. However, when the momentum of a particle goes too high, its velocity will be very close to the speed of light, thus the PID becomes more challenging at higher momenta. In Figure 29, the inverse velocity $1/\beta$ measured by STAR TOF detector versus the rigidity p/q in Au+Au collisions are shown, as one can see, the different particles show clearly separated curves.

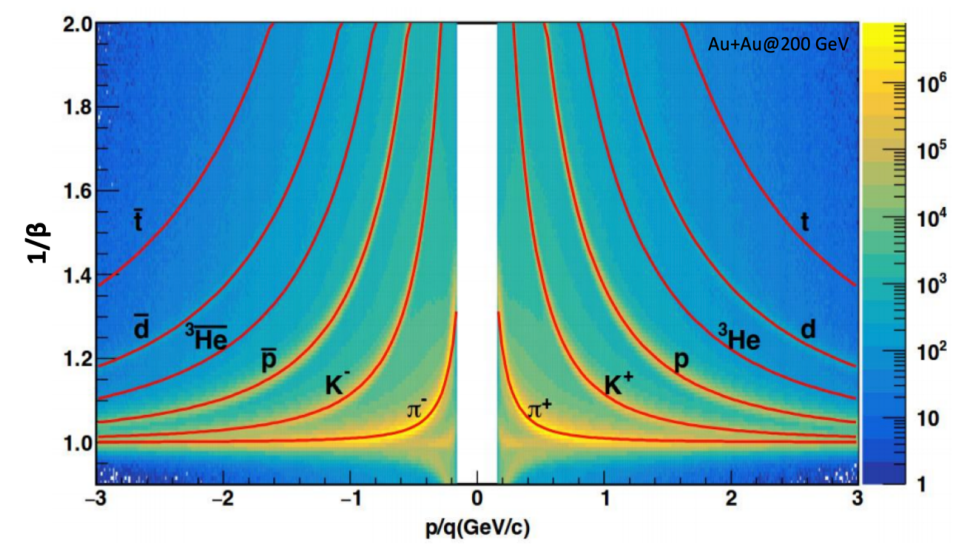


Figure 29: The inverse velocity $1/\beta$ measured by STAR TOF detector versus the rigidity p/q in Au+Au collisions at $\sqrt{s_{NN}} = 200$ GeV [60].

2.2.3 Barrel Electromagnetic Calorimeter (BEMC)

On top of the TOF detector and inside the aluminum coils of STAR solenoid sits the Barrel Electromagnetic Calorimeter (BEMC) [64]. BEMC covers a pseudo-rapidity range of $|\eta| < 1$ and the full azimuthal angle, thus fully matching the TPC tracking acceptance. A schematic view of BEMC is shown in Figure 30. BEMC consists of 120 calorimeter modules, each module can be segmented into 40 towers and subtending 6° in azimuthal angle and 1 unit of pseudo-rapidity, two towers in azimuthal direction and 20 towers in the η direction. There are 60 modules in $\eta > 0$ and $\eta < 0$ ranges. The full BEMC modules are segmented into 4,800 towers (120x40), each of which is pointing to the center of the interaction region as shown in the side view of a BEMC module in the left panel of Figure 31, while the right panel of Figure 31 shows

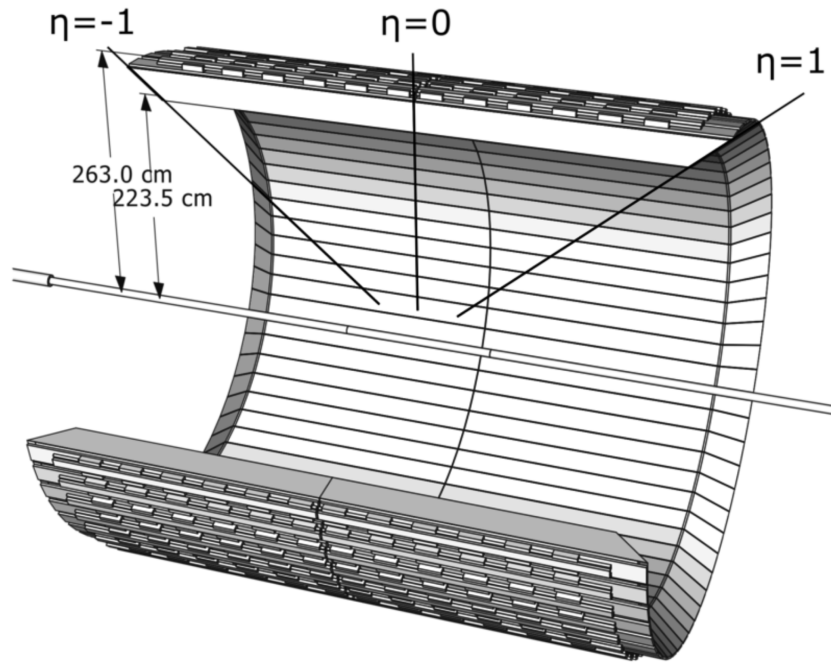


Figure 30: The perspective view of the Barrel Electromagnetic Calorimeter (BEMC) [64].

the end view of BEMC module. The plastic scintillators are mounted in a form of “megatile”, the 21st of them is illustrated in the left of Figure 31 .

Each module is composed of Barrel Shower Maximum Detecor (BSMD) and a lead scintillator stack. The BSMD is embedded in a depth of ~ 5 radiation lengths to the front of the stack. There are 20 layers of lead (5mm thick) and 21 layers of scintillator (19x5 mm thick + 2x6 mm thick), the 2 thicker scintillator layers are corresponding to the preshower detector as shown in Figure 32. Although the BEMC towers show a good energy resolution for electromagnetic showers, the much larger size of a tower than the size of an electromagnetic shower does not

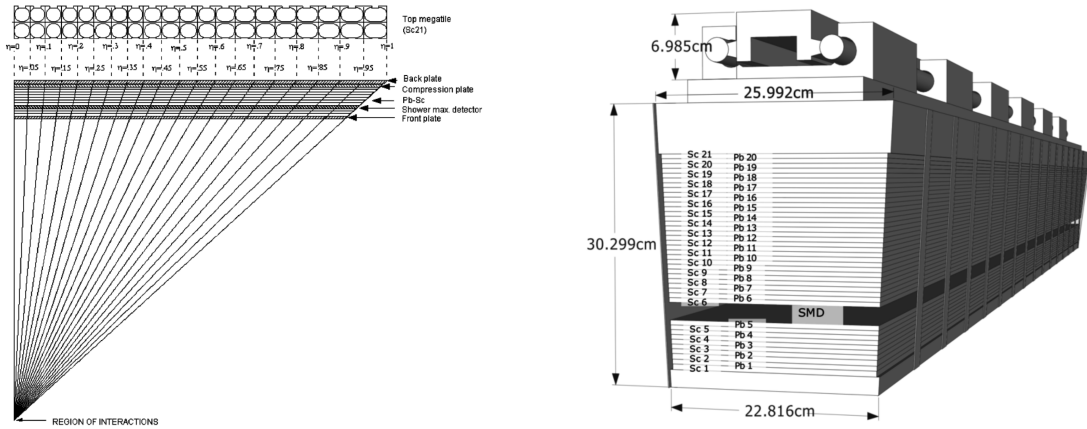


Figure 31: The side view (left) and end view (right) of a single BEMC module [64].

allow a good spatial resolution for these showers. The BSMD could provide a much better spatial resolution (a few mm), thus is very useful for the identification of electrons, π^0 s and the direct photons.

The readout response rate of the BEMC is very high to keep up with the RHIC collision rate ~ 9.35 MHz, thus BEMC is used as a triggering detector at STAR. BEMC can trigger on those events with high transverse energy particles, which is very useful to pre-select events during the online data taking. As the available readout rate of STAR detector systems is limited, BEMC serves as an efficient trigger for some specific physics analysis. Usually, hadrons deposit much lower fraction of their total energy than electrons, thus the precise measurement of the deposited energy of particles in BEMC can be used to separate electrons from hadrons.

2.2.4 Heavy Flavor Tracker (HFT)

The Heavy Flavor Tracker (HFT) [65] is composed of three sub silicon detectors: PiXeL detector (PXL), Intermediate Silicon Tracker (IST) and Silicon Strip Detector (SSD) as shown in Figure 33. The HFT sub detectors are concentric cylinders installed at the heart of the STAR detector system, which are closest to the center of the interaction region. The PXL are the two most inner layers of HFT, which is the first application of CMOS Monolithic Active Pixel Sensor (MAPS) technology in high energy experiments, and they are placed at a radius of 2.8 cm and 8 cm to the beam line. The IST is placed at a radius of 14 cm to the beam line, which is based on the single-side silicon pad sensors (pad size = 600 μm x 6 mm). The SSD is the outermost layer of HFT, placed at a radius of 22 cm to the beam line, which is based on double sided silicon strip sensors. The HFT greatly improved the resolution of the distance of closest approach (DCA) from $\sim 1\text{mm}$ (by TPC) to $\sim 250\text{-}300$ μm (by SSD and IST) and to ~ 30 μm (by PXL).

The left panel of Figure 34 shows the comparison of the transverse DCA of π as a function of momentum achieved by HFT compared to those from LHC experiments (ALICE, ATLAS, CMS). As one can see, for low momentum particles, STAR could achieve a much better DCA resolution, allowing reconstruction of secondary decay vertices of long-lived hadrons (D, B mesons ...). The right panel of Figure 34 shows the D^0 signal reconstructed via $D^0 \rightarrow K\pi$ decay channel in 2014 Au+Au collisions at $\sqrt{s_{\text{NN}}} = 200$ GeV. The small box shows the comparison of D^0 signals with and without HFT, the background is suppressed $\sim 10^4$ while with the HFT.

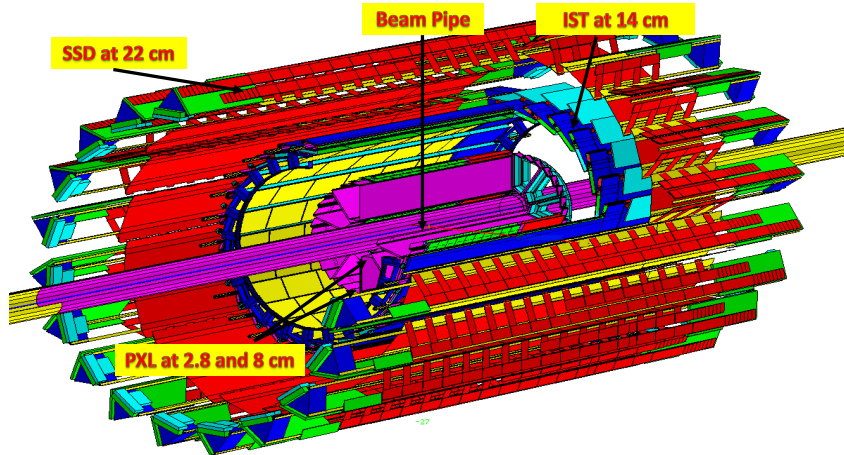


Figure 33: STAR Heavy Flavor Tracker (HFT) [65].

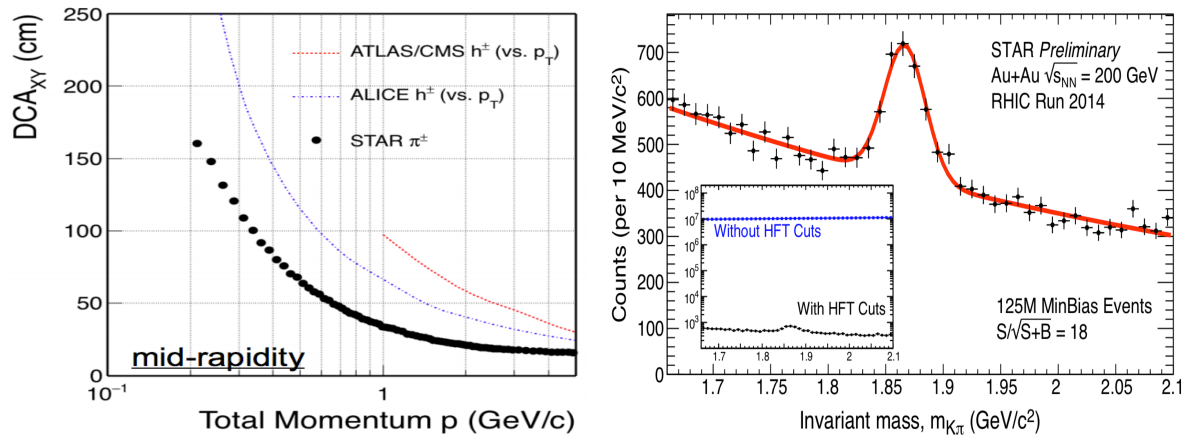


Figure 34: The performance of STAR HFT [66]. The left panel shows the transverse DCA of π^\pm measured by STAR compared to that from LHC experiments. The right panel shows the invariant mass of D^0 reconstructed in 2014 Au+Au collisions at $\sqrt{s_{NN}} = 200$ GeV. The small box shows the comparison of D^0 signals reconstructed with and without HFT.

2.2.5 Muon Telescope Detector (MTD)

The Muon Telescope Detector (MTD) [67] is installed at the most outside of STAR detector system. MTD covers the pseudorapidity range of $|\eta| < 0.5$ and 45% of the full azimuthal (ϕ) angle. The MTD detector is composed of multiple large Multi-gap Resistive Plate Chambers (LMRPC) which is mounted just on top of the BEMC electronic boxes as shown in the left figure of Figure 35. Below the BEMC electronic boxes are the STAR magnet flux-return bars which could help to remove most of the hadrons produced in the collision. The schematic view of the whole MTD system is shown in the right figure of Figure 35. The response efficiency of MTD can reach up to $\sim 85\%$ as determined via cosmic ray. MTD could achieve a timing resolution of ~ 108 picoseconds and a spatial resolution of 1.4 cm along the y direction (perpendicular to the MRPC strips of MTD) and 1.0 cm along the z direction (the beam axis direction). The installation of MTD allows to trigger on and identify muon at STAR.

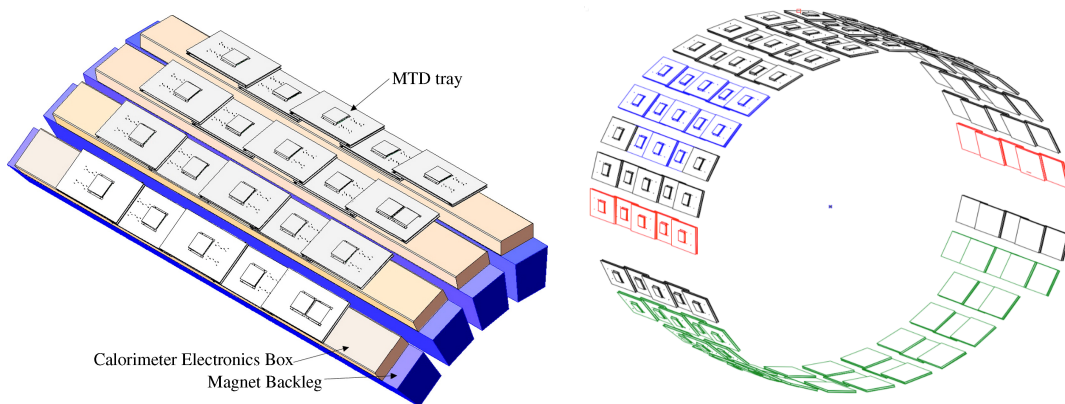


Figure 35: STAR Muon Telescope Detector (MTD) [67]. The MTD tray is installed on top of the BEMC electronic boxes. The right figure shows the schematic view of MTD system.

2.2.6 Vertex Position Detector (VPD)

The Vertex Position Detector (VPD) [68] can precisely measure primary vertex position along the beam direction and the “start time” of a collision. VPD is comprised of two assemblies which symmetrically locate at 5.7 meters away from the center of interaction region, where each assembly covers a pseudorapidity range of $4.24 < \eta < 5.1$. Each assembly contains 19 channels, the timing resolution of single channel in Au+Au collisions at $\sqrt{s_{NN}} = 200$ GeV is ~ 100 picoseconds, the entire VPD detector can achieve a timing resolution of ~ 30 picoseconds on the event start time and a position resolution of ~ 1 cm on the primary collision vertex along the beam direction. VPD is also fully integrated into the trigger system of STAR experiment and provides primary information for the minimum-bias trigger in heavy ion collisions.



Figure 36: STAR Vertex Position Detector (VPD) [68].

2.2.7 Beam-Beam Counter (BBC)

The Beam Beam Counter (BBC) [69] is composed of two identical detectors: BBC East and BBC West. Each BBC detector locates 3.75 meters away from center of the interaction region, around the beam pipe. Each BBC detector contains two inner and outer hexagonal annuli of scintillators. The inner annuli contains 18 smaller scintillator tiles while the outer annuli contains 18 larger scintillator tiles. The inner annuli and outer annuli cover a pseudorapidity range of $3.3 < |\eta| < 5$ and $2.1 < |\eta| < 3.6$ (The hexagonal shapes of inner annuli and outer annuli result in a slight overlap between them as shown in Figure 37.). BBC is very efficient on the detection of high-pseudorapidity particles and it serves as the main minimum bias trigger in p+p collisions for the STAR experiment. As a minimum bias (MB) trigger, at least one pair of coincidental hits between BBC East and BBC West detectors are required. The trigger efficiency on the total inelastic cross section excluding single diffraction processes in p+p collisions can reach up to 87%. Besides the MB trigger, the relative position of particles measured by BBC provide important information to determine polarizations of proton beams, thus be very useful for the study of proton spin structure.

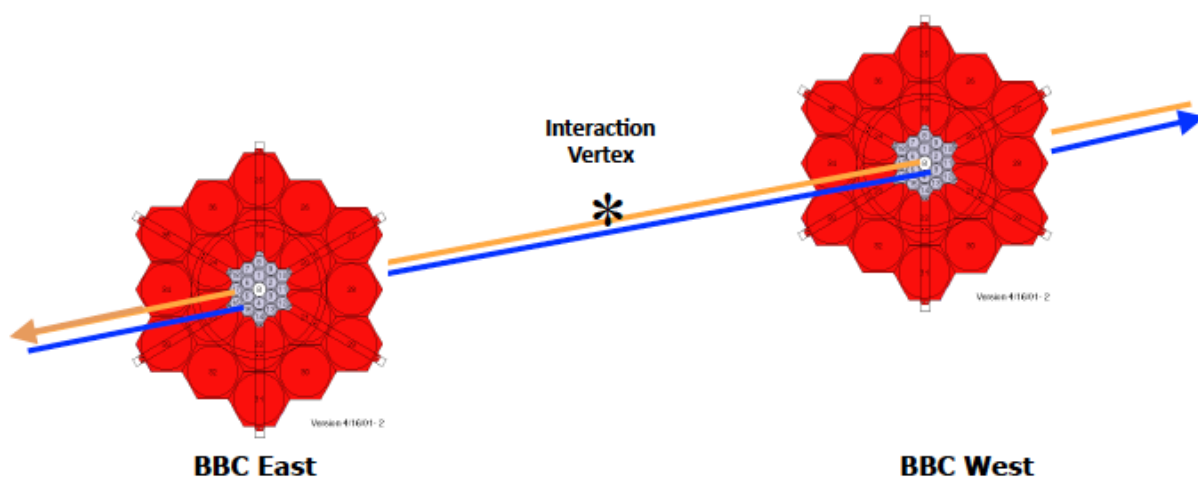


Figure 37: STAR Beam Beam Counter (BBC) [69].

CHAPTER 3

MEASUREMENTS OF UPSILON PRODUCTION IN P+P AND P+AU COLLISIONS

3.1 Upsilon Invariant Mass Reconstruction in Real Data

3.1.1 Data Sets

In this analysis, Υ are measured via $\Upsilon \rightarrow e^+e^-$ decay channel with the data sets taken in 2015 p+p collisions at $\sqrt{s} = 200$ GeV and 2015 p+Au collisions at $\sqrt{s_{NN}} = 200$ GeV. These data are triggered by BHT2*BBCMB trigger, which triggers on high transverse energy (E_T) particle events by requiring at least one of the BEMC towers is fired (the deposited energy in BEMC tower should pass the trigger threshold ~ 4.3 GeV), at the mean time there should be at least one pair of coincidental hits between BBC East detector and BBC West detector. The total number of recorded events from p+p and p+Au collisions are listed in Table II.

Data Name	Luminosity [pb^{-1}]	Number of events [M]
2015pp	120.539	234.737
2015pAu	407.010	181.376

TABLE II: The total recorded luminosity and number of events triggered by BHT2*BBCMB in 2015 p+p and p+Au collisions.

3.1.2 Event Selection

For the event selection, a valid vertex for each event is required. The definition of a valid vertex is a reconstructed primary vertex within 80 cm of the TPC center along the beam direction (z direction), and this primary vertex should be the one with the highest probability from a in-bunch collision. This requirement is realized by applying a cut of “ $|V_z| < 80$ cm and $\text{ranking} > 0$ ” on the reconstructed primary vertex of each event, where V_z is the position of reconstructed primary vertex along the z - direction while $\text{ranking} > 0$ corresponds to the index of vertex with highest probability. The number of events corresponding to each requirement are listed in Table XVIII.

Data Name	Cuts	Number of events [M]
2015pp	$ V_z < 200$ cm	221.18
2015pp	$ V_z < 80$ cm	188.53
2015pp	$ V_z < 80$ cm & $\text{ranking} > 0$	165.56
2015pAu	$ V_z < 200$ cm	165.80
2015pAu	$ V_z < 80$ cm	131.75
2015pAu	$ V_z < 80$ cm & $\text{ranking} > 0$	125.19

TABLE III: Number of BHT2*BBCMB events corresponding to different requirements in 2015 p+p and p+Au collisions.

3.1.3 Track Selection

As Υ decays nearly at the collision point due to its very short lifetime, thus only primary tracks are used for the Υ reconstruction. In order to select high quality primary tracks, the following basic cuts are applied:

- $p_T > 0.2$ GeV/c, a cut on the transverse momentum of track, to ensure that the track can fly into the TPC volume under the STAR magnetic field.
- $dca < 1.5$ cm, a cut on the Distance of Closest Approach (Dca), to select those tracks close to primary tracks and reduce the secondary tracks.
- $|\eta| < 1$, a cut on the pseudorapidity, to ensure tracks stay within the TPC or EMC detector effective acceptance.
- $nHitsFit \geq 25$, a cut on the number of hit points used to fit this track (the maximum given by the number of TPC readout pads, 45), to ensure the curve of a track is fitted by enough hit points so that a precise momentum information.
- $R \leq 0.52$, a cut on the ratio “R” of hit points used for fitting over the maximum possible points along this track, to reduce the possibility of selecting duplicated short tracks.
- $nHitsDedx \geq 15$, a cut on the number of points used for evaluating the energy loss $\langle dE/dx \rangle$ of track, to ensure a precise dE/dx information.

3.1.4 Electron Track Selection

As Υ are so massive ($m_{\Upsilon(1S)} = 9.46$ GeV/c²) that their decayed electrons are mainly high momentum electrons which can reach the BEMC detector (a threshold of $E_T \sim 1$ GeV).

Therefore, all electrons used for Υ reconstruction in this analysis are required to be able to match to BEMC towers. The electron identification (EID) is done by making use of information from both TPC and BEMC detectors. The electron identification related cuts are as follows:

- $p_T > 1.0 \text{ GeV}/c$, a cut on the transverse momentum, to ensure the electron could reach BEMC detector.
- $0.7 < E/p < 2.0$, a cut on the ratio of energy deposited in BEMC tower over the momentum extracted based the curve of track and STAR magnetic field. As electrons deposit most of their energy in the BEMC towers, this ratio are expected to be close to 1, while on the other side hadrons deposit less energy in BEMC towers, thus this cut could help to reject hadrons.
- $|z\text{Dist}| < 10 \text{ cm}$, $|\text{phiDist}| < 1 \text{ cm}$, a cut on the difference between the BEMC recorded hit position and the extrapolated BEMC hit position based on TPC tracks. This is to ensure tracks are matched to BEMC towers.
- $-1.5 < n\sigma_e < 2.5$, $n\sigma_e = \frac{1}{\sigma(\langle dE/dx \rangle)} \log \frac{\langle dE/dx \rangle^{\text{measured}}}{\langle dE/dx \rangle^{\text{expected}}}$. $\langle dE/dx \rangle^{\text{measured}}$ is the measured average energy loss of a track, $\langle dE/dx \rangle^{\text{expected}}$ is the expected average energy loss while assuming this track is an electron track, $\sigma(\langle dE/dx \rangle)$ is the energy loss resolution for electrons which depends on the path length, hit positions and momentum of a track. As different particle has different interaction property with the TPC gas, which results in different energy loss characteristic. Therefore the energy loss information measured by TPC could be used to perform the particle identification. However when momentum is high ($\geq 3 \text{ GeV}/c$), the bands of energy loss $\langle dE/dx \rangle$ as a function

of momentum of hadrons merge into what of electrons, making the discrimination of electrons and hadrons very difficult. Instead of using dE/dx directly, the new variable of $n\sigma_e$, centering around zero with a width of unity for pure electrons, could provide a better power to separate electrons from hadrons, is thus more commonly used.

- $DsmAdc > 18$ & $Adc0 \geq 300$ & $p_T > 3.5$ GeV/c, these cuts are only applied on the triggered electrons, where the trigger threshold values of $DsmAdc$, $Adc0$ and p_T corresponding to BHT2*BBCMB trigger is 18, 300 and ~ 3.5 GeV/c. $DsmAdc$ (or $Adc0$) is a variable converted from the deposited energy in the BEMC tower, which is used for the online trigger decision.

3.1.5 Make Electron Pairs

After the selection of electron candidates, the Υ candidates can be reconstructed based these electron candidates. The electrons from Υ decays are always e^+e^- pairs, thus all the unlike-sign electron candidates within one event are made into pairs, called the unlike-sign pairs. However, these unlike-sign pairs not only includes the Υ decayed electron pairs but also background contributions from semileptonic decays of correlated $B-\bar{B}$ meson decays, Drell – Yan process and random combinations.

The invariant mass of each pair can be calculated by:

$$m_{ee} = \sqrt{(E_1 + E_2)^2 - \|\vec{p}_1 + \vec{p}_2\|^2} \quad (3.1)$$

where, for each electron candidate: the \vec{p} is the momentum vector, which can be measured by TPC, $E = \sqrt{m_e^2 + \vec{p}^2}$ is the total kinematic energy; $m_e = 0.511 \text{ MeV}/c^2$ is the mass of electron.

- UnlikeSign Pairs = $\Upsilon(1S) + \Upsilon(2S) + \Upsilon(3S) + B\bar{B} + \text{Drell-Yan} + \text{RandomCombination}$

The contribution from random combination can be estimated from the like-sign pairs (e^+e^+ or e^-e^-), and the physics background from semileptonic decays of correlated $B\bar{B}$ meson decays and Drell-Yan process can be studied from the simulations. The yield of Upsilon signals can be obtained from the fitting of the subtraction of UnlikeSign and LikeSign electron pairs, and the details about the fitting method will be introduced in the later section.

Since Υ has very large mass, their decayed electrons should be all high momentum electrons. As the mass of group Υ state, $m_{\Upsilon(1S)} = 9.46 \text{ GeV}/c^2$, so the high momentum daughter electron should have a momentum larger than $4.5 \text{ GeV}/c$, and to further reduce the background level, a momentum cut on the lower momentum daughter electron is set to be $3.5 \text{ GeV}/c$. Since each event is triggered by the BHT2*BBCMB trigger, an additional requirement that there should be at least one triggered electron for each pair. The above two requirements are applied on both unlike-sign and like-sign pairs.

3.2 Efficiency Studies

3.2.1 Single Electron Reconstruction Efficiency

The single electron reconstruction efficiency is studied mainly based on the STAR official embedding simulations [70]. For the STAR official embedding simulation, the Monte Carlo

(MC) Υ decayed electrons are feed into the GEANT3 [71] detector simulator with the full geometry of STAR detectors, where the interactions between particles and detector materials are simulated and generate the Monte Carlo response signals of detectors. These MC detector responses are embedded into the real BHT2*BBCMB triggered raw data which are randomly sampled over the entire available data samples. After the mixing of MC responses of detectors together with those from real data, the data reconstruction with exactly same algorithms as for the real data reconstruction are performed with these mixed responses or signals. The single electron reconstruction efficiency can be calculated by looking at the ratio of the number of successfully reconstructed electron tracks over the total number of input MC electron tracks.

The STAR official embedding simulations cannot well reproduce the $n\sigma_e$ information of particles, thus the $n\sigma_e$ cut efficiency of electrons is estimated from the real data. In real data, a pure electron sample is obtained from the photon conversion electrons ($\gamma \rightarrow e^+e^-$), which are usually called photonic electrons. In this analysis, the photonic electrons are selected by the following selection criterion:

- the invariant mass of electron pairs: $m_{ee} < 0.24 \text{ GeV}/c^2$
- the Dca between two electron candidate tracks: $Dca_{ee} < 1.0 \text{ cm}$
- tight cuts on one electron candidate: $DsmAdc > 18$, $Adc0 > 300$, $|\eta| < 1$, $p_T > 0.2$, $nHitsFit \geq 20$, $nHitsDedx \geq 15$, $R > 0.52$, $-1 < n\sigma_e < 2.0$, $Dca < 1.5\text{cm}$, $0.6 < E/p < 3.0$, $|zDist| < 3$, $|\phi Dist| < 0.15$. This electron candidate is named as primary electron.
- cuts on the other electron candidate: $|\eta| < 1$, $p_T > 0.2$, $nHitsFit \geq 20$, $nHitsDedx \geq 15$, $R > 0.52$. This electron candidate is named as partner electron.

With the above selection, a clean electron samples can be obtained. The distribution of $n\sigma_e$ of electrons is studied by the partner electrons as there is no $n\sigma_e$ cut on them. The left panel of Figure 38 shows an example of the $n\sigma_e$ distribution of the partner electrons within a small p_T window of $4.0 < p_T < 4.5$ GeV/c, the mean and width (sigma) of $n\sigma_e$ can be extracted by fitting this $n\sigma_e$ distribution with a Gaussian function. The mean and sigma as a function of p_T can be obtained as shown in the right panel of Figure 38, as they are nearly flat with p_T , their values can be fitted by constant-value lines. The fitted constant mean and sigma of $n\sigma_e$ can be set to a Gaussian function and then use this Gaussian function to perform the random sampling on the electron tracks for the estimation of the $n\sigma_e$ cut efficiency on electrons.

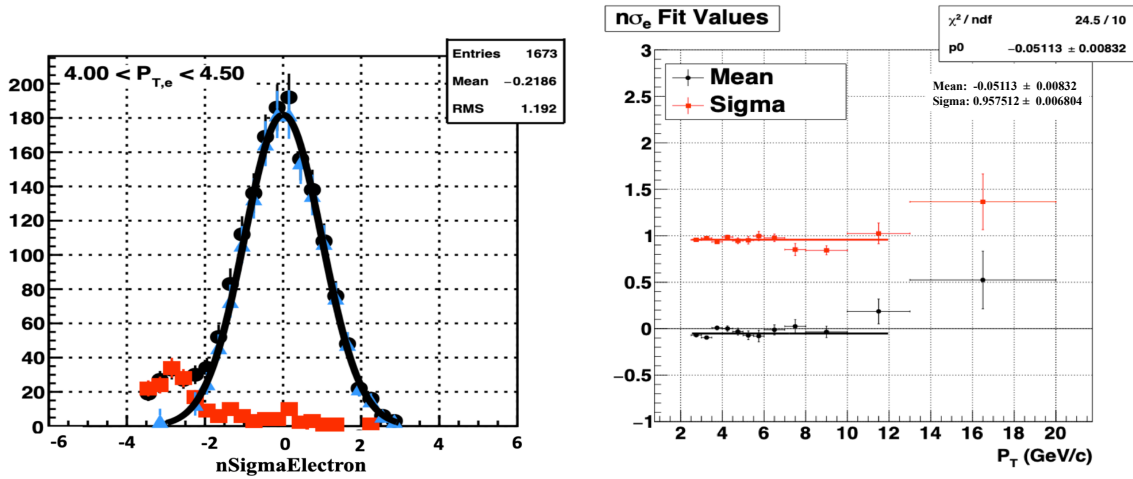


Figure 38: The left panel shows an example of $n\sigma_e$ distribution of photonic electrons within a transverse momentum window: $4.0 < p_T < 4.5$ GeV/c. The black points corresponds to the unlike-sign pairs, the red points corresponds to the like-sign pairs, the purple points are obtained by subtracting the like-sign distribution from the unlike-sign distribution. The right panel shows the fitted mean and width (sigma) of $n\sigma_e$ distributions as a function of p_T .

The single electron efficiency in 2015 p+p and p+Au are calculated in different pseudorapidity bins, Figure 39 shows an example of single electron reconstruction efficiency as a function of p_T within a pseudorapidity window of $0.2 < \eta < 0.4$ in 2015 pp and pAu. Where, the efficiencies corresponding to TPC, EMC and the BHT2 trigger are defined as follows:

- “TPC” is defined by cuts of “ $p_T > 0.2 \text{ GeV}/c$ & $n\text{HitsFits} \geq 25$ & $n\text{HitsDedx} \geq 15$ & $R \geq 0.52$ & $0 < \text{Dca} < 1.5 \text{ cm}$ & $-1.5 < n\sigma_e < 2.0$ ”

The efficiency of TPC: $\epsilon_{\text{TPC}} = \frac{\text{TPC}}{\text{MC}}$

- “EMC” is defined by cuts of “ $p_T > 1.5 \text{ GeV}/c$ & $e > 0.1 \text{ GeV}$ & $|z\text{Dist}| < 10 \text{ cm}$ & $|\text{phiDist}| < 1 \text{ cm}$ ” & $0.7 < e/p < 2.0$ ”

The efficiency of EMC: $\epsilon_{\text{EMC}} = \frac{\text{TPC\&EMC}}{\text{TPC}}$

- “Trg BHT2”:

BHT2 is defined by cuts of: “ $p_T > 3.5 \text{ GeV}/c$ & $\text{DsmAdc} > 18$ & $\text{Adc0} \geq 300$ ”

The efficiency of Trg BHT2: $\epsilon_{\text{BHT2}} = \frac{\text{TRGBHT2\&EMC\&TPC}}{\text{EMC\&TPC}}$

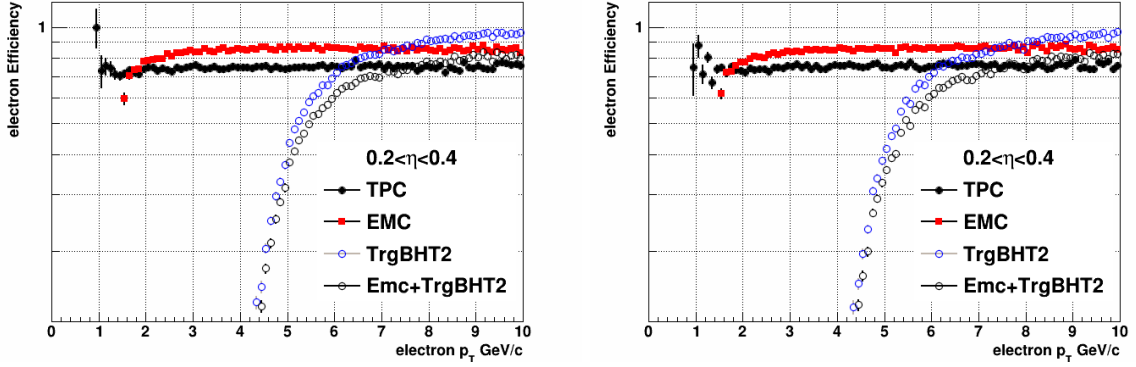


Figure 39: An example of single electron reconstruction efficiency as a function of p_T in Run15pp (left) and Run15pAu (right) within a pseudorapidity window of $0.2 < \eta < 0.4$.

3.2.2 Momentum Resolution

Due to the complexity of detector response simulations in TPC, it is hard for the embedding simulations to reproduce the momentum resolution precisely as in the real data reconstruction. However, this can be corrected by data-driven method following procedures:

1. The TPC momentum resolution as function of p_T for electron tracks can be studied from Embedding data. For each given p_T value (a small p_T bin), the σ of $\frac{p_T^{RC} - p_T^{MC}}{p_T^{MC}}$ can be obtained

by the fitting of its distribution with a double Crystall-Ball function. The double Crystall-Ball function is defined as follow equations:

$$P(p_T^{\text{RC}}, p_T^{\text{MC}}) \propto \begin{cases} A * (B - R)^{-n_1}, & \text{if } R \leq -\alpha_1 \\ e^{-\frac{R^2}{2}}, & \text{if } -\alpha_1 \leq R \leq \alpha_2 \\ C * (D + R)^{-n_2}, & \text{if } R \geq \alpha_2 \end{cases} \quad (3.2)$$

where: $A = (\frac{n_1}{|\alpha_1|})^{n_1} * e^{-\frac{-\alpha_1^2}{2}}$, $B = \frac{n_1}{|\alpha_1|} - |\alpha_1|$, $C = (\frac{n_2}{|\alpha_2|})^{n_2} * e^{-\frac{-\alpha_2^2}{2}}$, $D = \frac{n_2}{|\alpha_2|} - |\alpha_2|$,
 $R = (\frac{p_T^{\text{RC}} - p_T^{\text{MC}}}{p_T^{\text{MC}}} - \mu) / \frac{\sigma_{p_T}}{p_T}$

2. After fittings for each p_T bin, the electron p_T resolution ($\frac{\sigma_{p_T}}{p_T}$) as a function of p_T can be obtained, and this distribution can be well described by the following function:

$$f(p_T) = \sqrt{a^2(p_T)^2 + b^2} \quad (3.3)$$

The initial values of parameter a and b from the fitting is shown in the top left panel of Figure 63.

3. Fill the $\frac{p_T^{\text{RC}} - p_T^{\text{MC}}}{p_T^{\text{MC}}} \frac{0.01}{(\sigma_{p_T}/p_T)}$ vs p_T distribution, then fit this distribution by the double Crystall-ball function, obtain the all parameters from this fit as shown in the top right panel of Figure 63. The p_T of electrons can be smeared based on the function $f(p_T)$ and this Crystall-ball function.

4. The best the momentum resolution parameter ‘‘a’’ value can be obtained by tuning the a value to make the smeared J/ψ best matched to the J/ψ signals reconstructed in the real data

as shown in the bottom panel of Figure 63. For a fair comparison between the smeared J/ψ and J/ψ in real data, the p_T and y of smeared J/ψ were weighted to be same as the J/ψ in real data.

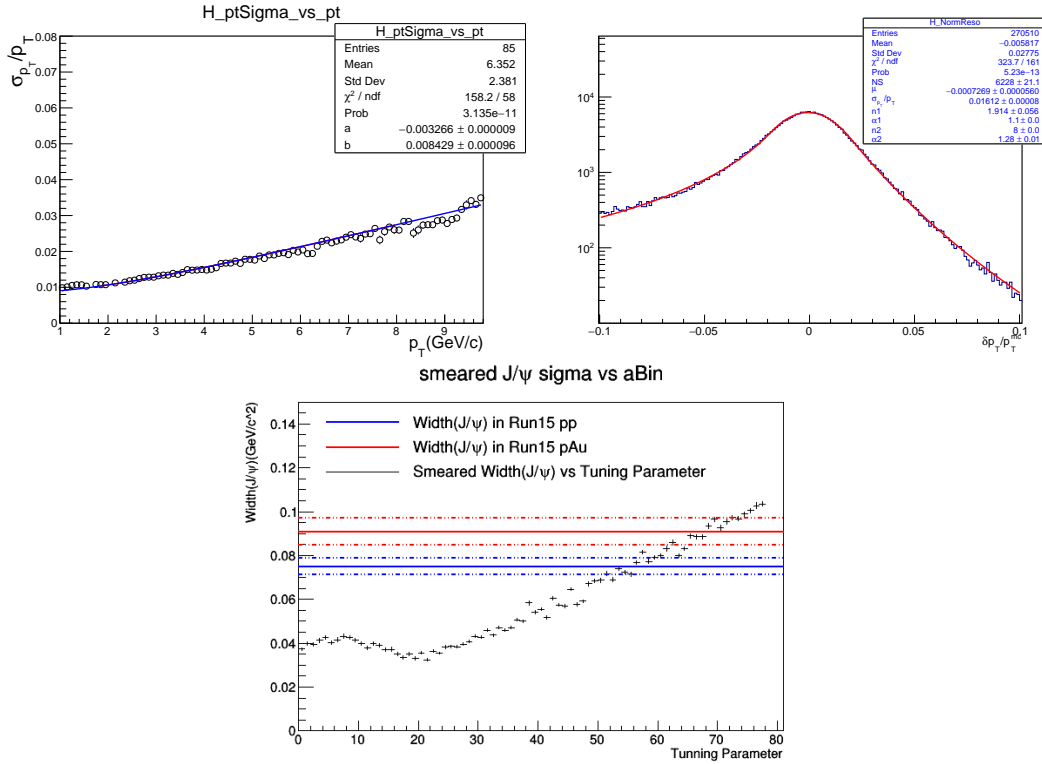
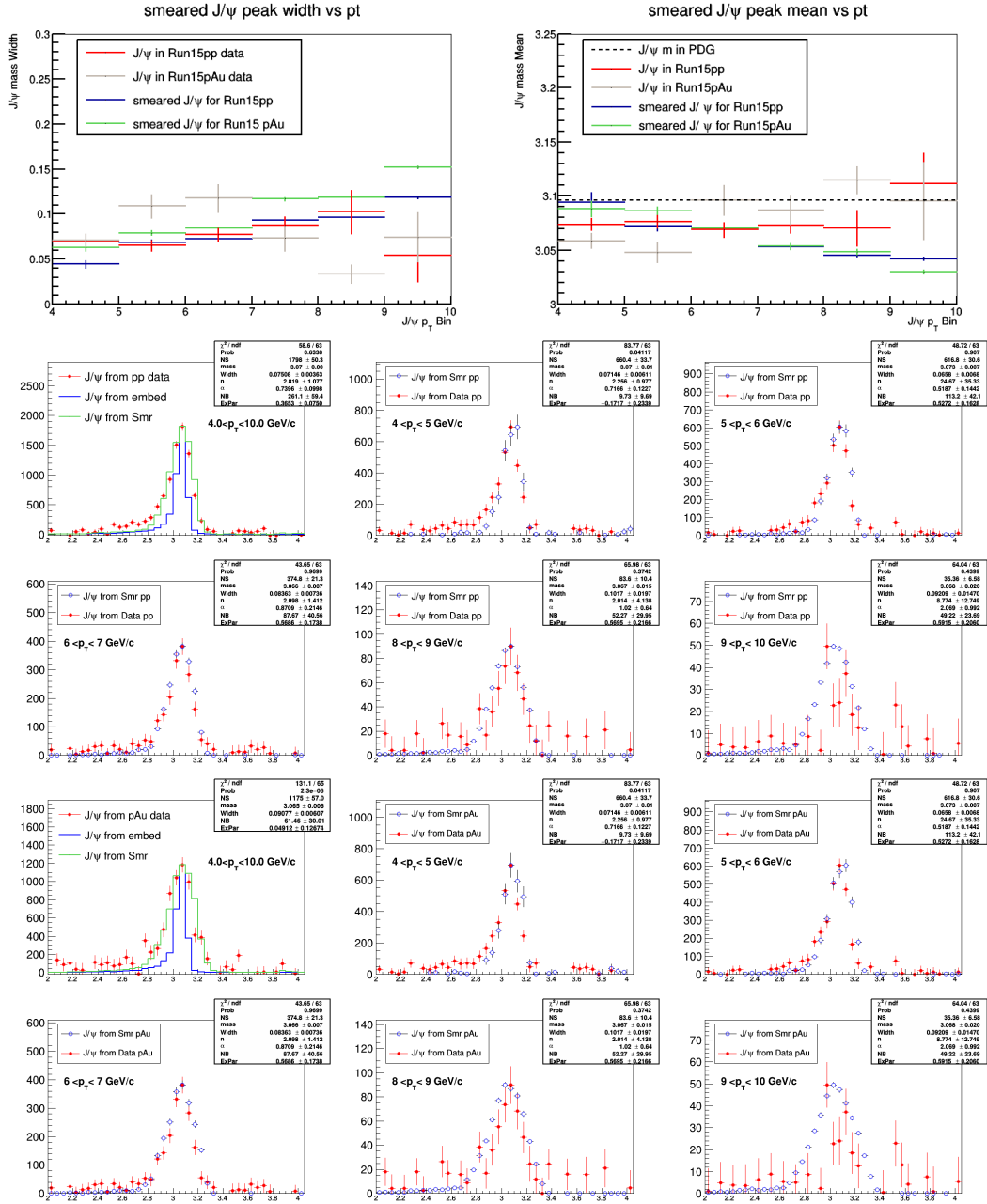


Figure 40: The top left panel shows the momentum resolution $\sigma(\frac{\delta p_T}{p_T})$ as function of p_T , fitted with a function of $f(p_T) = \sqrt{a^2(p_T)^2 + b^2}$. The top right panel shows the normalized $\delta p_T/p_T$ fitted by Double Crystal Ball function. The bottom panel shows the tuning of parameter “a” to best match the J/ψ width in Run15 pp and Run15 pAu BHT2 triggered data (The solid line is the fitted J/ψ width and the dotted lines shows the uncertainty of the fitted J/ψ width. The J/ψ p_T range is 4-10 GeV/c).

The mean and width of J/ψ from smeared signals are compared to that from real data as shown in the top two panels of Figure 64, the p_T range are selected to be 4 GeV/c to 10 GeV/c since the BHT2 trigger has a threshold cut on the triggered particle energy ~ 4.2 GeV. The following panels in Figure 64 shows the overlay of J/ψ signals from real data and from smearing for both Run15 pp and Run15 pAu in each p_T bin. Note that the blue lines in the $4 < p_T < 10$ GeV/c plots are corresponding to the original momentum resolution directly from the embedding samples of Run15 pp and Run15 pAu, respectively.

Figure 41: Comparison of smeared J/ψ to real data of 2015 pp and 2015 pAu

3.2.3 Upsilon Reconstruction Efficiency

The Υ reconstruction efficiency is obtained by enfolding all single electron reconstruction efficiency to the Υ decayed electrons and then calculate the fraction of successfully reconstructed Υ candidates from those electron pairs while considering the kinematic cuts (the high momentum electron: $p_e^{\text{high}} > 4.5$ GeV/c and the low momentum electron: $p_e^{\text{low}} > 3.5$ GeV/c) and detector acceptance ($|y_\Upsilon| < 1$ and $|\eta_e| < 1$). The single electron efficiency is as function of p_T for each small η bin ($\delta\eta = 0.2$) as shown in Figure 39. Υ are decayed by the EvtGen package (<https://evtgen.hepforge.org/>). The rapidity of Υ is weighted by a Gaussian ($\sigma = 1.15$), and the p_T of Υ is weighted by a Boltzmann-shape: $f(p_T) = \frac{p_T}{\exp(p_T/T)+1}$ where $T=1.127$. The summary of Υ detection efficiency in different rapidity bins and different p_T bins are listed in Table IV and Table V respectively.

Run15pp				
States	$ y < 1$	$ y < 0.5$	$0.5 < y < 1$	$-1.0 < y < -0.5$
$\Upsilon(1S)$	0.0579 ± 0.0004	0.0765 ± 0.0007	0.0345 ± 0.0006	0.0385 ± 0.0007
$\Upsilon(2S)$	0.0738 ± 0.0005	0.0988 ± 0.0008	0.0445 ± 0.0008	0.0456 ± 0.0008
$\Upsilon(3S)$	0.0828 ± 0.0009	0.1125 ± 0.0008	0.0474 ± 0.0008	0.0499 ± 0.0008
Run15pAu				
States	$ y < 1$	$ y < 0.5$	$0.5 < y < 1$	$-1.0 < y < -0.5$
$\Upsilon(1S)$	0.0557 ± 0.0004	0.0732 ± 0.0007	0.0343 ± 0.0006	0.0367 ± 0.0007
$\Upsilon(2S)$	0.0701 ± 0.0005	0.0945 ± 0.0008	0.0415 ± 0.0007	0.0428 ± 0.0007
$\Upsilon(3S)$	0.0780 ± 0.0005	0.1064 ± 0.0008	0.0441 ± 0.0008	0.0469 ± 0.0008

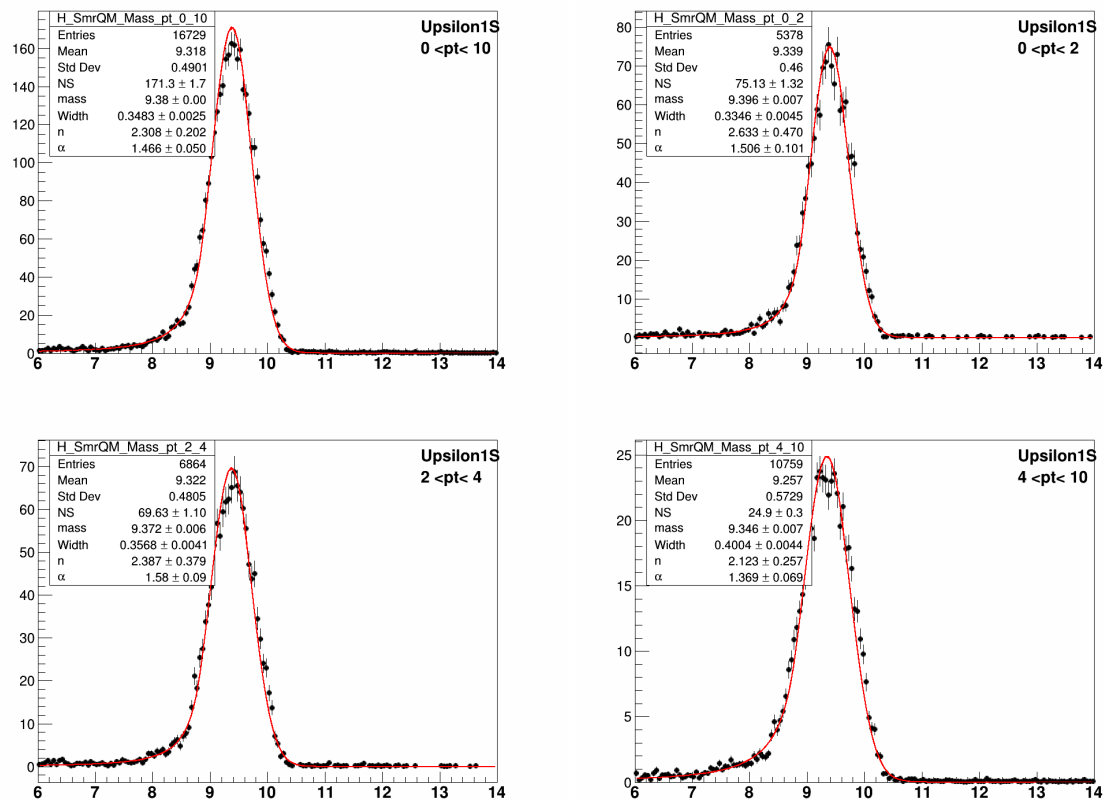
TABLE IV: Υ detection efficiency in different rapidity ranges with p_T integrated over $0 < p_T < 10$ GeV/c for Run15 pp and pAu.

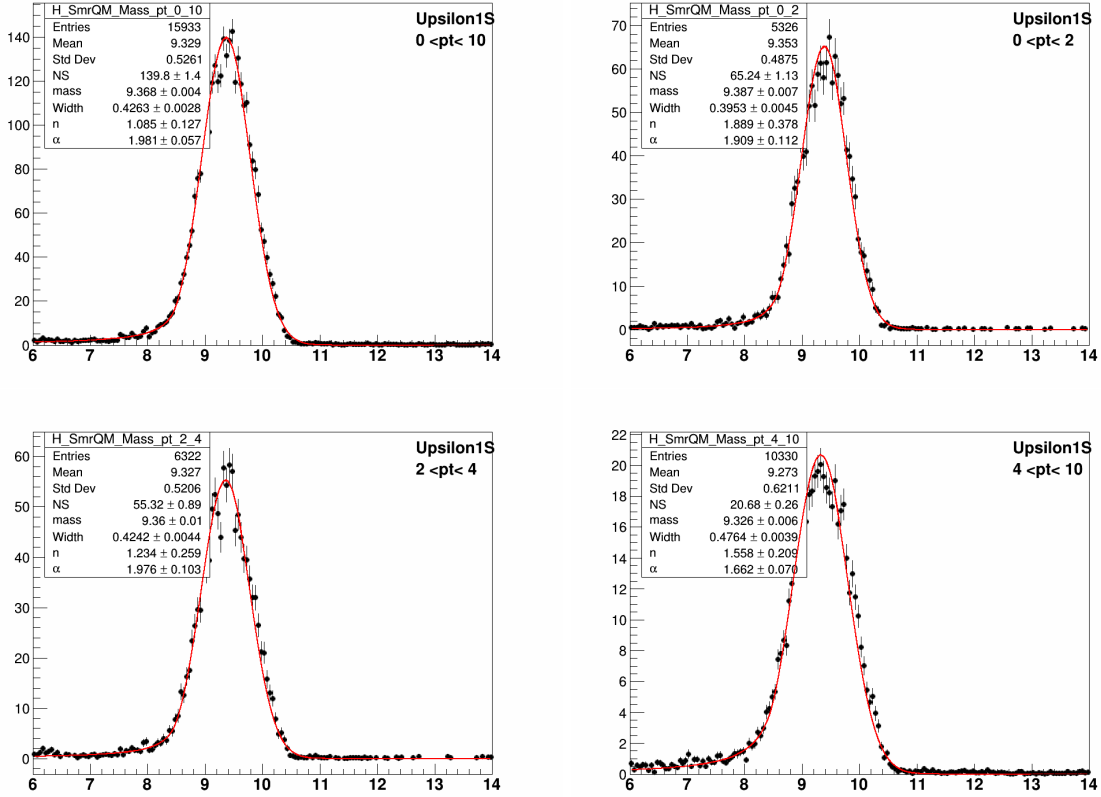
Run15pp $ \mathbf{y} < 1.0$			
States	$0 < p_T < 2$	$2 < p_T < 4$	$4 < p_T < 10$
$\Upsilon(1S)$	0.0535 ± 0.0007	0.0624 ± 0.0007	0.0612 ± 0.0006
$\Upsilon(2S)$	0.0710 ± 0.0008	0.0772 ± 0.0008	0.0741 ± 0.0007
$\Upsilon(3S)$	0.0798 ± 0.0008	0.0871 ± 0.0009	0.0821 ± 0.0007
Run15pp $ \mathbf{y} < 0.5$			
States	$0 < p_T < 2$	$2 < p_T < 4$	$4 < p_T < 10$
$\Upsilon(1S)$	0.0708 ± 0.0011	0.0826 ± 0.0012	0.0820 ± 0.0010
$\Upsilon(2S)$	0.0941 ± 0.0012	0.1041 ± 0.0013	0.1002 ± 0.0011
$\Upsilon(3S)$	0.1070 ± 0.0014	0.1195 ± 0.0014	0.1121 ± 0.0012
Run15pAu $ \mathbf{y} < 1.0$			
States	$0 < p_T < 2$	$2 < p_T < 4$	$4 < p_T < 10$
$\Upsilon(1S)$	0.0529 ± 0.0007	0.0581 ± 0.0007	0.0589 ± 0.0006
$\Upsilon(2S)$	0.0675 ± 0.0008	0.0736 ± 0.0008	0.0706 ± 0.0006
$\Upsilon(3S)$	0.0750 ± 0.0008	0.0817 ± 0.0009	0.0784 ± 0.0007
Run15pAu $ \mathbf{y} < 0.5$			
$\Upsilon(1S)$	0.0693 ± 0.0011	0.0762 ± 0.0011	0.0783 ± 0.0009
$\Upsilon(2S)$	0.0903 ± 0.0013	0.0999 ± 0.0013	0.0953 ± 0.0011
$\Upsilon(3S)$	0.1015 ± 0.0013	0.1121 ± 0.0014	0.1076 ± 0.0012

TABLE V: Υ detection efficiency in different p_T ranges with rapidity integrated over $|\mathbf{y}| < 1.0$ and $|\mathbf{y}| < 0.5$ for Run15 pp and Run15 pAu.

3.2.4 Upsilon Templates from Smearing

The Υ templates shapes are can obtained by smearing the MC with the momentum resolution parameters tuned to match the smeared J/ψ to real data. The smeared Υ templates for Run15 pp and Run15 pAu are shown in Figure 42 and Figure 43.

Figure 42: Υ templates for Run15 pp

Figure 43: Υ templates for Run15 pAu

3.2.5 Physics Background Shapes of $B\bar{B}$ and Drell-Yan from Simulation

The background from $B\bar{B}$ decays and Drell-Yan process are studied by the Pythia6 simulation with all the efficiency of single electron embedded within STAR detector acceptance. The Pythia settings are from PHENIX tuning which could well describe the measurements of $B\bar{B}$ and Drell-Yan in p+p collisions at $\sqrt{s} = 200$ GeV [74]. Figure 66 show the invariant mass dis-

tributions of unlike-sign pairs from $B\bar{B}$ and Drell-Yan, and these shapes are used in the fitting of Υ signals for Run15 pp and pAu.

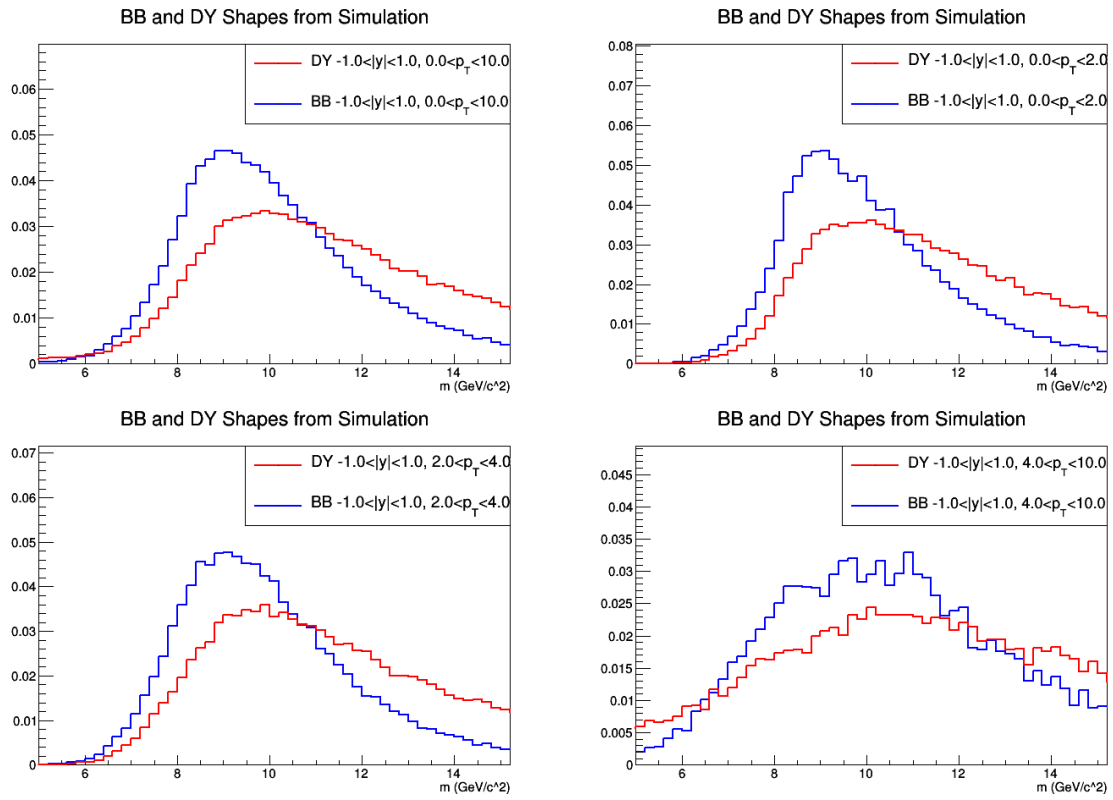


Figure 44: Background shapes of $B\bar{B}$ and Drell-Yan from Simulation

3.3 Upsilon Yields Extraction

The extraction of Υ signal yields is performed based a powerful package: RooFit, which provides a toolkit for modeling the expected distribution of events in a physics analysis.

The subtraction of unlike-sign and like-sign electron pairs are fitted by a function composed of $\Upsilon(1S)$, $\Upsilon(2S)$, $\Upsilon(3S)$ shapes, BB shape and DY shape:

$$f_{\text{total}} = \text{Yield}(1S) * \epsilon(1S) * \text{pdf}(1S) + \text{Yield}(2S) * \epsilon(2S) * \text{pdf}(2S) + \text{Yield}(3S) * \epsilon(3S) * \text{pdf}(3S) \\ + \text{Yield}(BB) * \epsilon(BB) * \text{pdf}(BB) + \text{Yield}(DY) * \epsilon(DY) * \text{pdf}(DY) \quad (3.4)$$

Where:

- “Yield” is the yield corrected by detection efficiency
- “ ϵ ” is the detection efficiency
- “pdf” is the particle probability distribution function

Because of the resolution in our data does not allow a clear separation of individual Υ state from each other, the three Υ pdfs are combined into one single pdf in our fitting. The combined pdf for all Υ states $\Upsilon(1S2S3S)$ can be constructed from each Υ pdf while weighted by their detection efficiency and the world wide experimental average ratios of $\Upsilon(1S) : \Upsilon(2S) : \Upsilon(3S) = 1 : 0.275 : 0.128$ from PDG.

The combined Upsilon pdf can be expressed as:

$$\begin{aligned}
\Pi &= \text{Yield}(1S) * \epsilon(1S) * \text{pdf}(1S) + \text{Yield}(2S) * \epsilon(2S) * \text{pdf}(2S) + \text{Yield}(3S) * \epsilon(3S) * \text{pdf}(3S) \\
&= \frac{\text{Yield}(1S2S3S) * \epsilon(1S2S3S)}{\text{Yield}(1S2S3S) * \epsilon(1S2S3S)} * \Pi \\
&= \frac{\text{Yield}(1S2S3S) * \epsilon(1S2S3S)}{\text{Yield}(1S2S3S) * \epsilon(1S2S3S)} * \{\text{Yield}(\Upsilon(1S)) * \epsilon(\Upsilon(1S)) * \text{pdf}(\Upsilon(1S)) \\
&\quad + \text{Yield}(\Upsilon(2S)) * \epsilon(\Upsilon(2S)) * \text{pdf}(\Upsilon(2S)) + \text{Yield}(\Upsilon(3S)) * \epsilon(\Upsilon(3S)) * \text{pdf}(\Upsilon(3S))\} \\
&= \text{Yield}(1S2S3S) * \epsilon(1S2S3S) * \left\{ \frac{\text{Yield}(1S)}{\text{Yield}(1S2S3S)} * \frac{\epsilon(1S)}{\epsilon(1S2S3S)} * \text{pdf}(1S) \right. \\
&\quad \left. + \frac{\text{Yield}(2S)}{\text{Yield}(1S2S3S)} * \frac{\epsilon(2S)}{\epsilon(1S2S3S)} * \text{pdf}(2S) + \frac{\text{Yield}(3S)}{\text{Yield}(1S2S3S)} * \frac{\epsilon(3S)}{\epsilon(1S2S3S)} * \text{pdf}(3S) \right\}
\end{aligned} \tag{3.5}$$

Where:

- $\text{Yield}(1S2S3S) = \text{Yield}(1S) + \text{Yield}(2S) + \text{Yield}(3S)$
- $\epsilon(1S2S3S) = \frac{\text{Yield}(1S)}{\text{Yield}(1S2S3S)} * \epsilon(1S) + \frac{\text{Yield}(2S)}{\text{Yield}(1S2S3S)} * \epsilon(2S) + \frac{\text{Yield}(3S)}{\text{Yield}(1S2S3S)} * \epsilon(3S)$
- $\frac{\text{Yield}(1S)}{\text{Yield}(1S2S3S)} = 0.7042, \frac{\text{Yield}(2S)}{\text{Yield}(1S2S3S)} = 0.2042, \frac{\text{Yield}(3S)}{\text{Yield}(1S2S3S)} = 0.0915$

The fitting function can be transformed to be as follows:

$$\begin{aligned}
f_{\text{total}} &= \text{Yield}(1S2S3S) * \epsilon(1S2S3S) * \{c_1 * \text{pdf}(1S) + c_2 * \text{pdf}(2S) + c_3 * \text{pdf}(3S)\} \\
&\quad + \text{Yield}(BB) * \epsilon(BB) * \text{pdf}(BB) + \text{Yield}(DY) * \epsilon(DY) * \text{pdf}(DY)
\end{aligned} \tag{3.6}$$

Where:

- $\text{Yield}(1S2S3S)$ is the efficiency corrected yield of $\Upsilon(1S2S3S)$

- $\epsilon(1S2S3S)$ is the efficiency of $\Upsilon(1S2S3S)$
- c_i is the constant of $\frac{Yield(iS)}{Yield(1S2S3S)} * \frac{\epsilon(iS)}{\epsilon(1S2S3S)}$, $i = 1, 2, 3$

In the fitting, pdf(1S), pdf(2S), pdf(3S), BB, DY shapes are obtained from the simulation, $Yield(1S2S3S) * \epsilon(1S2S3S)$, $Yield(BB) * \epsilon(BB)$ and $Yield(DY) * \epsilon(DY)$ are free parameters (as raw yields) which will be obtained by fitting to the invariant mass spectrum (UnlikeSign - LikeSign) in real data.

3.3.1 Upsilon Signals in Run15 pp

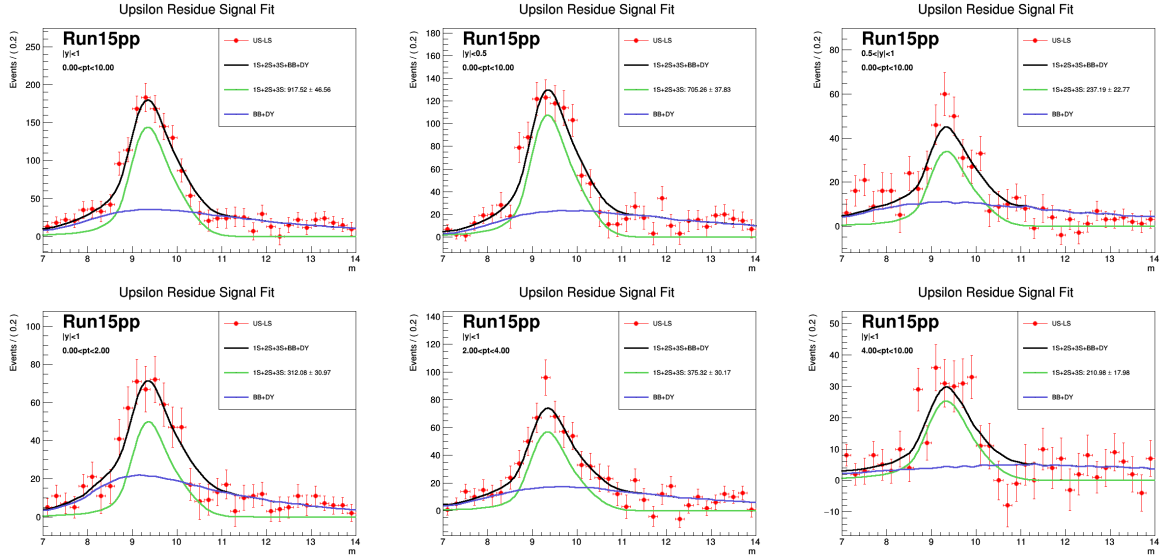


Figure 45: Upsilon signals in Run15 pp. The top three panels are Upsilon signals in different rapidity bins: $|y| < 1$, $|y| < 0.5$, $0.5 < |y| < 1$ with p_T integrated over $0 < p_T < 10$ GeV/c; The bottom three panels are Upsilon signals in different p_T bins: $0 < p_T < 2$ GeV/c, $2 < p_T < 4$ GeV/c, $4 < p_T < 10$ GeV/c with rapidity integrated over $|y| < 1$.

3.3.2 Upsilon Signals in Run15 pAu

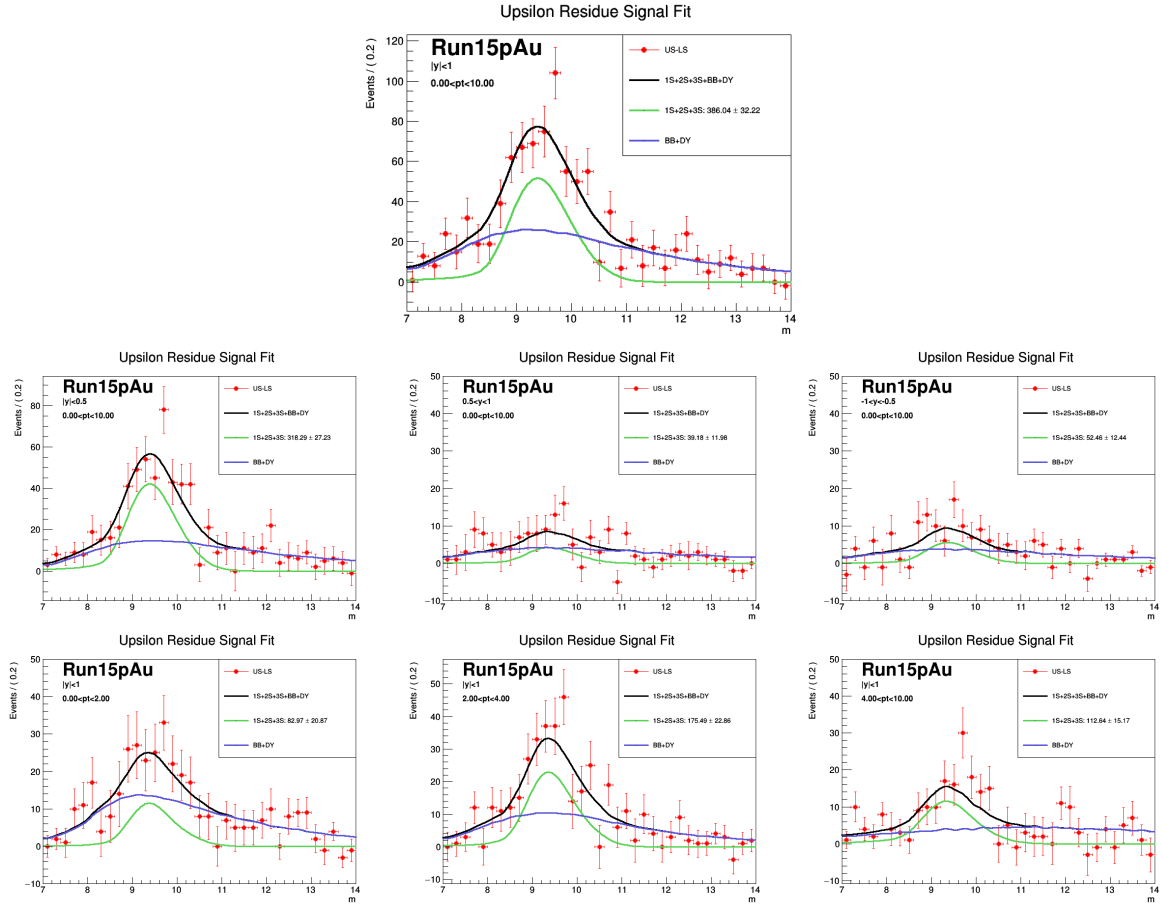


Figure 46: Upsilon signals in Run15 pAu. The top panel is the inclusive Upsilon signal. The middle three panels are Upsilon signals in different rapidity bins: $|y| < 0.5$, $0.5 < y < 1$, $-1 < y < -0.5$ with p_T integrated over $0 < p_T < 10$ GeV/c; The bottom three panels are Upsilon signals in different p_T bins: $0 < p_T < 2$ GeV/c, $2 < p_T < 4$ GeV/c, $4 < p_T < 10$ GeV/c with rapidity integrated over $|y| < 1$.

3.4 Number of Equivalent MB Events and Trigger Bias Calculation

In Run15 pp and pAu, Υ is studied with the BHT2*BBCMB triggered events. In this analysis, the number of equivalent MB events and the trigger bias are calculated for both J/ Ψ and Υ . The cross section of J/ Ψ or Υ can be obtained by equation Equation 3.7.

The J/ ψ or Υ cross section can be obtained by:

$$\sigma_{\text{particle}} = \frac{\sigma_{\text{MB}}}{N_{\text{MB}}^{\text{eqv.}} \epsilon_{\text{MB}}^{\text{goodvtx}}} * \frac{N_{\text{particle}}^{\text{raw}}}{\text{Acc.} \times \epsilon_{\text{particle}}^{\text{Trig}} \epsilon_{\text{particle}}^{\text{trk}} \epsilon_{\text{particle}}^{\text{eID}}} * \frac{\epsilon_{\text{MB}}^{\text{BBC}} \epsilon_{\text{MB}}^{\text{goodvtx}}}{\epsilon_{\text{particle}}^{\text{BBC}} \epsilon_{\text{particle}}^{\text{goodvtx}}} \quad (3.7)$$

Where:

- σ_{MB} is the NSD cross section for p+p collisions and total cross section for p+Au collisions.
- $N_{\text{MB}}^{\text{eqv.}}$ is the number of equivalent BBCMB events corresponding to the analyzed BHT2*BBCMB events.
- $\epsilon_{\text{MB}}^{\text{goodvtx}}$ is the good vertex efficiency in normal MB events.
- $N_{\text{particle}}^{\text{raw}}$ is the number of raw counts of J/ Ψ or Υ from real data.
- Acc. is the acceptance of TPC, EMC and the momentum cuts on electrons.
- $\epsilon_{\text{particle}}^{\text{Trig}}$, $\epsilon_{\text{particle}}^{\text{trk}}$ and $\epsilon_{\text{particle}}^{\text{eID}}$ are the BHT2 trigger efficiency, tracking efficiency and electron identification efficiency, which are obtained from the embedding samples.
- $\epsilon_{\text{MB}}^{\text{BBC}}$ is the BBC efficiency in normal MB events.
- $\epsilon_{\text{particle}}^{\text{BBC}}$ is the BBC efficiency in the particle (J/ Ψ or Υ) events.
- $\epsilon_{\text{particle}}^{\text{goodvtx}}$ is the good vertex efficiency in the particle (J/ Ψ or Υ) events.

- $\frac{\epsilon_{\text{MB}}^{\text{BBC}} \epsilon_{\text{MB}}^{\text{goodvtx}}}{\epsilon_{\text{particle}}^{\text{BBC}} \epsilon_{\text{particle}}^{\text{goodvtx}}}$ is defined as the trigger bias factor in this analysis.

The number of equivalent MB events can be calculated in section 3.4.1. The trigger bias factor and the related efficiency can be obtained by analyze the simulated data of PYTHIA + GEANT + Zero-Bias simulation as discussed in section 3.4.3.1 and section 3.4.3.2.

3.4.1 Number of Equivalent MB Events Based on BBCMB

The number of equivalent MB events can be calculated based on the formula Equation 4.2, here the $N_{\text{MB}}^{\text{eqv.}}(\text{online})$ is the number of equivalent MB events while BBCMB trigger and BHT2*BBCMB trigger are all active. The total number of $N_{\text{MB}}^{\text{eqv.}}(\text{online})$ is calculated by the sum over all runs.

$$N_{\text{MB}}^{\text{eqv.}}(\text{online}) = \sum_{\text{irun}} [N_{\text{BBCMB}}^{\text{recorded}}(|V_z| < 200) \frac{\text{LIVETIME}_{\text{BHT2}} \text{PS}_{\text{BBCMB}}}{\text{LIVETIME}_{\text{BBCMB}} \text{PS}_{\text{BHT2}}}](\text{irun}) \quad (3.8)$$

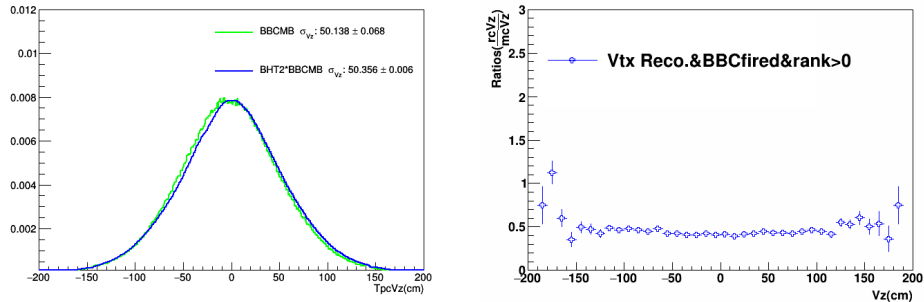


Figure 47: The left panel shows the TPC V_z distributions of BBCMB and BHT2*BBCMB events in Run15 p+p data. The right panel shows the ratio of reconstructed V_z over MC V_z ($\frac{rcV_z}{mcV_z}$) from the PYTHIA8+GEANT+ZeroBias simulation for Run15 pp.

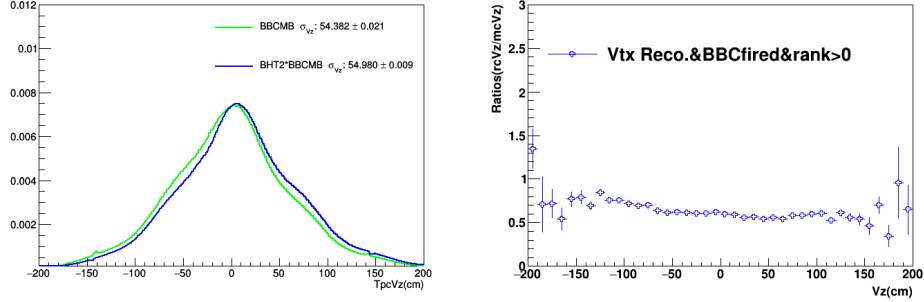


Figure 48: The left panel shows the TPC V_z distributions of BBCMB and BHT2*BBCMB events in Run15 p+Au data. The right panel shows the ratio of reconstructed V_z over MC V_z ($\frac{rcV_z}{mcV_z}$) from the PYTHIA8+GEANT+ZeroBias simulation for Run15 pAu.

In the Figure 47 and Figure 48, the left panel shows the reconstructed TPC V_z distribution of BBCMB and BHT2*BBCMB events with $\text{ranking} > 0$ from the real data. Their fitted width from a Gaussian function (fitting range is $|V_z| < 80\text{cm}$) are listed on the plot. The right panel shows the ratio of reconstructed V_z over MC V_z ($\frac{rcV_z}{mcV_z}$) from the PYTHIA8 + GEANT + ZeroBias simulation. In the simulation, the V_z was initially sampled by the Gaussian function with a width fitted from the real data as shown in the left panel, then weight the MBonly events in simulation to V_z of BBCMB in real data and weight the Particle events in simulation to V_z of BHT2*BBCMB in real data. The results in the right panel is obtained after weighted the MC V_z to the real V_z in left panel. The blue curve in the right panel is thus the efficiency of vertex reconstruction as function of V_z under the condition of “BBC fired and Ranking > 0 ”. Thus, the real V_z distribution can be obtained by correcting the V_z distribution in the real data with such efficiency, the results are shown in Figure 49.

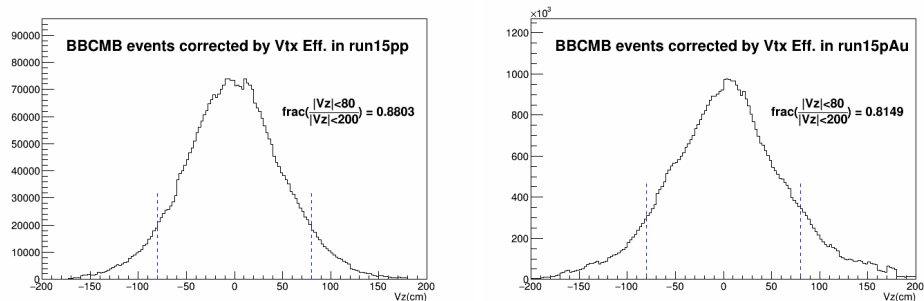


Figure 49: The left panel shows the TPC V_z (ranking > 0) distributions of Run15pp BBCMB events corrected by the efficiency shown in right panel of Figure 47. The right panel shows the TPC V_z (ranking > 0) distributions of Run15pAu BBCMB events corrected by the efficiency shown in right panel of Figure 48.

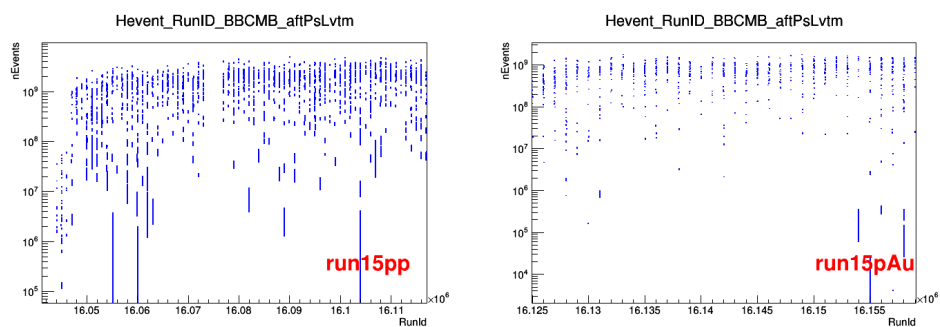


Figure 50: The number of equivalent BBCMB events vs RunId (Run number) corresponding to the BHT2*BBCMB events in Run15 pp and Run15 pAu.

The number of equivalent BBCMB events in each run are shown Figure 50. After sum over all runs and multiply the fraction of $\frac{|Vz| < 80}{|Vz| < 200}$ and multiply the fraction of analyzed BHT2*BBCMB events, the total number of equivalent MB events corresponding to the analyzed BHT2*BBCMB data can be obtained as:

$$N_{\text{MB}}^{\text{eqv.}} = N_{\text{MB}}^{\text{eqv.}}(\text{on-line}) * \frac{N_{\text{BHT2}}(\text{Ana.})}{N_{\text{BHT2}}(\text{on-line})} * \frac{|Vz| < 80}{|Vz| < 200} \quad (3.9)$$

The number of analyzed BHT2 events are counted by the codes for the signal reconstruction which is different to that for the equivalent MB events counting, so the number of equivalent MB events corresponding to the signal reconstruction should be calculated by the formula Equation 3.9.

Run	$N_{\text{MB}}^{\text{eqv.}}(\text{on-line})$	$N_{\text{BHT2}}(\text{on-line})$	$N_{\text{BHT2}}(\text{Ana.})$	$\frac{ Vz < 80}{ Vz < 200}$	$N_{\text{MB}}^{\text{eqv.}}$
Run15 pp	$3.1377 * 10^{12}$	$2.118 * 10^8$	$2.118 * 10^8$	0.8803	$2.7621 * 10^{12}$
Run15 pAu	$7.0724 * 10^{11}$	$1.7302 * 10^8$	$1.6580 * 10^8$	0.8149	$5.5211 * 10^{11}$

TABLE VI: Number of equivalent BBCMB events of Run15 pp and Run15 pAu corresponding the analyzed BHT2*BBCMB events. $N_{\text{MB}}^{\text{eqv.}}(\text{on-line})$ is the number of equivalent BBCMB events corresponding to the number of BHT2 events $N_{\text{BHT2}}(\text{on-line})$. $N_{\text{BHT2}}(\text{Ana.})$ is number of BHT2 events ($|Vz| < 200$ cm) used for the Upsilon signal extraction. $N_{\text{MB}}^{\text{eqv.}}$ is the number of equivalent BBCMB events before the in bunch pile-up correction.

All the numbers used for the calculation of $N_{\text{MB}}^{\text{eqv.}}$ and the $N_{\text{MB}}^{\text{eqv.}}$ itself of Run15 pp and Run15 pAu are listed in Table VI.

3.4.2 In Bunch Pileup Effects Study

Due to the very high luminosity with 2015 p+p and p+Au collisions, the effects of more than one collisions (in-bunch pile up effects) happened during a bunch crossing may not be ignored. To quantify this effects, we may start from assuming that λ is the probability that one collision happens during a given bunch-crossing. Then the probability of that there are k collisions happen in a bunch-crossing would be:

$$P_k[\text{k collisions in a bunch-crossing}] = \frac{\lambda^k e^{-\lambda}}{k!}$$

and we would have: $P_0 = e^{-\lambda}$, $P_1 = \lambda e^{-\lambda}$, $P_2 = \frac{\lambda^2}{2} e^{-\lambda}$ and $P_3 = \frac{\lambda^3}{6} e^{-\lambda}$. The contribution of $k \geq 3$ is much smaller compared to $k=1$ and $k=2$, thus ignored in our study.

Let's start from the in-bunch pile up study for p+p collisions, if let ϵ be the BBC single side fired efficiency ($\epsilon \sim 0.9$), we could classify the BBC triggered events as the following cases:

- For $k=1$, the probability of that two sides of BBC are fired:

$$P_{\text{BBC}}[k = 1] = P_1 * \epsilon^2 \tag{3.10}$$

- For $k=2$, two sides of BBC are fired can be due to following 4 cases:

1. two collisions both fire two sides of BBC
2. one collision fire two sides of BBC and another one fire only one side of BBC
3. one collision fire two sides of BBC and another one fired nothing
4. one collision fire one side of BBC and the other collision fire the other side of BBC

The probability of that two sides of BBC fired:

$$P_{\text{BBC}}[k = 2] = P_2 * [\epsilon^4 + 4 * \epsilon^3(1 - \epsilon) + 2 * \epsilon^2(1 - \epsilon)^2 + 2 * \epsilon^2(1 - \epsilon)^2] = P_2 * [\epsilon^2(2 - \epsilon)^2] \quad (3.11)$$

The fraction of k=2 events among all BBC triggered events can be obtained by

$$\text{Fraction}(k = 2) = \frac{P_{\text{BBC}}[k = 2]}{P_{\text{BBC}}[k = 1] + P_{\text{BBC}}[k = 2]} = \frac{P_2 * [\epsilon^2(2 - \epsilon)^2]}{P_2 * [\epsilon^2(2 - \epsilon)^2] + P_1 * \epsilon^2} = \frac{\lambda(2 - \epsilon)^2}{2 + \lambda(2 - \epsilon)^2} \quad (3.12)$$

The BBC rate in per bunch-crossing due to the real collisions should be the expectation of k=1 and k=2 collisions, then we have the following relation:

$$\frac{\text{BBCRate}}{9.838\text{MHz} * \frac{102}{120}} = 1 * P_1 * \epsilon^2 + 2 * P_2 * \epsilon^2(2 - \epsilon)^2 + \dots \cong \lambda e^{-\lambda} \epsilon^2 + \lambda^2 e^{-\lambda} \epsilon^2(2 - \epsilon)^2 \quad (3.13)$$

$$\frac{\text{BBCRate}/\epsilon^2}{9.838\text{MHz} * \frac{102}{120}} = \lambda e^{-\lambda} + \lambda^2 e^{-\lambda} (2 - \epsilon)^2 \cong \lambda \quad (\text{while } \lambda \text{ is small and } \epsilon \text{ close to } 1) \quad (3.14)$$

For the in-bunch pile up in p+Au collisions, the similar derivation procedures as in p+p can be performed. Let ϵ_E and ϵ_W be the efficiency of BBC east and BBC west, we could have:

$$\begin{aligned} \text{Fraction}(k=2) &= \frac{P_{\text{BBC}}[k=2]}{P_{\text{BBC}}[k=1] + P_{\text{BBC}}[k=2]} = \frac{P_2 * [\epsilon_E * \epsilon_W * (\epsilon_W - 2)(\epsilon_E - 2)]}{P_2 * [\epsilon_E * \epsilon_W * (\epsilon_W - 2)(\epsilon_E - 2)] + P_1 * \epsilon_E * \epsilon_W} \\ &= \frac{\lambda(2 - \epsilon_E) * (2 - \epsilon_W)}{2 + \lambda(2 - \epsilon_E) * (2 - \epsilon_W)} \end{aligned} \quad (3.15)$$

$$\frac{\text{BBCRate}/(\epsilon_E * \epsilon_W)}{9.838\text{MHz} * \frac{102}{120}} = \lambda * e^{-\lambda} + \lambda^2 * e^{-\lambda} * (2 - \epsilon_E) * (2 - \epsilon_W) \cong \lambda \quad (3.16)$$

The λ and $\text{Fraction}[k=2]$ can be obtained in the real data. The λ could be obtained based on the BBC rates in each run. The λ and $\text{frac}[k=2]$ distributions in Run15pp and Run15pAu are shown in Figure 51. The average of $\text{Fraction}[k=2]$ for all runs can be calculated:

$$\langle \text{Fraction}[k=2] \rangle = \frac{\sum_{\text{firstRun}}^{\text{lastRun}} \text{eqv.MB}[i\text{Run}] * \text{Fraction}(i\text{Run})}{\sum_{\text{firstRun}}^{\text{lastRun}} \text{eqv.MB}[i\text{Run}]} \quad (3.17)$$

The final equivalent number of MB events are calculated by:

$$N_{\text{MB}}^{\text{eqv.}}(\text{final}) = N_{\text{MB}}^{\text{eqv.}} * (1 + \langle \text{Frac}[k=2] \rangle) \quad (3.18)$$

The in-bunch pile up effects does not only contribute to the number of equivalent MB events, but also contribute to the corresponding BBC efficiency and vertex reconstruction efficiency. We will discuss how to take it into account on the trigger bias factors in the following sections.

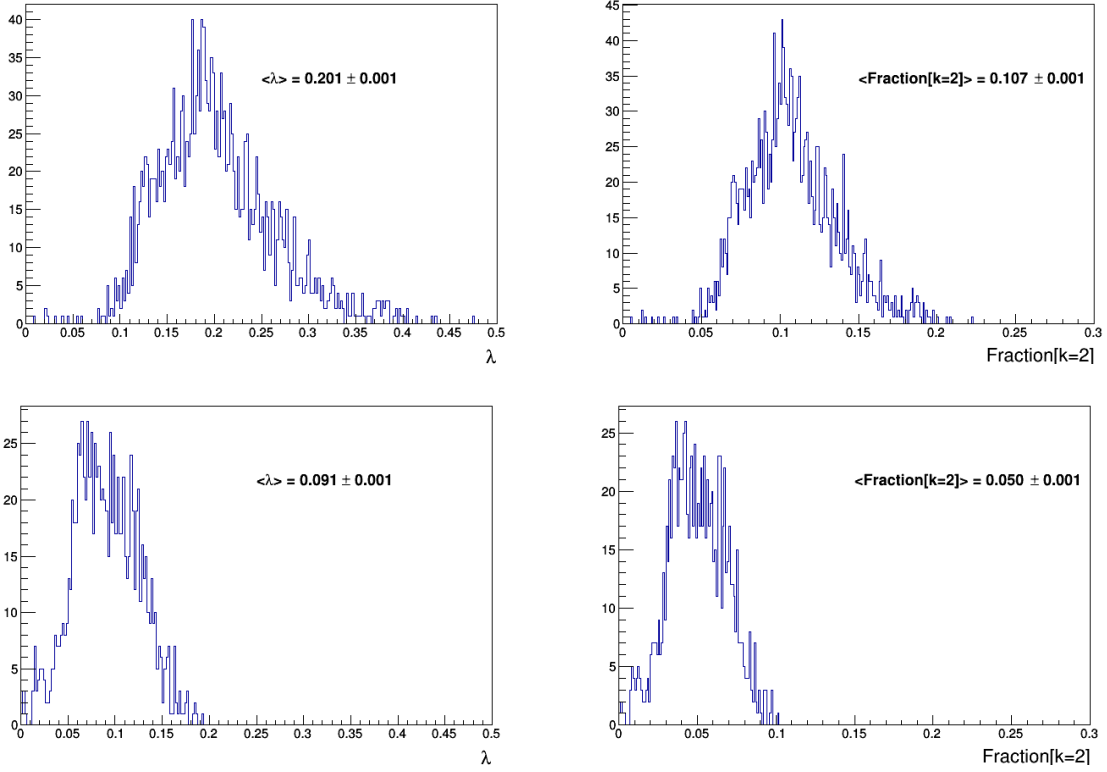


Figure 51: The λ and fraction[$k = 2$] distribution in Run15 p+p (top two panels) and pAu (bottom two panels) BBCMB events. Each entry of the histogram is corresponding to one run.

The final number of equivalent MB events for Run15 pp and Run15 pAu BHT2*BBCMB events are summarized and listed in Table VII.

	$\langle \lambda \rangle$	$\langle \text{Frac}[k = 2] \rangle$	$N_{\text{MB}}^{\text{eqv.}}(\text{final})$
Run15 pp	0.201 ± 0.001	0.107 ± 0.001	$3.0576 * 10^{12}$
Run15 pAu	0.091 ± 0.001	0.050 ± 0.001	$5.7972 * 10^{11}$

TABLE VII: The average value of λ , $\text{Frac}[k = 2]$ and the final number of equivalent MB events $N_{\text{MB}}^{\text{eqv.}}(\text{final})$ of Run15 pp and pAu.

3.4.3 Trigger Bias Factors (TB) are Studied from Simulation

In the simulation, the Monte Carlo (MC) events are generated by PYTHIA/HIJING for Run15 pp/pAu. These MC events are feed into the STAR GEANT detector simulator, the simulated MC signals from STAR GEANT are mixed with those from the Zero-Bias real data. In this way, the trigger bias study is done under the similar environment as the real data taken.

3.4.3.1 Trigger Bias Factor in Run15 pp

Similar to the $N_{\text{MB}}^{\text{eqv.}}$, the efficiency of $\epsilon_{\text{MB}}^{\text{BBC}}$, $\epsilon_{\text{particle}}^{\text{BBC}}$, $\epsilon_{\text{MB}}^{\text{goodvtx}}$, $\epsilon_{\text{particle}}^{\text{goodvtx}}$ should also be corrected with the in-bunch pile up effects with $\text{Frac}[k = 2]$. That is to calculate their average values from $k=1$ and $k=2$ cases. The average BBC trigger efficiency can be obtained by:

$$\langle \epsilon \rangle = \epsilon[k = 1] * \text{Frac}[k = 1] + \epsilon[k = 2] * \text{Frac}[k = 2]$$

$$\langle \epsilon_{\text{MB}}^{\text{BBC}} \rangle = \epsilon_{\text{MB}}^{\text{BBC}}[k = 1] * \text{Frac}[k = 1] + \epsilon_{\text{MB+MB}}^{\text{BBC}}[k = 2] * \text{Frac}[k = 2]$$

$$\langle \epsilon_{\text{particle}}^{\text{BBC}} \rangle = \epsilon_{\text{J}/\psi}^{\text{BBC}}[k = 1] * \text{Frac}[k = 1] + \epsilon_{\text{particle+MB}}^{\text{BBC}}[k = 2] * \text{Frac}[k = 2]$$

Where, if let ϵ_1 be BBC single side efficiency from the MB only event simulations and ϵ_2 is the BBC single side efficiency from particle (J/ ψ or Upsilon) event simulations, the values of ϵ_1 and ϵ_2 are listed in Table VIII.

FireType/EvtType	MBonly	J/ ψ	Υ	D_0
BBCsingleFire	0.9278	0.9119	0.9038	0.9179
BBCdoubleFire	0.8603	0.8316	0.8166	0.8425

TABLE VIII: Run15 pp BBC single fire and double fire efficiency, the statistical uncertainty of these efficiency values is ~ 0.001 .

The efficiency of BBC for MBonly events and Particle events for K=1 and K=2 cases are as follows:

- $\epsilon_{\text{MB}}^{\text{BBC}}[k = 1] = \epsilon_1^2$, and $\epsilon_{\text{MB}}^{\text{BBC}}[k = 2] = \epsilon_1^2(2 - \epsilon_1)^2$
- $\epsilon_{\text{particle}}^{\text{BBC}}[k = 1] = \epsilon_2^2$, and $\epsilon_{\text{particle+MB}}^{\text{BBC}}[k = 2] = \epsilon_1^2\epsilon_2^2 + [2\epsilon_1^2\epsilon_2(1 - \epsilon_2) + 2\epsilon_2^2\epsilon_1(1 - \epsilon_1)] + [\epsilon_1^2(1 - \epsilon_2^2) + \epsilon_2^2(1 - \epsilon_1^2)] + 2\epsilon_1(1 - \epsilon_1)\epsilon_2(1 - \epsilon_2) = (\epsilon_1 + \epsilon_2 - \epsilon_1\epsilon_2)^2$

Note that for the BBC efficiency of Particle event, the probability of 2 Particle (J/ ψ or Upsilon) produced in a bunch crossing can be ignored since the production rate of quarkonium in MB events is too small, so that only 1 Particle event + 1 MB event need to be considered here.

$\epsilon_{\text{MB}}^{\text{BBC}}$	$\epsilon_{\text{J}/\psi}^{\text{BBC}}$	$\epsilon_{\gamma}^{\text{BBC}}$	$\epsilon_{\text{D}_0}^{\text{BBC}}$
0.8608	0.8316	0.8169	0.8425
$\epsilon_{\text{MB+MB}}^{\text{BBC}}$	$\epsilon_{\text{MB+J}/\psi}^{\text{BBC}}$	$\epsilon_{\text{MB}+\gamma}^{\text{BBC}}$	$\epsilon_{\text{MB+D}_0}^{\text{BBC}}$
0.9896	0.9873	0.9862	0.9882

TABLE IX: Run15 pp BBC efficiencies for K=1 and K=2 , the statistical uncertainty of these efficiency values is ~ 0.001 .

As the good vertex reconstruction efficiency. $\epsilon_{\text{MB}}^{\text{goodvtx}}$ will be canceled, no further correction needed for it. In the Zero-Bias data, the probabilities of $k=0$, $k=1$ and $k=2$ can be given by Poisson distributions: $P_0 = e^{-\lambda}$, $P_1 = \lambda e^{-\lambda}$, $P_2 = \frac{\lambda^2}{2} e^{-\lambda}$. Let the probability to produce a Particle (J/ ψ , Upsilon or D_0) in a event be p_{particle} , p_{particle} should be $\ll P_0, P_1, P_2$. Since a MC Particle event is embedded into a Zero-Bias event, in principle, each event in these simulation should be a Particle event + ZB event. For the $\epsilon_{\text{particle}}^{\text{goodvtx}}$ in the PYTHIA+GEANT+ZeroBias simulation is from the total contribution of 1 Particle event + 1 ZB event($k=0, k=1, k=2$). Thus the relative contributions of $k=0, k=1, k=2$ will be proportional to $p_{\text{J}/\psi} * P_0 : p_{\text{J}/\psi} * P_1 : p_{\text{J}/\psi} * P_2$, which is actually same as in the real data of our analysis. Thus average $\epsilon_{\text{J}/\psi}^{\text{goodvtx}}$ can be obtained directly from the PYTHIA + GEANT + ZeroBias simulations.

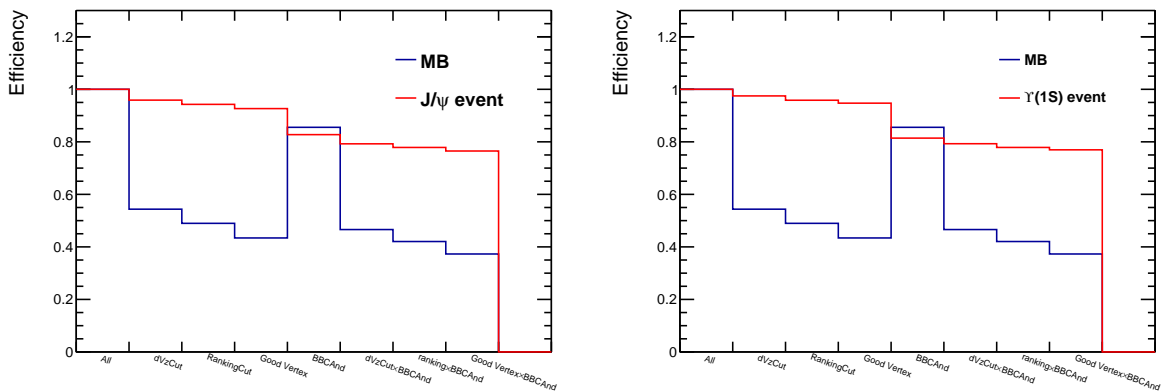


Figure 52: Efficiency corresponding to the following cuts: $dVzCut = “|mcVz - rcVz| < 1.5 \text{ cm}”$, $RankingCut = “ranking > 0”$, $good \text{ Vertex} = “dVzCut * RankingCut”$, $BBCAnd = “BBC \text{ both sides fired}”$ for MBonly events and J/ψ or γ events are calculated and compared in the figures.

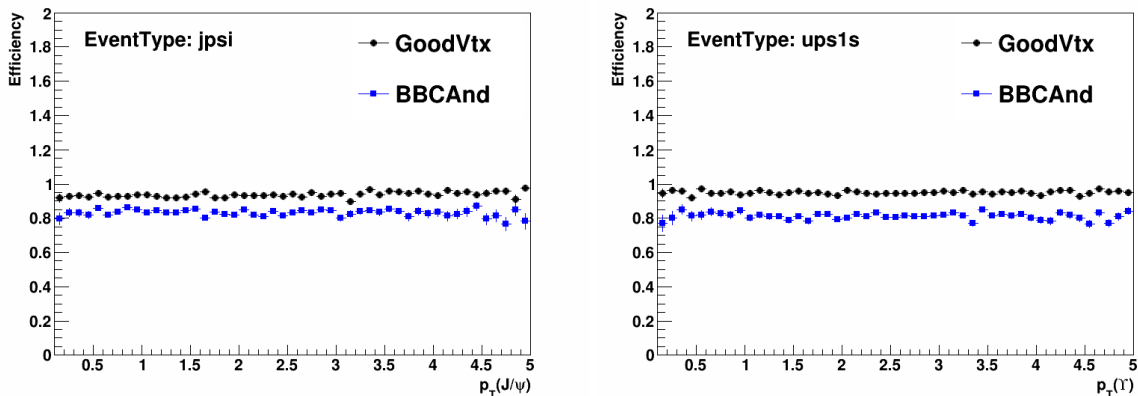


Figure 53: BBC efficiency and the good vertex efficiency in J/ψ and γ events.

$\langle \epsilon_{\text{MB}}^{\text{BBC}} \rangle$	$\langle \epsilon_{\text{J}/\psi}^{\text{BBC}} \rangle$	$\langle \epsilon_{\Upsilon}^{\text{BBC}} \rangle$	$\langle \epsilon_{\text{D}_0}^{\text{BBC}} \rangle$
0.8746	0.8483	0.8350	0.8582
$\langle \epsilon_{\text{MB}}^{\text{goodVtx}} \rangle$	$\langle \epsilon_{\text{J}/\psi}^{\text{goodVtx}} \rangle$	$\langle \epsilon_{\Upsilon}^{\text{goodVtx}} \rangle$	$\langle \epsilon_{\text{D}_0}^{\text{goodVtx}} \rangle$
0.4340	0.9266	0.9472	0.8487

TABLE X: The average value of BBC efficiency and good Vertex efficiency for MOnly, J/ ψ , Υ , D_0 events for Run15 pp. (The statistical uncertainty of these efficiency values is ~ 0.001 , so can be ignored.)

	J/ ψ	Υ	D_0
TrigBias("Tune:HF")	0.4829	0.4800	0.5211
TrigBias("Tune:4Cx")	0.4816	0.4837	
TrigBias Syst. Error (%)	$\pm 3.0\%$	$\pm 3.0\%$	

TABLE XI: Run15 pp Trigger Bias $\frac{\langle \epsilon_{\text{MB}}^{\text{BBC}} \rangle \langle \epsilon_{\text{MB}}^{\text{goodvtx}} \rangle}{\langle \epsilon_{\text{Particle}}^{\text{BBC}} \rangle \langle \epsilon_{\text{Particle}}^{\text{goodvtx}} \rangle}$ (Particle = J/ ψ or Υ) using two Pythia8 settings "Tune:HF" and "Tune:4Dx".

The average value of BBC efficiency and good Vertex efficiency for MOnly, J/ ψ , Υ , D_0 events are listed in Table X. The trigger bias factors $\frac{\langle \epsilon_{\text{MB}}^{\text{BBC}} \rangle \langle \epsilon_{\text{MB}}^{\text{goodvtx}} \rangle}{\langle \epsilon_{\text{Particle}}^{\text{BBC}} \rangle \langle \epsilon_{\text{Particle}}^{\text{goodvtx}} \rangle}$ are calculated and listed in Table XI. In our analysis, the default settings for the Particle events (J/ ψ , Υ , D_0) is the STAR official HF tune. We also obtained the Trigger-Bias factor with another widely used Pythia8 settings: Tune:4Dx, and the Trigger-Bias factor from Tune:4Dx is very close to the default one. The relative difference of Trigger bias from these two Pythia8 settings is much

smaller than the systematic uncertainty of Trigger bias factor of J/ψ analysis of Run12 pp [75] (3%, which is estimated from the difference between Pythia8 and Pythia6), we will quote 3% as the systematic uncertainty of the Trigger bias factor for our J/ψ and Υ analysis with Run15 p+p BHT2*BBCMB data. The Trigger-Bias of D_0 in p+p collisions is calculated and listed together with J/ψ , Υ , that is for the Trigger-Bias study in Run15 pAu collisions. It will be discussed in Section 3.4.3.2.

3.4.3.2 Trigger Bias factor in Run15 pAu

Due to lack of effective simulation tool for the quarkonium production in p+Au collisions, the best way to study the Trigger Bias for the measurements of J/ψ or Υ in Run15 p+Au 200 GeV collisions is to study the D_0 Trigger Bias by the Hijing [72]+GEANT+Zero-Bias simulation. The idea is mainly based on the fact that the Trigger bias of D_0 , J/ψ and Υ are very close to each other in the p+p collisions as shown in Table XI of section 3.4.3.1.

FireType/EvtType	MBonly	D_0
BBCsingleEast	0.9506	0.9879
BBCsingleWest	0.8788	0.8931
BBCdoubleFire	0.8355	0.8823

TABLE XII: Run15 pAu BBC single fire and double fire efficiency(The statistical uncertainty is 0.001, thus can be ignored.)

If let ϵ_E and ϵ_W be the efficiency of east BBC and west BBC single side fire efficiency, correspondingly. Based on the similar procedures, we could derive that:

$$\lambda \cong \frac{\text{BBCRate}/(\epsilon_E * \epsilon_W)}{9.383\text{MHz} * (102/120)}$$

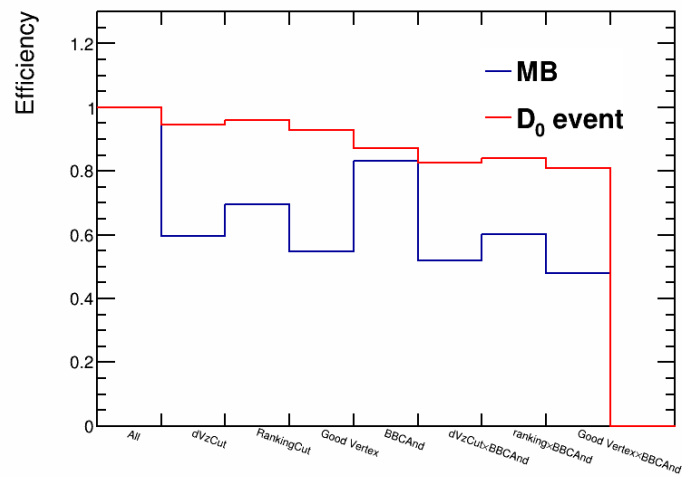


Figure 54: Efficiencies comparison between MB-only events and D₀ events with different cuts in the Hijing+GEANT+ZeroBias simulation

The average BBC trigger efficiency can be calculated by:

$$\langle \epsilon \rangle = \epsilon[k=1] * \text{Frac}[k=1] + \epsilon[k=2] * \text{Frac}[k=2]$$

$$\langle \epsilon_{\text{MB}}^{\text{BBC}} \rangle = \epsilon_{\text{MB}}^{\text{BBC}}[k=1] * \text{Frac}[k=1] + \epsilon_{\text{MB+MB}}^{\text{BBC}}[k=2] * \text{Frac}[k=2]$$

$$\langle \epsilon_{\text{D}_0}^{\text{BBC}} \rangle = \epsilon_{\text{D}_0}^{\text{BBC}}[k=1] * \text{Frac}[k=1] + \epsilon_{\text{D}_0+\text{MB}}^{\text{BBC}}[k=2] * \text{Frac}[k=2]$$

$\epsilon_{\text{MB}}^{\text{BBC}}$	$\epsilon_{\text{D}_0}^{\text{BBC}}$
0.8355	0.8823
$\epsilon_{\text{MB+MB}}^{\text{BBC}}$	$\epsilon_{\text{MB+D}_0}^{\text{BBC}}$
0.9829	0.9865

TABLE XIII: Run15 pAu BBC efficiencies for K=1 and K=2

and we have:

- $\epsilon_{\text{MB}}^{\text{BBC}}[k=1] = \epsilon_{\text{E}}(\text{MB}) * \epsilon_{\text{W}}(\text{MB})$
- $\epsilon_{\text{MB}}^{\text{BBC}}[k=2] = \epsilon_{\text{E}}(\text{MB}) * \epsilon_{\text{W}}(\text{MB}) * (2 - \epsilon_{\text{E}}(\text{MB}))(2 - \epsilon_{\text{W}}(\text{MB}))$
- $\epsilon_{\text{D}_0}^{\text{BBC}}[k=1] = \epsilon_{\text{E}}(\text{D}_0) * \epsilon_{\text{W}}(\text{D}_0)$

- $\epsilon_{D_0+MB}^{BBC}[k=2] = \epsilon_E(MB) * \epsilon_W(MB) * \epsilon_E(D_0) * \epsilon_W(D_0) - \epsilon_E(MB) * \epsilon_W(MB)(\epsilon_E(D_0) + \epsilon_W(D_0)) - (\epsilon_E(MB) + \epsilon_W(MB)) * \epsilon_E(D_0) * \epsilon_W(D_0) + \epsilon_E(MB) * \epsilon_W(MB) + \epsilon_E(D_0) * \epsilon_W(D_0) + \epsilon_E(MB) * \epsilon_W(D_0) + \epsilon_W(MB) * \epsilon_E(D_0)$

Where $\epsilon_E(MB), \epsilon_W(MB), \epsilon_E(D_0), \epsilon_W(D_0)$ is BBC single side efficiencies from the MB only or the D_0 event simulations. Note that for the BBC efficiency of D_0 event, we can ignore the probability of 2 D_0 produced in a bunch crossing, instead, we consider 1 D_0 event + 1 MB event here.

$\langle \epsilon_{MB}^{BBC} \rangle$	$\langle \epsilon_{D_0}^{BBC} \rangle$	$\langle \epsilon_{MB}^{goodVtx} \rangle$	$\langle \epsilon_{D_0}^{goodVtx} \rangle$
0.8428	0.8874	0.5464	0.9268

TABLE XIV: The average value of BBC efficiency and good Vertex efficiency for MBonly and D_0 events for Run15 pAu.

In Table XIV, the average of BBC efficiency and good vertex efficiency for MBonly and D_0 events are listed. We want to make use of these numbers together with Table X to estimate the average BBC efficiency and good vertex efficiency for J/ψ and Υ measurement in Run15 p+Au collisions.

As shown in Table X, the $\langle \epsilon_{D_0}^{BBC} \rangle$ is very close to $\langle \epsilon_{J/\psi}^{BBC} \rangle$ and $\langle \epsilon_{\Upsilon}^{BBC} \rangle$, and $\langle \epsilon_{D_0}^{BBC} \rangle$ is larger than $\langle \epsilon_{J/\psi}^{BBC} \rangle$ and larger than $\langle \epsilon_{\Upsilon}^{BBC} \rangle$ in p+p collisions. Thus we would expect this relation will keep same in p+Au collisions. On the other hand, the $\langle \epsilon_{D_0}^{BBC} \rangle$ (0.8874) in p+Au

collisions is higher than that (0.8582) in p+p collisions, similarly $\langle \epsilon_{J/\psi}^{\text{BBC}} \rangle$ and $\langle \epsilon_{\Upsilon}^{\text{BBC}} \rangle$ in p+Au collisions can be expected to be higher than those in p+p collisions. Thus the $\langle \epsilon_{J/\psi}^{\text{BBC}} \rangle$ in pAu collisions should be within 0.8483 and 0.8874, and $\langle \epsilon_{\Upsilon}^{\text{BBC}} \rangle$ be within 0.8350 and 0.8874. We choose the mid value as the estimated values of $\langle \epsilon_{J/\psi}^{\text{BBC}} \rangle$ and $\langle \epsilon_{\Upsilon}^{\text{BBC}} \rangle$. The number are listed in Table XV.

As shown in Table X, the $\langle \epsilon_{D_0}^{\text{goodVtx}} \rangle$ is significantly lower than $\langle \epsilon_{J/\psi}^{\text{goodVtx}} \rangle$ and $\langle \epsilon_{\Upsilon}^{\text{goodVtx}} \rangle$ in p+p collisions, thus the $\langle \epsilon_{D_0}^{\text{goodVtx}} \rangle$ in p+Au collisions is expected to be still lower than $\langle \epsilon_{\Upsilon}^{\text{goodVtx}} \rangle$ although may be not that significant as in p+p collisions. At the mean time, the good vertex efficiency of J/ψ or Υ in p+Au collisions should also be higher than what in p+p collisions. So $\langle \epsilon_{J/\psi}^{\text{goodVtx}} \rangle$ should be > 0.9268 and < 1 , and $\langle \epsilon_{\Upsilon}^{\text{goodVtx}} \rangle$ should be > 0.9472 and < 1 . The mid values are used as the values of $\langle \epsilon_{J/\psi}^{\text{goodVtx}} \rangle$ and $\langle \epsilon_{\Upsilon}^{\text{goodVtx}} \rangle$ as listed in Table XV.

$\langle \epsilon_{J/\psi}^{\text{BBC}} \rangle$	$\langle \epsilon_{\Upsilon}^{\text{BBC}} \rangle$	$\langle \epsilon_{J/\psi}^{\text{goodVtx}} \rangle$	$\langle \epsilon_{\Upsilon}^{\text{goodVtx}} \rangle$
0.8679 ± 0.0195	0.8862 ± 0.0262	0.9634 ± 0.0366	0.9736 ± 0.0264

TABLE XV: The estimated average values and uncertainties of BBC efficiency and good Vertex efficiency for J/ψ and Υ events for Run15 pAu. (The systematic uncertainty is estimated by $\pm(\text{UpLimit} - \text{LowLimit})/2$)

Particle	D ₀	J/ψ	Υ
TrigBias	0.5599	0.5508 ± 0.0243	0.5338 ± 0.0214
TrigBias Syst. Error (%)		± 5.3%	± 5.0%

TABLE XVI: Trigger Bias $\frac{\langle \epsilon_{\text{MB}}^{\text{BBC}} \rangle \langle \epsilon_{\text{MB}}^{\text{goodvtx}} \rangle}{\langle \epsilon_{\text{particle}}^{\text{BBC}} \rangle \langle \epsilon_{\text{particle}}^{\text{goodvtx}} \rangle}$ for D₀, J/ψ and Υ measurements in Run15 p+Au collisions. (The systematic uncertainty of trigger bias factors propagated from the systematic uncertainty of BBC efficiency and good Vertex efficiency are listed in the second row. The final systematic uncertainty of Trigger Bias factor also take into account the uncertainty of 3% from different Pythia versions, are listed in the last row.)

The Trigger Bias factor for J/ψ and Υ measurements in Run15 p+Au collisions calculated and listed in Table XVI. The much larger systematic uncertainty in p+Au collisions than those in p+p collisions is due to the lack of effective simulation package for quarkonium production in p+Au collisions.

3.4.4 A Summary for Number of equivalent MB events and Trigger Bias Factor

The final values of the number of equivalent MB events and Trigger Bias factors for J/ψ or Υ measurements with Run15 pp and Run15 pAu BHT2*BBCMB triggered data are listed in the Table XVII.

	N _{MB} ^{eqv.} (final)	$\langle \epsilon_{\text{MB}}^{\text{goodVtx}} \rangle$	Trig-Bias (J/ψ)	Trig-Bias(Υ)
Run15 pp	3.0576 * 10 ¹²	0.4340	0.4829 ± 0.0145	0.4800 ± 0.0144
Run15 pAu	5.7972 * 10 ¹¹	0.5464	0.5508 ± 0.0292	0.5338 ± 0.0267

TABLE XVII: The final number of equivalent MB events, good vertex efficiency and the trigger bias factor for J/ψ and Υ measurements with Run15 pp and pAu BHT2*BBCMB triggered data.

3.5 Systematic uncertainties of Υ measurements in Run15 pp and pAu

The systematic uncertainties of Υ cross section measurements in Run15 pp and Run15 pAu are obtained in different sources:

- Fitting Ranges: the default fitting range is 7.0-14.0 GeV/c², the fitting ranges are changed to 6.6-14.0, 7.4-14.0, 7.0-13.6, 7.0-13.8, 6.8-13.8 GeV/c² and obtain cross sections, take the maximum difference relative to default cross section as the systematic uncertainty from the fitting range.
- Binning Width: the default bin width is 0.2 GeV/c², changed to 0.16 GeV/c² and 0.4 GeV/c², take the maximum difference relative to default cross section as the systematic uncertainty from the binning width.
- Υ Templates: The default template Width and the Shift factor are obtained from the fitting of smeared signals. The smeared template rely on the fitted width and mean of real J/ψ, so the width and mean of Υ templates are varied to cover the fitted statistical uncertainty of J/ψ mean and width. The widths of Υ templates are changed by ±5%, and the shift of the mean of Υ templates are changed ±10%.
- B \bar{B} (BB) and Drell-Yan (DY) Templates: The BB and DY shapes are from the PYTHIA simulation with the detector efficiency embedded. The default PYTHIA settings in this analysis for the BB and DY simulation are from the PHENIX tuned settings which could well describe the measured BB and DY production at RHIC energy. There is another PYTHIA settings tuned to match results of di-lepton analysis. We take the difference

of our physics results based on BB and DY shaped from this two PYTHIA settings as a systematic uncertainty of BB and DY shapes.

- $\Upsilon(1S):\Upsilon(2S):\Upsilon(3S)$ relative ratio: The default value of these relative ratios between each Υ state are from the world wide average value (1:0.275:0.128) for both Run15pp and Run15pAu, the ratios are changed to (1:0.275:0) for Run15pp systematic uncertainty. The CMS measured ratios (1:0.22:0.08) in pPb collisions [46] are used for the for the systematic uncertainty estimation of Run15 pAu.
- Tracking “nHitsFits and nHitsDedx” Cuts: The default cuts used in Run15 pp and pAu is “nHitsFits \geq 25 and nHitsDedx \geq 15”, the cuts are changed to “nHitsFits \geq 20 and nHitsDedx \geq 10” for the systematic uncertainty calculation.
- Dca cut: the default cut is “dca < 1.5 cm”, the cuts are changed to “dca < 1.25 cm” and “dca < 1.75 cm” for the systematic uncertainty calculation.
- Trigger Threshold Adc0 cut: the default Adc0 cut is “Adc0 \geq 300”, the cut is changed to “Adc0 \geq 303” for the systematic uncertainty calculation.
- E/p cut: the default cut is “0.7 < E/p < 2.0”, the cut is changed to “0.8 < E/p < 1.8” and “0.6 < E/p < 2.5” systematic uncertainty calculation.
- $n\sigma_e$ cut: the mean and σ of $n\sigma_e$ are changed up and down according to statistical uncertainties of the mean and σ from fitting

- BEMC matching “zDist and phiDist” cut: the default cut is “zDist < 10 and phiDist < 1”, these cuts are changed to “zDist < 11 and phiDist < 1.1” and “zDist < 9 and phiDist < 0.9” for systematic uncertainty calculation.
- Υ p_T curve parameter “T” value: The default value of T is 1.127 is obtained from the fitting of previous STAR Υ measurement in U+U collisions [48], and this value is changed to 1.1 and 1.3 for systematic uncertainty calculation.
- The uncertainty of geometrical acceptance (for p+p and p+Au collisions): The uncertainty of the polarization of Υ mesons, it will be studied later.

The other common systematic uncertainties:

- The uncertainty from the NSD cross section measurement (for p+p collisions): $\sigma_{\text{NSD}} = 30 \pm 2.4$ mb
- The uncertainty from the Glauber model parameter (for p+Au collisions): $N_{\text{coll}} = 4.7 \pm 0.3$ [73]
- The uncertainty from the Trigger Bias factor: $\text{TrigBias}(\text{pp}) = 0.4800 \pm 0.0144$, $\text{TrigBias}(\text{pAu}) = 0.5338 \pm 0.0267$

3.5.1 Systematic uncertainties of Υ cross section measurements in Run15 pp

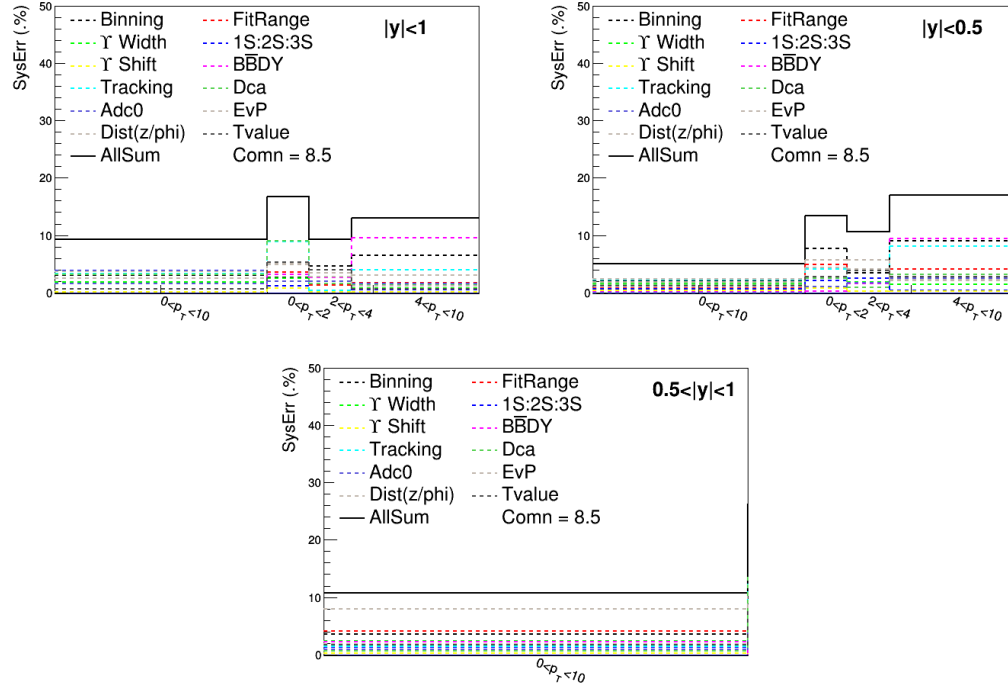


Figure 55: Systematic uncertainties from different sources for $\Upsilon(1S+2S+3S)$ cross section as function of p_T in Run15pp within rapidity ranges: $|y| < 1$, $|y| < 0.5$, $0.5 < |y| < 1$

3.5.2 Systematic uncertainties of Υ invariant yield measurements in Run15 pAu

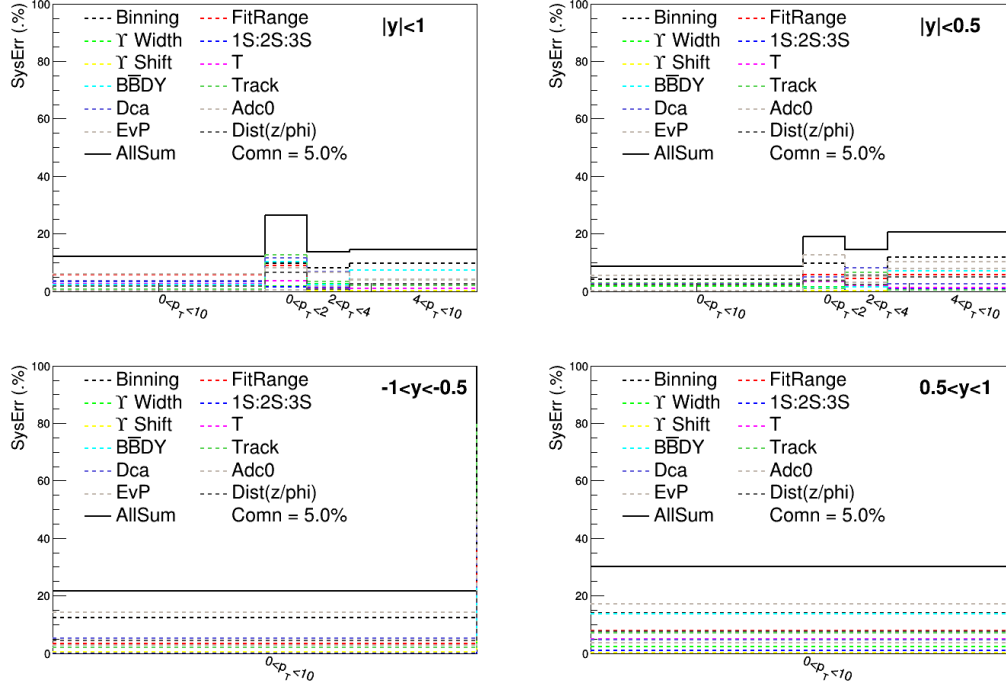


Figure 56: Systematic uncertainties from different sources for $\Upsilon(1S+2S+3S)$ invariant yield as function of p_T measurement in Run15pAu within rapidity ranges: $|y| < 1$, $|y| < 0.5$, $0.5 < |y| < 1$

3.5.3 Systematic uncertainties of ΥR_{pA} measurements

The R_{pA} is calculated based on the Υ cross section measurements from Run15 pp and the invariant yield measurement from Run15 pAu, thus the systematic uncertainties for the R_{pA} are contributed from both of these two measurements. The systematic uncertainty of R_{pA} can be separated into two parts:

1. Common normalization uncertainty(those uncertainties which will move the values of R_{pA} in each small y bin or p_T bin up or down synchronously):

- from the systematic uncertainty of Run15 pp:

$$\sigma_{\text{NSD}} = 30 \pm 2.4 \text{ mb}$$

$$\text{TrigBias(pp)} = 0.4800 \pm 0.0144$$

- from the systematic uncertainty of Run15 pAu:

The Glauber model parameter (for p+Au collisions): $N_{\text{coll}} = 4.7 \pm 0.3$

$$\text{TrigBias(pAu)} = 0.5338 \pm 0.0267$$

2. Uncertainties for each individual data points:

- Uncorrelated uncertainties sources:

$$\text{ErrorSum}_{\text{uncorr}} = \sqrt{\sum_{\text{pp,pAu}} \sum_{\text{isource}} \sigma_{\text{isource}}^2}$$

, `isource` = “Binning”, “FitRange”, “ Υ Templates,” “Upsilon 1S,2S,3S relative ratio”, “BB,DY Templates”, “ Υ p_T curve parameter T value” in Run15pp and Run15pAu

- Correlated uncertainties:

$$\text{ErrorSum}_{\text{corr}} = \sqrt{\sum_{\text{isource}} (\sigma_{\text{isource}}^{\text{pAu}} - \sigma_{\text{isource}}^{\text{pp}})^2}$$

, `isource` = “Tracking”, “Dca”, “E/p”, “zDist”, “phiDist”, “Adc0” cuts.

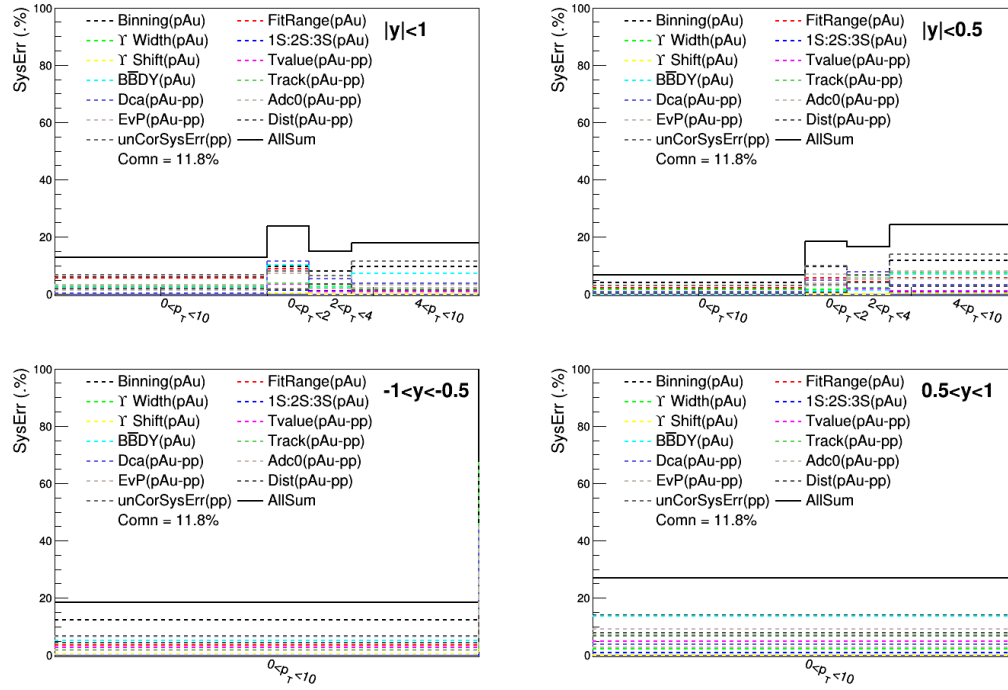


Figure 57: Systematic uncertainties from different sources for R_{pA} of $\Upsilon(1S+2S+3S)$ as function of p_T within rapidity ranges: $|y| < 1$, $|y| < 0.5$, $0.5 < y < 1$, and $-1.0 < y < -0.5$

CHAPTER 4

MEASUREMENTS OF UPSILON PRODUCTION IN AU+AU COLLISIONS

4.1 Data Sets

In this analysis, Υ are measured via $\Upsilon \rightarrow e^+e^-$ decay channel with the data taken in 2011 Au+Au collisions at $\sqrt{s_{NN}} = 200$ GeV. The data are triggered by NPE18 trigger, which triggers on the high transverse energy (E_T) particle events by requiring at least one of the BEMC towers is fired (the deposited energy in BEMC tower should pass the trigger threshold ~ 4.3 GeV).

4.1.1 Event Selection

Each event used for this analysis is required to have a valid reconstructed collision vertex (primary vertex reconstructed by TPC). The reconstructed collision vertex is required to be within 30 cm of the TPC center along the beam direction (z direction), which is limited by the STAR official StRefMult class [76] was only performed within $|V_z| < 30$ cm. The left panel of Figure 58 shows the V_z^{TPC} distribution of all NPE18 triggered events in Run11 AuAu data. In order to reject those events with wrong reconstructed primary vertex, the difference between the vertex along z direction reconstructed by the TPC (V_z^{TPC}) and the VPD (V_z^{VPD}) is required to be less than 3 cm, where, the difference between V_z^{TPC} and V_z^{VPD} distributions is shown in right panel of Figure 58. Those events from the collisions between beam and beam pipe also need to be rejected by requiring the distance of TPC vertex along radius direction (V_r) less than

2 cm. Finally, there are 38.59 M events passing the event selection requirement. The number of events corresponding to each requirement are listed in Table XVIII.

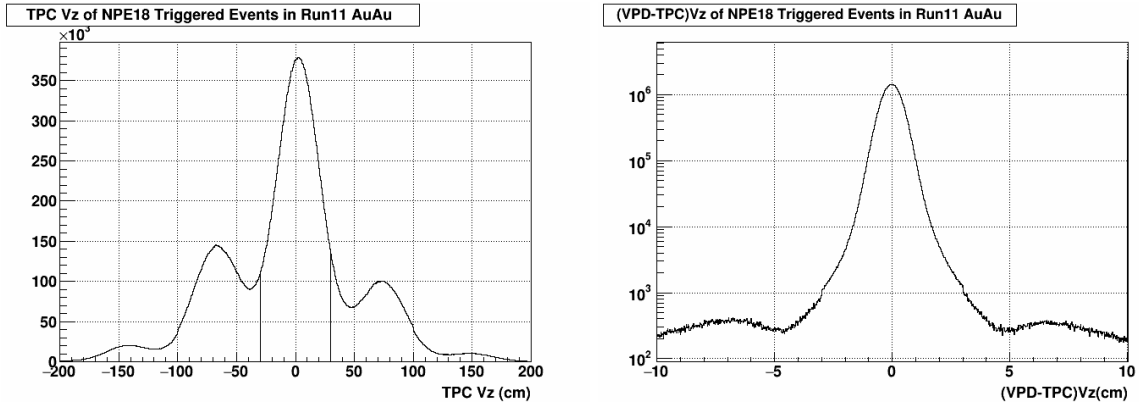


Figure 58: The left panel shows V_z^{TPC} distribution and the right panel shows the difference between V_z^{TPC} and V_z^{VPD} of NPE18 triggered events in Run11 AuAu data.

Cuts	Number of events [M]
$ V_z^{\text{TPC}} < 200\text{cm}$	79.30
$ V_z^{\text{TPC}} < 30\text{cm}$	39.60
$ V_z^{\text{TPC}} < 30\text{ cm} \ \& \ V_z^{\text{TPC}} - V_z^{\text{VPD}} < 3\text{ cm} \ \& \ \sqrt{V_x^2 + V_y^2} < 2\text{ cm}$	38.59

TABLE XVIII: Number of NPE18 triggered events in Run11 AuAu data

The multiplicity distribution in TPC and corrected multiplicity distribution in TPC based on the Glauber Monte Carlo simulation for NPE18 triggered events in Run11 AuAu data are shown in Figure 59. The centrality distribution and the re-weight factor corrected centrality distribution are shown in Figure 60. The average number of participants and binary collisions for each centrality bin are listed in Table XIX.

Cent. Min(%)	Cent Max (%)	$\langle N_{\text{part}} \rangle$	$\langle N_{\text{coll}} \rangle$
0.0	5.0	349.64479 ± 2.10277	1048.11384 ± 27.46719
5.0	10.0	302.22503 ± 6.06888	838.41152 ± 22.71669
0.0	10.0	325.47688 ± 3.62739	941.23714 ± 26.27357
10.0	20.0	237.26805 ± 8.51684	593.66913 ± 30.17927
20.0	30.0	169.03745 ± 10.52574	366.44382 ± 32.33380
30.0	40.0	116.73536 ± 11.06074	216.45403 ± 29.20314
40.0	50.0	76.87774 ± 10.67252	120.05550 ± 23.36185
50.0	60.0	47.78713 ± 9.49642	62.17938 ± 16.84881
60.0	70.0	27.38266 ± 7.65968	29.65826 ± 10.89828
70.0	80.0	14.38576 ± 5.19649	13.09320 ± 5.88355
0.0	60.0	161.63208 ± 8.91690	381.42696 ± 25.93762
0.0	80.0	126.65486 ± 7.69572	291.90194 ± 20.46382

TABLE XIX: The average number of participants ($\langle N_{\text{part}} \rangle$) and the average binary collisions ($\langle N_{\text{coll}} \rangle$) in different centrality bins [76].

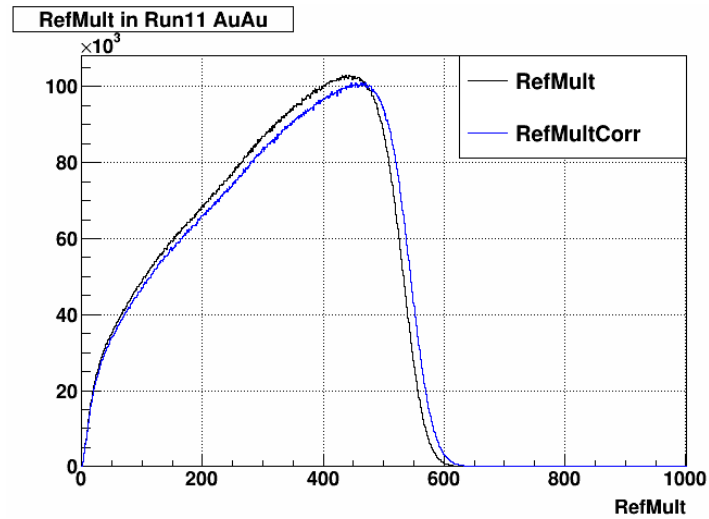


Figure 59: The black line shows the multiplicity distribution in TPC for NPE18 triggered events in Run11 AuAu data, and the blue line shows the corrected multiplicity distribution in TPC based on the Glauber Monte Carlo simulation.

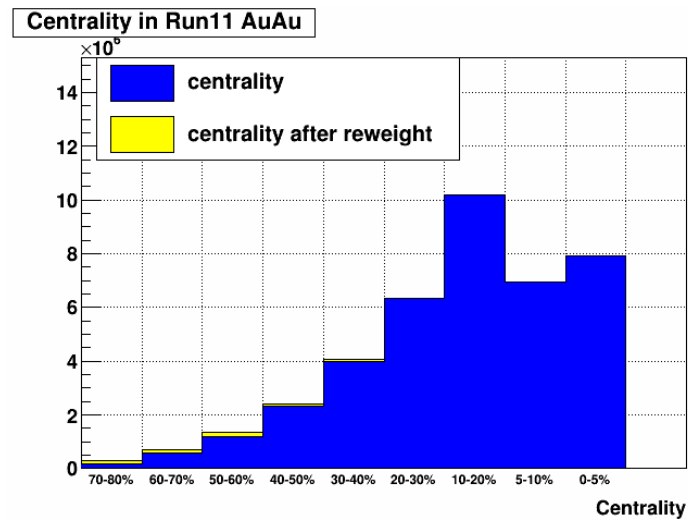


Figure 60: The centrality distribution and the re-weighted centrality distribution of NPE18 triggered events in Run11 AuAu data

4.1.2 Electron track selection

The cuts variables used in Run11 AuAu analysis are basically same as that in Run15 pp and pAu analysis except the `nHitsDedx` which is not used in Run11 AuAu analysis. The details of cut sets are listed as follows:

- $n\text{HitsFit} \geq 20$, $R \geq 0.52$, $0 < dca \leq 1.5$ cm, $|\eta| \leq 1$, $0.2 < p < 30$ GeV/c
- $-1.2 \leq n\sigma_e \leq 3.0$, $0.3 \leq E/p \leq 1.8$, $|z\text{Dist}| \leq 10$, $|\text{phiDist}| \leq 0.1$
- $\text{DsmAdc} > 18$ & $\text{Adc0} \geq 300$ & $p_T \geq 3.5$ GeV/c

For each Upsilon candidate (electron pairs), we also require:

- $|y| < 1$ & $0 < p_T < 15$ GeV/c
- at least one triggered electron per electron pair
- As Υ has very large mass ($m_{\Upsilon(1S)} = 9.46$ GeV/c²), their daughter electrons usually have much high momentum. To improve the signal significance, the cuts on the electron momentum are also applied: at least one electron with $p \geq 4.5$ GeV/c and both electrons should have $p \geq 3.5$ GeV/c.

4.2 Efficiency Study with Embedding Samples

4.2.1 Single Electron Reconstruction Efficiency

The single electron efficiency is studied based on the STAR official Υ embedding samples except the $n\sigma_e$ cut efficiency since the STAR embedding cannot well reproduce the energy loss ($\frac{dE}{dx}$) information. The $n\sigma_e$ distribution of electrons is studied from the partner electron of a

photonic electron pairs, such distribution can be fitted by a Gaussian function. The fitted mean and width of a Gaussian function for each p_T bin are shown in Figure 61.

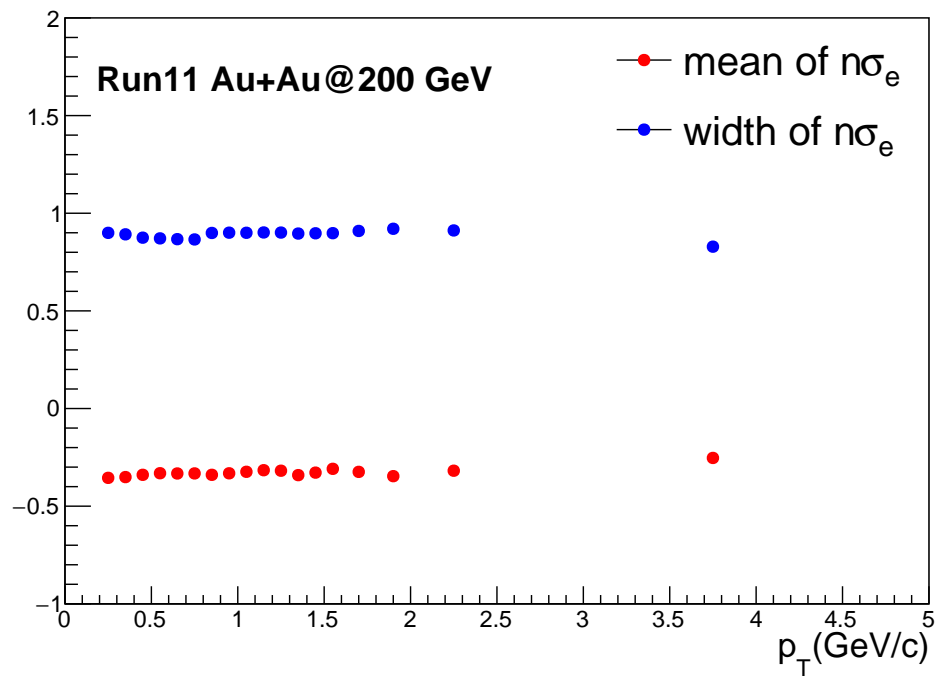


Figure 61: The fitted mean and width of $n\sigma_e$ as function of p_T in Run11 AuAu 200 GeV data

Figure 62 show the single electron efficiencies corresponding to different requirements (“TPC”, “EMC”, “Trg BHT2”) in different centralities of Run11 200 GeV AuAu data.

Where:

- “TPC” is defined as “ $p_T \geq 0.2 \text{ GeV}/c$
& $n\text{HitsFits} \geq 20$ & $\text{Ratio} \geq 0.52$
& $0 < \text{Dca} < 1.5$ & $-1.2 < n\sigma_e < 3.0$ ”
- “EMC” is defined as “ $e > 0.1 \text{ GeV}$ & $1.5 < p_T < 30 \text{ GeV}/c$
& $|z\text{Dist}| < 10 \text{ cm}$ & $|\text{phiDist}| < 0.1 \text{ cm}$ ” & $0.3 < E/p < 2.0$ ”
- “Trg BHT2”: “ $p_T > 3.5 \text{ GeV}/c$ & $\text{DsmAdc} > 18$ & $\text{Adc0} \geq 300$ ”

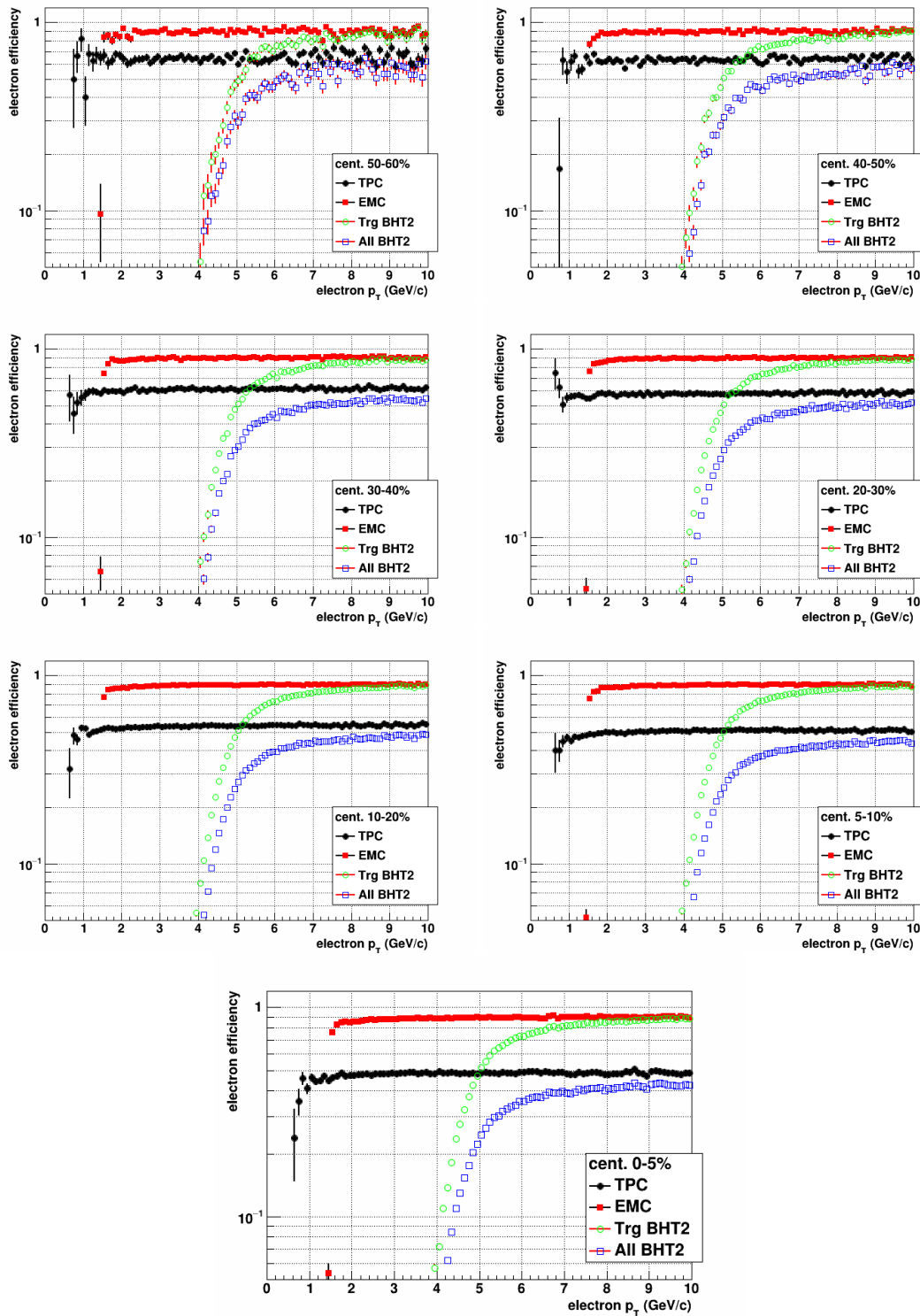


Figure 62: Efficiencies of single electron as function of p_T corresponding to different requirements (“TPC”, “EMC”, “Trg BHT2”) in different centralities of Run11 200 GeV AuAu data.

4.2.2 Momentum Resolution

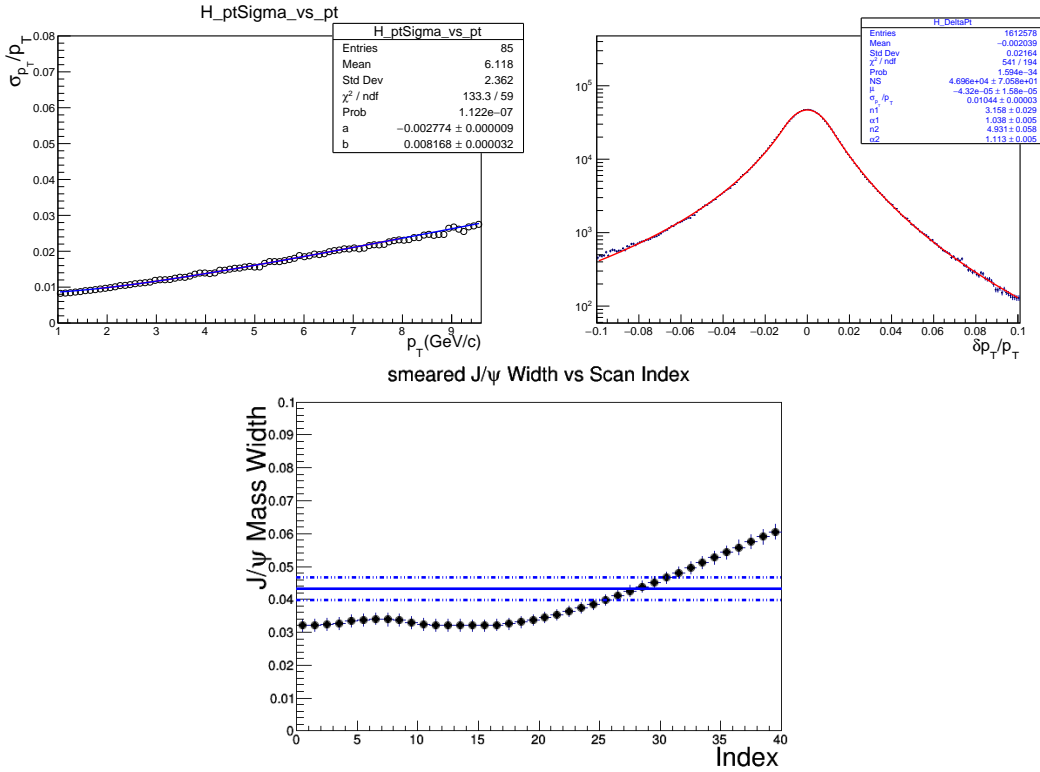


Figure 63: The top left panel shows the momentum resolution $\sigma(\frac{\delta p_T}{p_T})$ as function of p_T , fitted with a function of $f(p_T) = \sqrt{a^2(p_T)^2 + b^2}$. The top right panel shows the normalized $\delta p_T / p_T$ fitted by Double Crystal Ball function. The bottom panel shows the tuning of parameter "a" to best match the J/ψ mass width in Run11 AuAu BHT2 triggered data (The solid line is the fitted J/ψ width and the dotted lines shows the uncertainty of the fitted J/ψ width. The J/ψ p_T range is 4-10 GeV/c).

The J/ψ signals from smearing and the real data of 2011 200 GeV AuAu are compared in Figure 64. The smeared J/ψ signals are drawn in blue histograms, the J/ψ signals from real data reconstruction are drawn in red solid circles. The Upsilon templates will be obtained from the smearing with same smearing parameters from this J/ψ signals study.

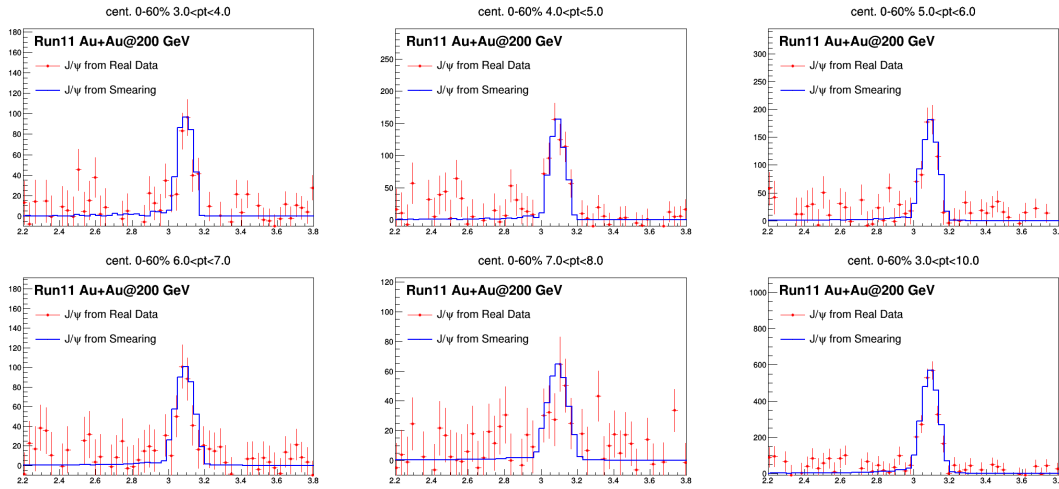


Figure 64: Comparison of smeared J/ψ to real data in Run11 200 GeV AuAu data.

4.2.3 Upsilon Reconstruction Efficiency

The Upsilon efficiency is calculated in different centrality and different p_T bins. The Upsilon reconstruction efficiency in different centrality bins for rapidity integrated within $|y| < 1$ and p_T integrated over $0 < p_T < 10$ GeV/c. are listed in Table XX. The Upsilon reconstruction

efficiency in different p_T bins with centrality integrated within 0-60% and rapidity integrated within $|y| < 0.5$ are listed in Table XXI.

Centrality	$\Upsilon(1S)$	$\Upsilon(2S)$	$\Upsilon(3S)$
0-10%	0.0383 ± 0.0006	0.0492 ± 0.0007	0.0510 ± 0.0007
10-30%	0.0469 ± 0.0006	0.0593 ± 0.0007	0.0649 ± 0.0007
30-60%	0.0610 ± 0.0011	0.0753 ± 0.0012	0.0822 ± 0.0013
0-60%	0.0425 ± 0.0004	0.0541 ± 0.0005	0.0576 ± 0.0005

TABLE XX: The reconstruction efficiency of $\Upsilon(1S)$, $\Upsilon(2S)$, $\Upsilon(3S)$ in centrality bins of 0-10%, 10-30%, 30-60% and 0-60%. For rapidity integrated within $|y| < 1$ and p_T integrated over $0 < p_T < 10$ GeV/c.

p_T range	$\Upsilon(1S)$	$\Upsilon(2S)$	$\Upsilon(3S)$
$0 < p_T < 2$ GeV/c	0.0398 ± 0.0007	0.0521 ± 0.0008	0.0550 ± 0.0008
$2 < p_T < 4$ GeV/c	0.0457 ± 0.0007	0.0585 ± 0.0008	0.0616 ± 0.0008
$4 < p_T < 10$ GeV/c	0.0438 ± 0.0006	0.0521 ± 0.0006	0.0567 ± 0.0007

TABLE XXI: The reconstruction efficiency of $\Upsilon(1S)$, $\Upsilon(2S)$, $\Upsilon(3S)$ in different p_T bins. For rapidity integrated within $|y| < 1$ and centrality integrated over 0-60%.

4.2.4 Upsilon Templates from Smearing

The momentum resolution parameters are tuned so that we can successfully smear the J/ψ to match real data, then we perform the smearing with the same parameters to get the smeared

Υ templates for Run11 AuAu. From the J/ψ signal fittings, we know, the tuning parameters can be obtained separately for each centrality bins: 0-10%, 10-30%, 30-60% and 0-60%. The smeared Upsilon signals templates are shown in Figure 65.

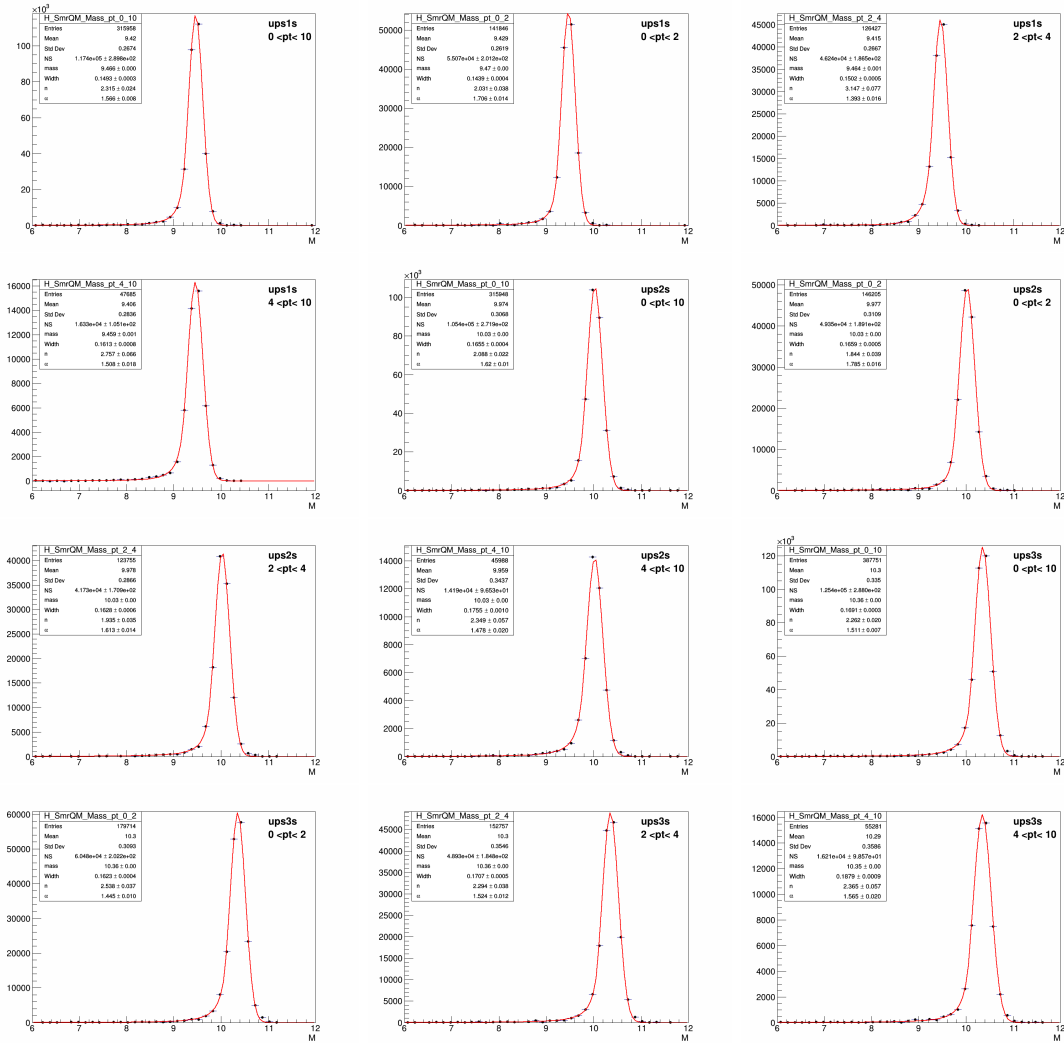


Figure 65: $\Upsilon(1S)$, $\Upsilon(2S)$, $\Upsilon(3S)$ templates for 0-60% centrality of Run11 AuAu

4.2.5 Physics background shapes of $B\bar{B}$ and Drell-Yan from simulation

The background from $B\bar{B}$ decays and Drell-Yan process are studied by the Pythia6 simulation with all the efficiencies of single electron embedded. The PYTHIA settings are from PHENIX tuning which could successfully describe the $B\bar{B}$ and DY shapes measured in 200 GeV p+p collisions [74]. Figure 66 show the invariant mass distributions of unlike-sign electron pairs from $B\bar{B}$ and Drell-Yan, and these histograms are used as the physics background templates in the fitting of Υ signals for Run11 AuAu.

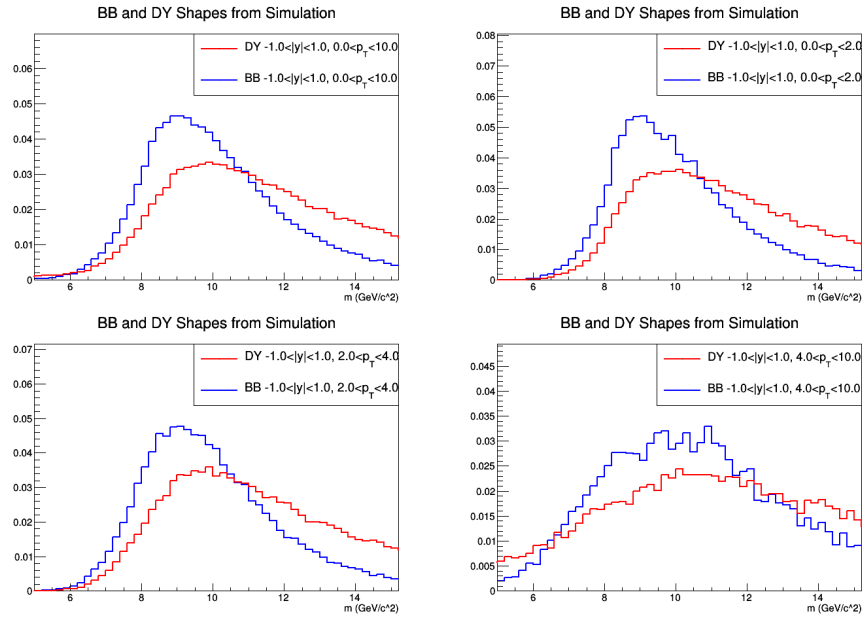


Figure 66: Background shapes of $B\bar{B}$ and Drell-Yan from PYTHIA simulation with all efficiency of single electron embedded.

4.3 How to Extract the Upsilon Signal Yields

4.3.1 Fitting Methods

The HFT detector was not installed in Run11 AuAu, thus the momentum resolution in Run11 AuAu is much better than that in Run15 pp and pAu, allowing a separation of the excited states ($\Upsilon(2S)$ and $\Upsilon(3S)$) from the ground state ($\Upsilon(1S)$). For the fitting of Upsilon signals in Run11 AuAu, the excited states are combined together as one signal $\Upsilon(2S3S)$. The combined pdf for $\Upsilon(2S3S)$ can be constructed from $\Upsilon(2S)$ and $\Upsilon(3S)$ pdf while weighted by their detection efficiency and the world wide experimental average ratios of $\Upsilon(2S) : \Upsilon(3S) = 0.275 : 0.128$ from PDG [20].

The fitting function is constructed as:

$$\begin{aligned}
 f_{\text{total}} = & \text{Yield}(1S) * \epsilon(1S) * \text{pdf}(1S) + \text{Yield}(2S3S) * \epsilon(2S3S) * [c_2 * \text{pdf}(2S) + c_3 * \text{pdf}(3S)] \\
 & + \text{Yield}(BB) * \epsilon(BB) * \text{pdf}(BB) + \text{Yield}(DY) * \epsilon(DY) * \text{pdf}(DY)
 \end{aligned}
 \tag{4.1}$$

Where:

- Yield is the efficiency corrected yield.
- ϵ is the detection efficiency.
- c_i is the constant of $\frac{\text{Yield}(iS)}{\text{Yield}(2S3S)} * \frac{\epsilon(iS)}{\epsilon(2S3S)}$, $i = 2, 3$.

In the fitting, pdf(1S), pdf(2S), pdf(3S), BB, DY shapes are fixed from the simulation, only Yield(1S) * $\epsilon(1S)$, Yield(2S3S) * $\epsilon(2S3S)$, Yield(BB) * $\epsilon(BB)$ and Yield(DY) * $\epsilon(DY)$ are

free parameters (Raw Yields) which will be obtained by fitting to the invariant mass spectrum (Unlike Sign - Like Sign) in real data.

4.4 Number of Equivalent MB Events

The monitoring MB events trigger corresponding to NPE18 trigger is called “zdc-ht-mon”, which has exactly the same definition of NPE18 trigger but without the BHT trigger requirement. The number of equivalent MB events can be estimated corresponding to the “zdc-ht-mon” trigger.

$$N_{MB}^{eqv.}(online) = \sum_{irun} [N_{ZDCMB}^{recorded}(|V_z| < 30) \frac{LIVETIME_{BHT2} PS_{ZDCMB}}{LIVETIME_{ZDCMB} PS_{BHT2}}](irun) \quad (4.2)$$

Where:

- “PS” is the pre-scale of a trigger which tells among how many triggered events one triggered event is recorded.
- “LIVETIME” is live (active) time of a trigger.

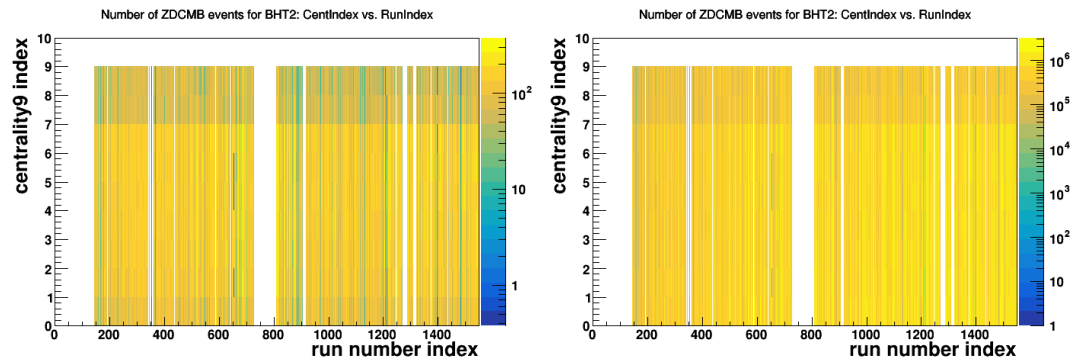


Figure 67: The centralities versus the number of ZDC MB events corresponding to the NPE18 triggered events in each run, before (left panel) and after (right panel) the pre-scale and live time correction.

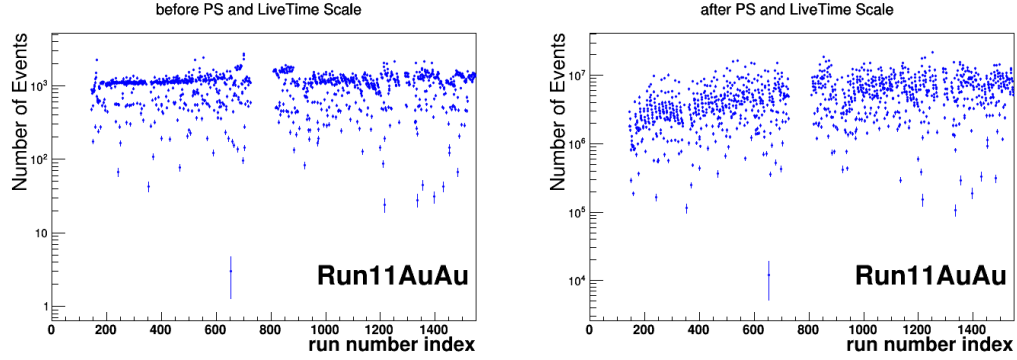


Figure 68: The number of ZDC MB events corresponding to the NPE18 triggered events in each run, before (left panel) and after (right panel) the pre-scale and live time correction, for all centralities.

The centrality index with the run number index 2-dimensional figures are shown in Figure 67, the left figure is before the trigger pre-scale and live time correction while the right figure is after the trigger pre-scale and live time correction. The two figures in Figure 68 is the x-projection of Figure 67 for all centralities. After sum the equivalent MB events over all runs in Figure 68, we could obtain the total number equivalent of MB events for all centralities. When we project the right figure of Figure 67 into x-axis for centralities: 0-10%, 10-30%, 30-60%, 0-60% separately, and then sum over all runs, we can also obtain the number of equivalent MB events for these centrality bins separately, these numbers are listed in Table XXII.

Centrality	0-10%	10-30%	30-60%	0-60%
$N_{MB}^{eqv. goodvtx} (M)$	700.88	1523	2310	4534

TABLE XXII: The number of equivalent MB events corresponding to the analyzed NPE18 triggered events in 2011 Au+Au collisions at $\sqrt{s_{NN}} = 200$ GeV.

4.5 Upsilon Signals from Fitting

In this analysis, Upsilon are measured in different centrality bins and different p_T bins. Figure 69 shows the Upsilon invariant mass including the signal fittings in different centrality bins: 0-60%, 30-60%, 10-30%, 0-10% for p_T integrated over $0 < p_T < 10$ and rapidity integrated over $|y| < 1$. Figure 70 shows the Upsilon invariant mass including the signal fittings in different p_T bins: $0 < p_T < 10$, $0 < p_T < 2$, $2 < p_T < 4$, $4 < p_T < 10$ GeV/c for centrality integrated over 0-60% and rapidity integrated over $|y| < 1$.

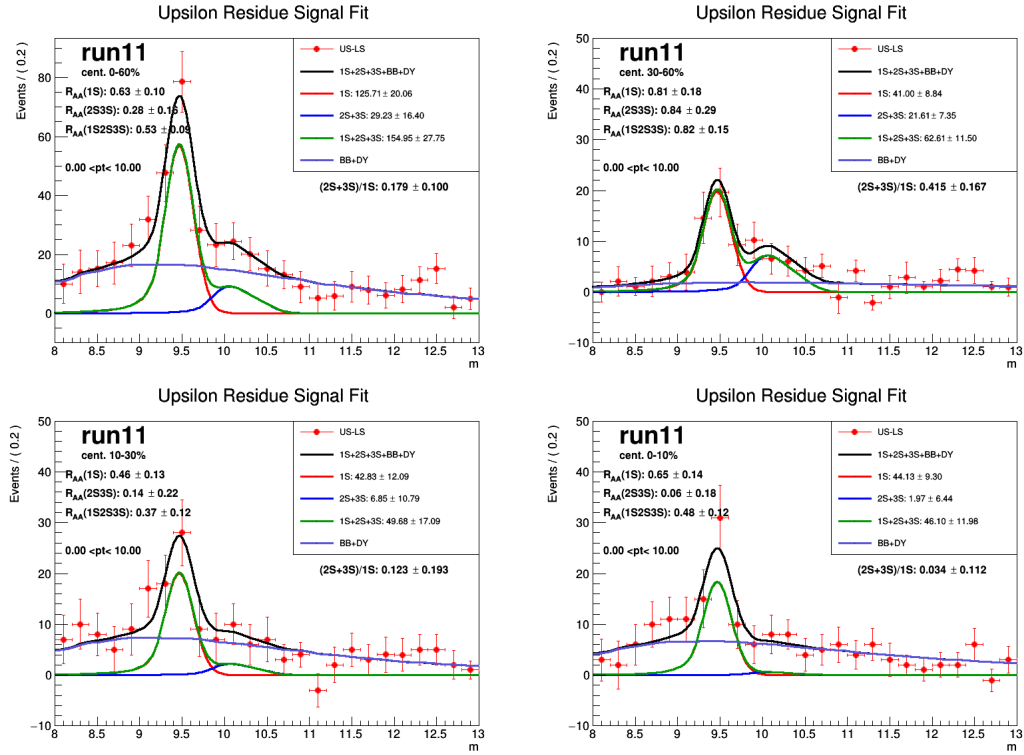


Figure 69: The invariant mass distribution of reconstructed Υ candidates, unlike-sign electron pairs (US) subtracted by like-sign electron pairs (LS), in different centrality bins of 0-60%, 30-60%, 10-30%, 0-10% with p_T integrated over $0 < p_T < 10$ and rapidity integrated over $|y| < 1$ in 2011 Au+Au collisions at $\sqrt{s_{NN}} = 200$ GeV.

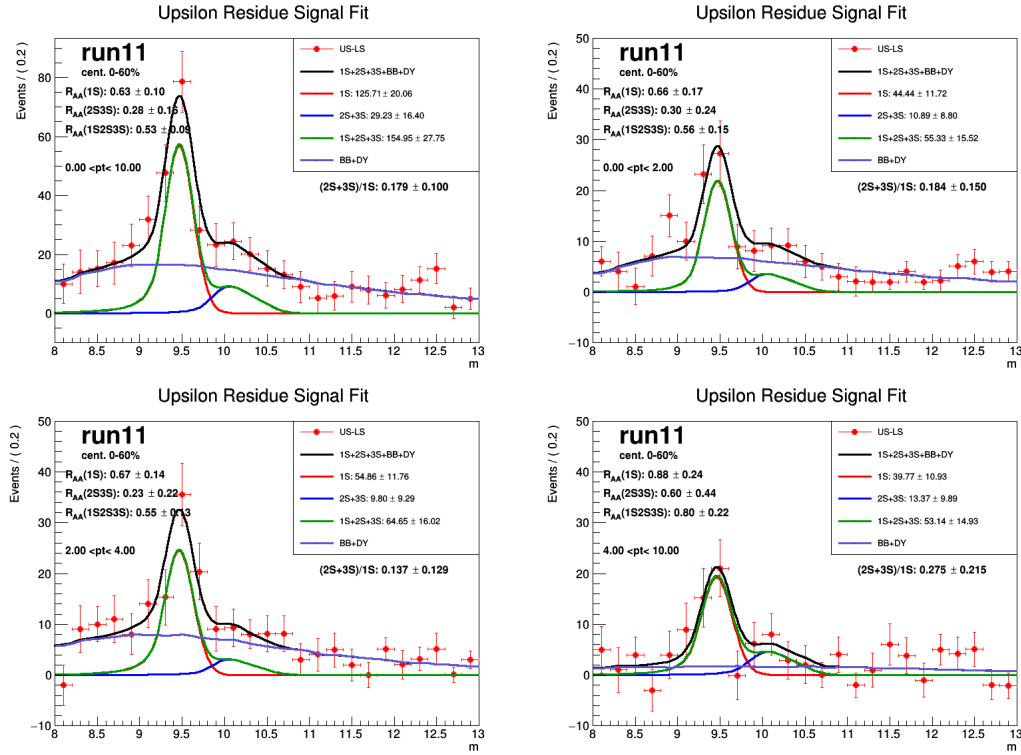


Figure 70: The invariant mass distribution of reconstructed Υ candidates, unlike-sign electron pairs (US) subtracted by like-sign electron pairs (LS), in different p_T bins: $0 < p_T < 10$, $0 < p_T < 2$, $2 < p_T < 4$, $4 < p_T < 10$ GeV/c with centrality integrated over 0-60% and rapidity integrated over $|y| < 1$ in 2011 Au+Au collisions at $\sqrt{s_{NN}} = 200$ GeV.

4.6 Systematic Uncertainties of Υ Measurements in Run11 AuAu

The systematic uncertainties of Υ invariant yield measurements in Run11 AuAu are obtained in different sources as follows:

- Fitting Ranges: the default fitting range is 8.0-13.0 GeV/c^2 , the fitting ranges are changed to 7.6-13.0, 8.4-13.0, 8.0-12.6, 8.0-13.4, 7.8-13.2 GeV/c^2 and obtain cross-sections, take the maximum difference relative to default cross-section as the systematic uncertainty from the fitting range.
- Binning Width: the default bin width is 0.2 GeV/c^2 , changed to 0.15 GeV/c^2 and 0.25 GeV/c^2 , take the maximum difference relative to default cross-section as the systematic uncertainty from the binning width.
- Υ Templates: The default template Width and the Shift factor are obtained from the fitting of smeared signals. The smeared template rely on the fitted width and mean of real J/ψ , so the width and mean of Υ templates are varied to cover the fitted statistical uncertainty of J/ψ mean and width. The widths of Υ templates are changed by $\pm 5\%$, and the shift of the mean of Υ templates are changed $\pm 10\%$.
- $B\bar{B}$ (BB) and Drell-Yan (DY) Templates: The BB and DY shapes are from the PYTHIA simulation with the detector efficiency embedded. The default PYTHIA settings in this analysis for the BB and DY simulation are from the PHENIX tuned settings which could well describe the measured BB and DY production at RHIC energy. There is another PYTHIA settings tuned to match results of di-lepton analysis. We take the difference of our physics results based on BB and DY shaped from this two PYTHIA settings as a systematic uncertainty of BB and DY shapes.
- $B\bar{B}$ shapes (de-correlated): As $B\bar{B}$ pairs are produced at the initial hard scattering, the b quarks are always generated at the same time and flying away in opposing directions.

The long life time of them allows they experience the entire evolution of the medium. However the modification on their kinematics due to the interactions with medium is still unknown. In our study, the default $B\bar{B}$ shapes are obtained while ignoring these modification effects. For the systematic uncertainty estimation, we take another extreme case that the correlation of these b hadrons are totally destroyed by the interactions with medium.

- $\Upsilon(1S):\Upsilon(2S):\Upsilon(3S)$ relative ratio: The default value of these relative ratios between each Υ state are from the world wide average value (1:0.275:0.128) for both Run15pp and Run15pAu, the ratios are changed to (1:0.275:0) for systematic uncertainty.
- Tracking “nHitsFits” Cuts: The default cuts of “nHitsFits ≥ 20 ”, this cut is changed to “nHitsFits ≥ 25 ” for the systematic uncertainty calculation.
- Dca cut: the default cut is “dca > 1.5 cm”, the cuts are changed to “dca > 1.25 cm” and “dca > 1.75 cm” for the systematic uncertainty calculation.
- Trigger Threshold Adc0 cut: the default Adc0 cut is “Adc0 ≥ 300 ”, the cut is changed to “Adc0 ≥ 303 ” for the systematic uncertainty calculation.
- E/p cut: the default cut is “ $0.3 < E/p < 1.8$ ”, the cut is changed to “ $0.4 < E/p < 1.7$ ” and “ $0.2 < E/p < 1.9$ ” systematic uncertainty calculation.
- BEMC matching “zDist and phiDist” cut: the default cut is “|zDist| < 10 and |phiDist| < 0.1 ”, these cuts are changed to “|zDist| < 11 and |phiDist| < 0.11 ” and “|zDist| < 9 and |phiDist| < 0.09 ” for systematic uncertainty calculation.

- Υ p_T curve parameter “T” value: The default value of T is 1.127 is obtained from the fitting of previous STAR Upsilon measurement [48], and this value is changed to 1.1 and 1.3 for systematic uncertainty calculation.

The other common systematic uncertainties:

- Acceptance: +1.7%, -3.0% cited from the previous Upsilon measurement [47].
- $n\sigma_e$: $\pm 4\%$ cited from the dielectron analysis with Run11 AuAu MB data [77]

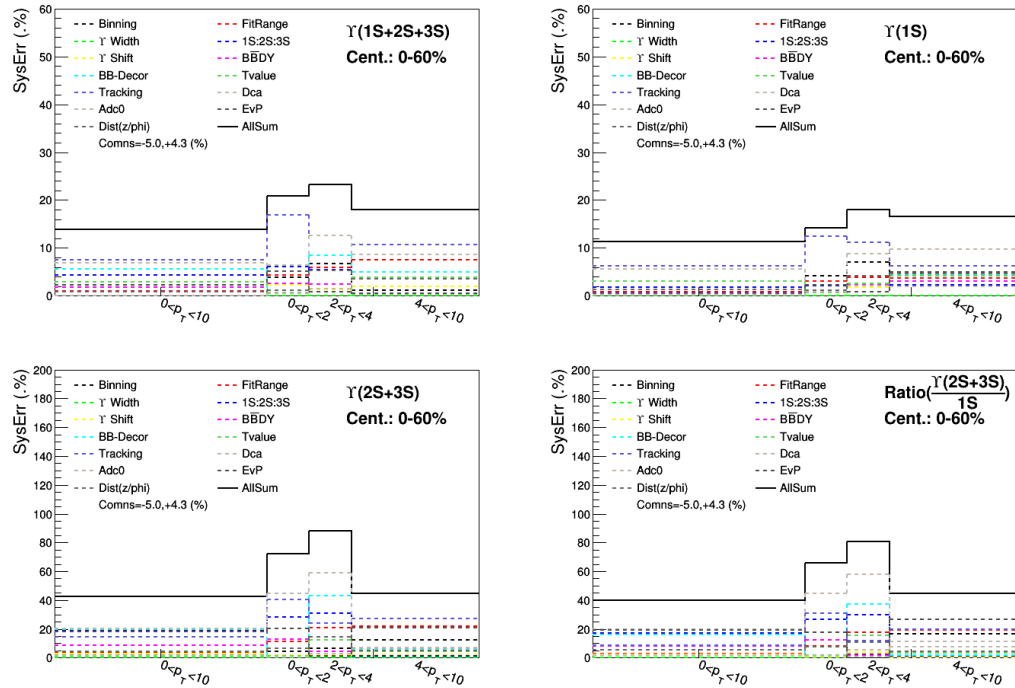


Figure 71: Systematic uncertainties from different sources for the invariant yields of $\Upsilon(1S+2S+3S)$, $\Upsilon(1S)$, $\Upsilon(2S+3S)$ and the Ratio of $\frac{2S+3S}{1S}$ as a function of p_T in 0-60% centrality within rapidity ranges: $|y| < 1$ in 2011 Au+Au collisions

4.6.1 Systematic Uncertainties of Υ R_{AA} Measurements

The R_{AA} is calculated based on the Υ cross-section measurements from Run15 pp and the invariant yield measurements from Run11 AuAu, thus the systematic uncertainties for the R_{AA} are contributed from both of this two measurements.

The systematic uncertainty of R_{AA} can be separated into two parts:

1. Common normalization uncertainty(those uncertainties which will move the values of R_{AA} in each centrality bin or p_T bin up or down synchronously):

- from the systematic uncertainty of Run15 pp:

$$\sigma_{NSD} = 30 \pm 2.4 \text{ mb}$$

$$\text{TrigBias(pp)} = 0.4800 \pm 0.0144$$

- from the systematic uncertainty of Run11 AuAu:

$$n\sigma_e: \pm 4\% \text{ cited from the dielectron analysis with Run11 AuAu MB data}$$

The uncertainty from the average number of binary collision N_{coll} for each centrality in Glauber Model simulation

2. Uncertainties for each individual R_{AA} data points:

- Uncorrelated uncertainties sources:

$$\text{ErrorSum}_{\text{uncorr}} = \sqrt{\sum_{pp, AuAu} \sum_{\text{isource}} \sigma_{\text{isource}}^2}$$

, `isource` = “Binning”, “FitRange”, “Upsilon Templates,” “Upsilon 1S,2S,3S relative ratio”, “BB,DY Templates”, “Upsilon p_T curve parameter T value” in Run15pp; and “Binning”, “FitRange”, “Upsilon Templates,” “Upsilon 1S,2S,3S relative ratio”, “BB,DY shapes from different PYTHIA settings”, “de-correlated BB shapes”, “Upsilon p_T curve parameter T value” in Run11AuAu.

- Correlated uncertainties:

$$\text{ErrorSum}_{\text{corr}} = \sqrt{\sum_{\text{isource}} (\sigma_{\text{isource}}^{\text{AuAu}} - \sigma_{\text{isource}}^{\text{pp}})^2}$$

, `isource` = “Tracking”, “Dca”, “E/p”, “zDist”, “phiDist”, “Adc0” cuts.

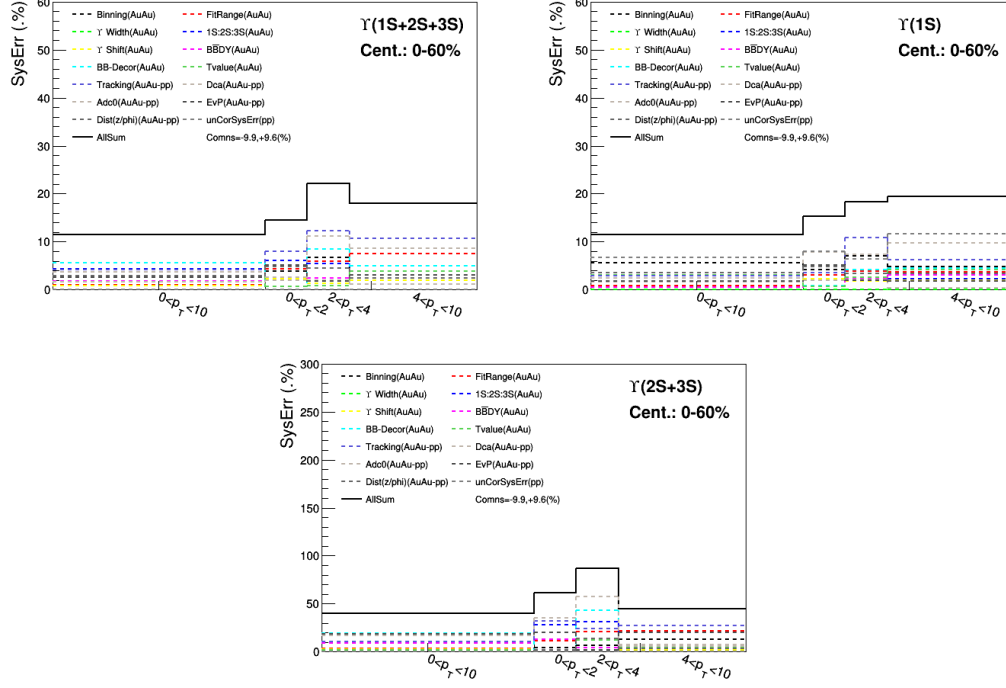


Figure 72: Systematic uncertainties from different sources for R_{AA} of $\Upsilon(1S+2S+3S)$, $\Upsilon(1S)$, $\Upsilon(2S+3S)$ as a function of p_T in 0-60% centrality within rapidity ranges: $|y| < 1$ from 2011 Au+Au collisions and 2015 p+p collisions

The systematic uncertainty coming from the average number of binary collisions $\langle N_{coll} \rangle$, which is not shown in the above figures, are drawn around the data points in a separate box as shown in the next section.

4.7 Physics Results

The invariant yield of Upsilon can be obtained by the following formula:

$$\text{Inv.Yield}(\Upsilon) = \frac{1}{N_{MB}^{\text{eqv.}} \epsilon_{MB}^{\text{goodvtx}}} * \frac{N_{\Upsilon}^{\text{raw}}}{\text{Acc.} \times \epsilon^{\text{Trig}} \epsilon^{\text{trk}} \epsilon^{\text{eID}}} * \frac{\epsilon_{MB}^{\text{ZDC}} \epsilon_{MB}^{\text{goodvtx}}}{\epsilon_{\Upsilon}^{\text{ZDC}} \epsilon_{\Upsilon}^{\text{goodvtx}}} \quad (4.3)$$

Here, the above equation is basically same as what we used for the invariant yield calculation Upsilon in p+Au calculation or identical to the cross section calculation in p+p collisions. However, a much larger multiplicity in the Au+Au collisions makes differences of ZDC coincidence and the good vertex efficiency between Upsilon events and normal MB events can be negligible, thus $\epsilon_{\Upsilon}^{\text{ZDC}} = \epsilon_{\text{MB}}^{\text{ZDC}}$, and with the same reason, the good vertex efficiency in Au+Au is 1.

$$\text{Inv.Yield}(\Upsilon) = \frac{1}{N_{\text{MB}}^{\text{eqv.}} \epsilon_{\text{MB}}^{\text{goodvtx}}} * \frac{N_{\Upsilon}^{\text{raw}}}{\text{Acc.} \times \epsilon^{\text{Trig}} \epsilon^{\text{trk}} \epsilon^{\text{eID}}} \quad (4.4)$$

The nuclear modification factor R_{AA} is defined as follows:

$$R_{\text{AA}} = \frac{\text{Inv.Yield}_{\text{AA}}^{(\Upsilon)}}{\sigma_{\text{pp}}^{(\Upsilon)}} * \frac{\sigma_{\text{pp}}^{\text{inel.}}}{\langle N_{\text{coll}}^{\text{AA}} \rangle} \quad (4.5)$$

Note that:

- $N_{\text{MB}}^{\text{eqv.}}$ is the number of equivalent ZDC MB events within $|V_z| < 30$ cm.
- $\epsilon_{\text{MB}}^{\text{goodvtx}}$ is the good vertex efficiency defined by the fraction of events within V_z satisfying the condition of “ $|V_z^{\text{TPC}} - V_z^{\text{VPD}}| < 3$ cm and $\sqrt{V_x^2 + V_y^2} < 2$ cm”.
- $\sigma_{\text{pp}}^{(\Upsilon)}$ is the Upsilon cross section measured in 2015 p+p collisions.
- $\sigma_{\text{pp}}^{\text{inel.}}$ is the inelastic cross section of p+p collisions.
- $\langle N_{\text{coll}}^{\text{AA}} \rangle$ is the average number of binary collisions in Au+Au collisions, as listed in Table XIX.

In this analysis, Upsilon is measured via $\Upsilon \rightarrow e^+e^-$ decay channel, the corresponding physics results are shown in section 4.7.1. Since the full installation of MTD at STAR in 2014, the di-muon trigger has collected large data sets in 2014 and 2016 Au+Au collisions at $\sqrt{s_{NN}} = 200$ GeV, with integrated luminosity of $\mathcal{L}_{2014} = 14.2 \text{ nb}^{-1}$ and $\mathcal{L}_{2016} = 12.8 \text{ nb}^{-1}$, respectively. The results of $R_{AA}^{\Upsilon(1S)}$ and the ratio $\frac{\Upsilon(2S+3S)}{\Upsilon(1S)}$ from this analysis (measured in $\Upsilon \rightarrow e^+e^-$ decay channel) and di-muon analysis (measured in $\Upsilon \rightarrow \mu^+\mu^-$ decay channel) are consistent with each other as shown in section 4.7.2, thus the results from these two analysis are combined together and the physics conclusions will be draw based on the combined results.

4.7.1 Physics Results Measured in $\Upsilon \rightarrow e^+e^-$ Decay Channel

The nuclear modification factor R_{AA} of $\Upsilon(1S)$, $\Upsilon(2S+3S)$, $\Upsilon(1S+2S+3S)$ and the ratio of excited Upsilon states $\Upsilon(2S+3S)$ over ground state $\Upsilon(1S)$ as a function of transverse momentum p_T are shown in Figure 73. The nuclear modification factor R_{AA} of $\Upsilon(1S)$, $\Upsilon(2S+3S)$, $\Upsilon(1S+2S+3S)$ and the ratio of excited Upsilon states $\Upsilon(2S+3S)$ over ground state $\Upsilon(1S)$ as a function of the average number participating nucleon N_{part} are shown in Figure 74. The comparison of Upsilon ground state and the excited states are shown in Figure 75, where the left panel shows the comparison of $R_{AA}^{\Upsilon(1S)}$ and $R_{AA}^{\Upsilon(2S+3S)}$ while the right panel shows the ratio $\frac{\Upsilon(2S+3S)}{\Upsilon(1S)}$ in different centralities (or N_{part}).

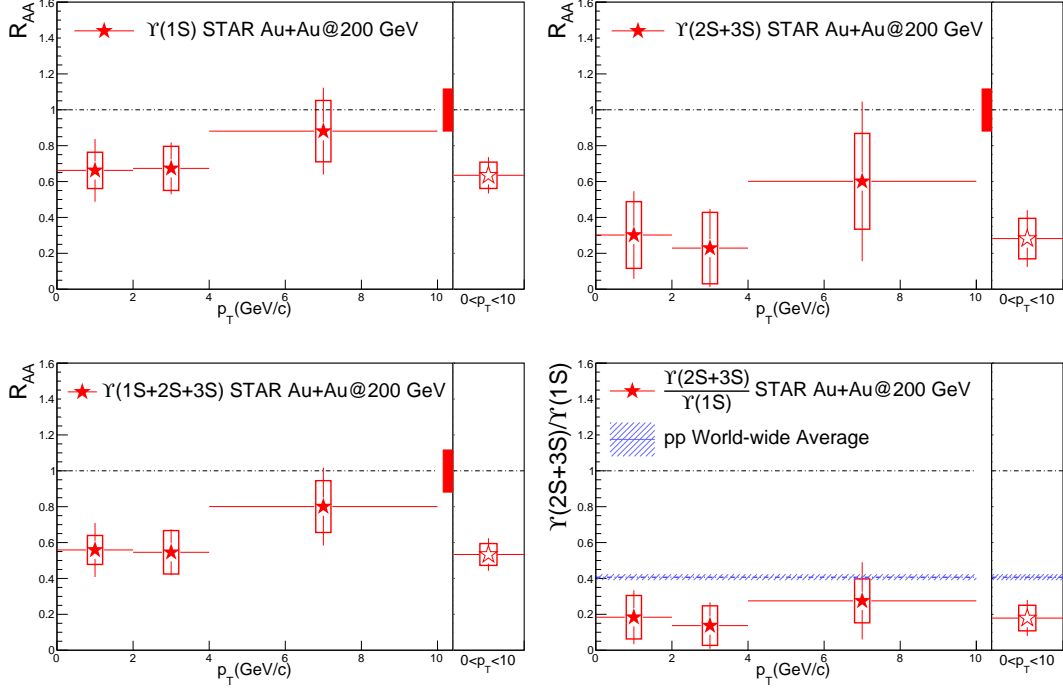


Figure 73: The nuclear modification factor R_{AA} of $\Upsilon(1S)$, $\Upsilon(2S+3S)$, $\Upsilon(1S+2S+3S)$ (the first 3 panels) and the ratio (the last panel) of excited Upsilon states over ground state as a function of p_T with rapidity integrated over $|y| < 1$ and centrality integrated over 0-60% are shown in red solid stars. The red open stars represent for the p_T integrated results. The vertical bar and the horizontal bar around each data point denote the bin width and statistical uncertainty of that point. The systematic uncertainties of each data point are drawn in red open boxes around the data points. The red solid box around the unity represents the common normalization uncertainty.

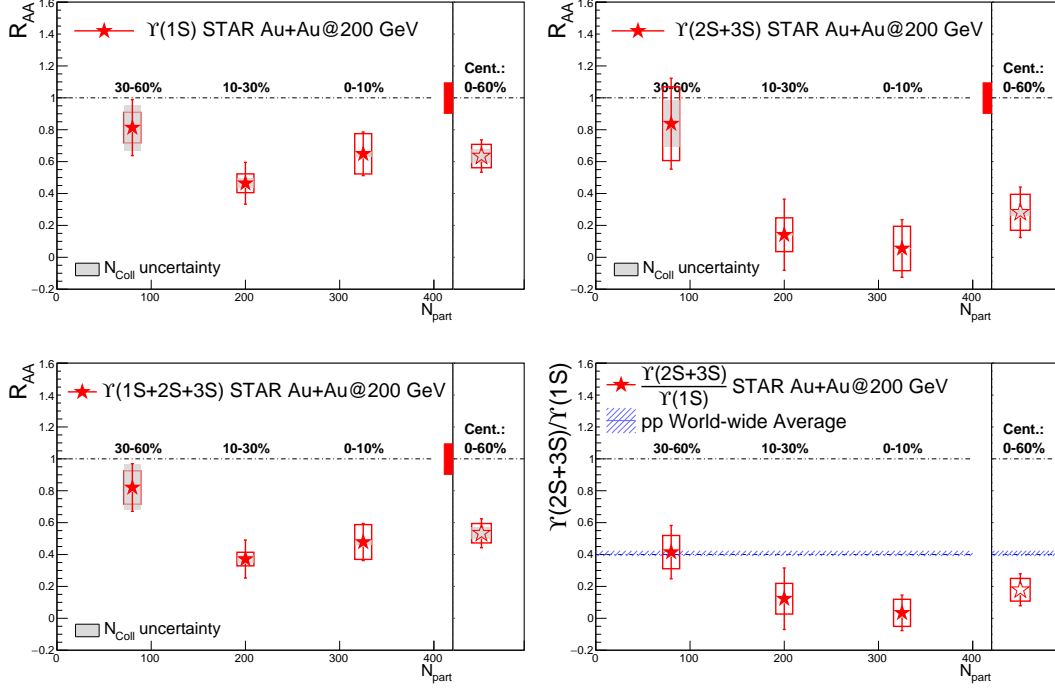


Figure 74: The nuclear modification factor R_{AA} of $\Upsilon(1S)$, $\Upsilon(2S+3S)$, $\Upsilon(1S+2S+3S)$ (the first 3 panels) and the ratio (the last panel) of excited Upsilon states over ground state as a function of N_{part} with rapidity integrated over $|y| < 1$ and p_T integrated over $0 < p_T < 10$ GeV/c are shown in red solid stars. The red open stars stand for the results of 0-60% centrality. The vertical bar around each data point represent the statistical uncertainty of that point. The systematic uncertainties of each data point are drawn in red open boxes around the data points, where the systematic uncertainty from N_{coll} is drawn separately in gray solid boxes. The red solid box around the unity represents the common normalization uncertainty.

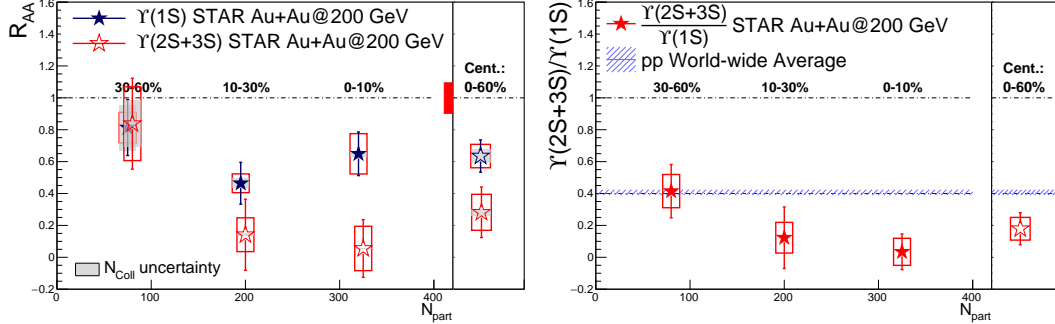


Figure 75: The comparison of Upsilon ground state and the excited states. The left panel is the R_{AA} of $\Upsilon(1S)$ and $\Upsilon(2S + 3S)$ as a function of N_{part} with rapidity integrated over $|y| < 1$ and centrality integrated over 0-60%. The right panel is ratio of $\Upsilon(2S + 3S)$ over $\Upsilon(1S)$ as a function of N_{part} with rapidity integrated over $|y| < 1$ and p_T integrated over $0 < p_T < 10$ GeV/c. The red open stars stand for the centrality integrated results. The vertical bar around each data point represent the statistical uncertainty of that point. The systematic uncertainties of each data point are drawn in red open boxes around the data points, where the systematic uncertainty from N_{coll} is drawn separately in grey solid boxes. The red solid box around the unity represents the common normalization uncertainty.

4.7.2 Cross-check between “di-electron” and “di-muon” analysis

The Υ production measurements in Au+Au collisions at $\sqrt{s_{NN}} = 200$ GeV with the STAR experiments are performed in both di-electron channel and di-muon channel. The comparison of R_{AA}^{1S} and ratio $\frac{\Upsilon(2S+3S)}{\Upsilon(1S)}$ between di-electron analysis and di-muon analysis are shown in Figure 76.

As one can see, results from di-muon and di-electron analysis are well consistent with each other within uncertainty, thus results from this two analysis are combined to improve the precision. (Note that, for the comparison of R_{AA} between the di-electron and and di-muon results, the reference of p+p measurement is the preliminary results listed in [78], while the results before this section are all corresponding to the new results after more efficiency corrected. As the reference only shift all the R_{AA} data points up $\sim 10\%$, it won't influence the physics conclusion, so it is not updated for now.)

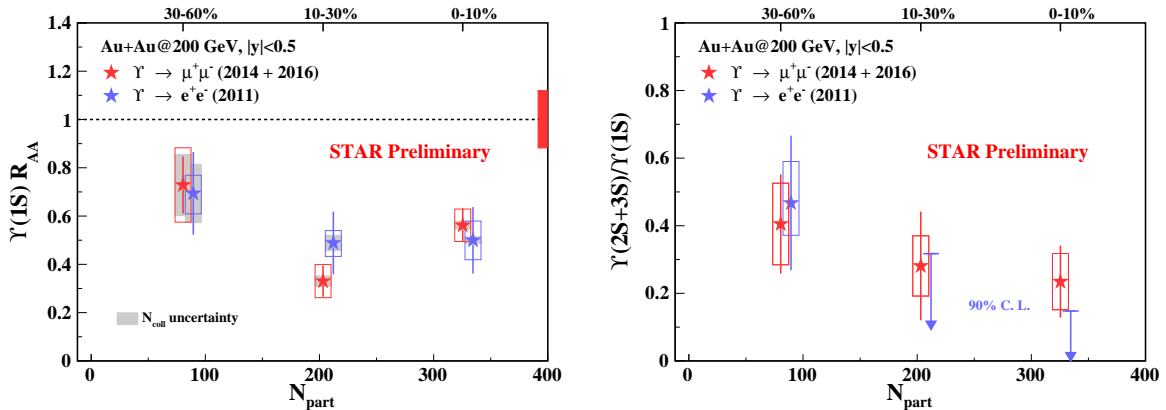


Figure 76: The left panel shows the comparison of R_{AA}^{1S} between di-electron (blue stars) and di-muon (red stars) analysis, the red solid box around unity line denotes the common normalization uncertainty. The right panel shows the comparison of ratio $\frac{Y(2S+3S)}{Y(1S)}$ between di-electron and di-muon analysis, the down arrows represent the upper limit with a confidence level of 90%. The open boxes around data points denote the systematic uncertainty and the gray solid boxes denote the systematic uncertainty coming from the $\langle N_{coll} \rangle$.

CHAPTER 5

PHYSICS RESULTS SUMMARY AND DISCUSSION

(PART OF RESULTS IN THIS CHAPTER WERE PREVIOUSLY PUBLISHED BY ZAOCHEN YE FOR STAR COLLABORATION, “ Υ MEASUREMENTS IN P+P, P+AU AND AU+AU COLLISIONS AT $\sqrt{s_{NN}} = 200$ GEV WITH THE STAR EXPERIMENT,” NUCL. PHYS. A 967, 600 (2017)), THESE RESULTS ARE ALSO PRESENTED IN OUR STAR COLLABORATOR-XINJIE HUANG AND WANGMEI ZHA’S SQM CONFERENCE PROCEEDINGS AT EPJ WEB OF CONFERENCES.

The final physics results in this thesis include the cross section of $\Upsilon(1S+2S+3S)$ production in p+p collisions, the invariant yield of $\Upsilon(1S+2S+3S)$ production in p+Au collisions, the nuclear modification factor of R_{pAu} and R_{AA} .

- The cross section of Υ in p+p collisions:

$$\sigma(\Upsilon) = \frac{\sigma_{pp}^{NSD}}{N_{MB}^{eqv.} \epsilon_{MB}^{goodvtx}} * \frac{N_{\Upsilon}^{raw}}{Acc. \times \epsilon^{Trig} \epsilon^{trk} \epsilon^{elD}} * TrigBias \quad (5.1)$$

- The invariant yield of Υ in p+Au collisions:

$$Inv.Yield(\Upsilon) = \frac{1}{N_{MB}^{eqv.} \epsilon_{MB}^{goodvtx}} * \frac{N_{\Upsilon}^{raw}}{Acc. \times \epsilon^{Trig} \epsilon^{trk} \epsilon^{elD}} * TrigBias \quad (5.2)$$

- The nuclear modification factor R_{pAu} of Υ :

$$R_{pA} = \frac{\text{Inv.Yield}_{pA}^{(\Upsilon)}}{\sigma_{pp}^{(\Upsilon)}} * \frac{\sigma_{pp}^{\text{inel.}}}{\langle N_{\text{coll}}^{pA} \rangle} \quad (5.3)$$

- The nuclear modification factor R_{AA} of Υ :

$$R_{AA} = \frac{\text{Inv.Yield}_{AA}^{(\Upsilon)}}{\sigma_{pp}^{(\Upsilon)}} * \frac{\sigma_{pp}^{\text{inel.}}}{\langle N_{\text{coll}}^{AA} \rangle} \quad (5.4)$$

5.1 Upsilon Cross section in p+p and Invariant Yield in p+Au

The new $\Upsilon(1S+2S+3S)$ cross section in 2015 p+p collisions at $\sqrt{s}=200$ GeV within a rapidity of $|\mathbf{y}| < 0.5$ and with \mathbf{p}_T integrated over $0 < \mathbf{p}_T < 10$ GeV/c is shown in red star in Figure 77, follows the world-wide experimental data trend predicted by the Next-to-Leading Order (NLO) Color Evaporation Model (CEM) calculation [79]. The new results is also consistent with the STAR published result [47] (open star) but with a factor of ~ 2 improvement on the precision.

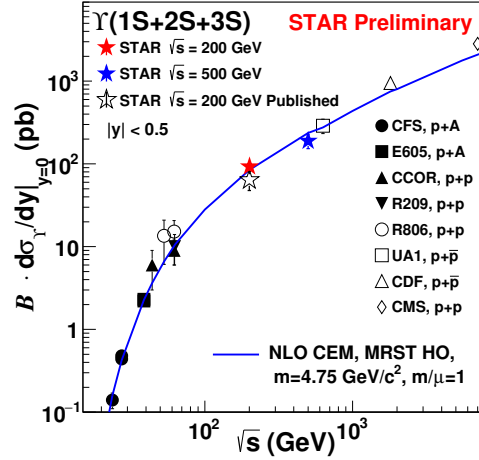


Figure 77: $\Upsilon(1S+2S+3S)$ cross section (red star) in 2015 p+p collisions at $\sqrt{s} = 200$ GeV is compared to STAR published result (open star), the preliminary result in p + p collisions (blue star) at $\sqrt{s} = 500$ GeV, the world-wide experimental data and the theoretical curve predicted by the NLO CEM calculator [79]. (The previous published data from STAR collaboration are also compared to the world-wide data in PHYSICAL REVIEW D 82, 012004 (2010). This figure is also shown in the previous publication by Xinjie Huang, on EPJ Web of Conferences 171, 18015 (2018))

The cross section as a function of transverse momentum p_T and rapidity y in p+p collisions at $\sqrt{s} = 200$ GeV are shown in Figure 78, where the results in rapidity ranges of $0.5 < y < 1.0$ and $-1.0 < y < -0.5$ combined as one point in $0.5 < |y| < 1$. The open circle in $-1.0 < y < -0.5$ is the mirror image point of $0.5 < |y| < 1$. The blue shaded bands are from the pQCD CEM calculations [79]. As one can see, our experimental data points are consistent with the pQCD CEM model calculations for both transverse momentum and rapidity dependence. The measurements of Υ production cross section in p+p collisions at $\sqrt{s} = 200$ GeV provide a precise base line for Υ suppression study in p+Au and Au+Au collisions at the same collision energy.

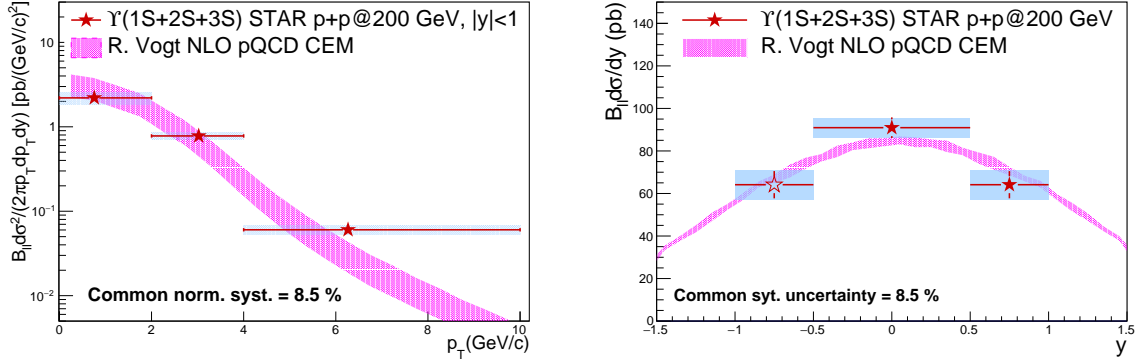


Figure 78: $\Upsilon(1S+2S+3S)$ cross section (red stars) as a function of transverse momentum (left) and rapidity (right) in 2015 p+p collisions at $\sqrt{s} = 200$ GeV are compared to the pQCD Color Evaporation Model (CEM) calculations (blue bands) [79]. The cross section of $\Upsilon(1S+2S+3S)$ as a function of p_T is measured within a rapidity range of $|y| < 1$. While the results in rapidity ranges of $0.5 < y < 1.0$ and $-1.0 < y < -0.5$ are combined as $0.5 < |y| < 1$, the open circle in $-1.0 < y < -0.5$ is the mirror image point of $0.5 < |y| < 1$. The vertical and horizontal bar around data points denotes the statistical uncertainty and the bin with, respectively. The azure boxes around data points represent the systematic uncertainty.

The invariant yield of $\Upsilon(1S+2S+3S)$ as a function of transverse momentum and rapidity in p+Au collisions $\sqrt{s_{NN}} = 200$ GeV are shown in Figure 79. At present, the direct theoretical calculations of Υ invariant yield or cross section in p+Au collisions is still omitted.

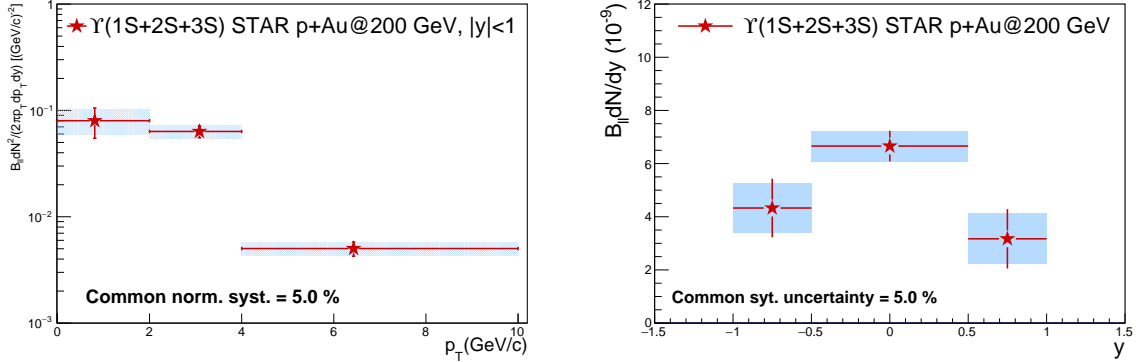


Figure 79: $\Upsilon(1S+2S+3S)$ invariant yield as a function of transverse momentum (left) and rapidity (right) in 2015 p+Au collisions at $\sqrt{s} = 200$ GeV are shown in red stars. The vertical and horizontal bar around data points denotes the statistical uncertainty and the bin width, respectively. The azure boxes around data points represent the systematic uncertainty.

5.1.1 Nuclear Modification Factor

The nuclear modification factor R_{pAu} of $\Upsilon(1S+2S+3S)$ as a function of transverse momentum and rapidity are shown in Figure 80. From the left panel, one can see that the $\Upsilon(1S+2S+3S)$ is significantly suppressed in p+Au collisions w.r.t that in p+p collisions and the suppression tends to be stronger towards the lower p_T . From the right panel of Figure 80, one can see that the suppression of $\Upsilon(1S+2S+3S)$ doesn't show a clear rapidity dependence within the measured narrow rapidity range of $|y| < 1$.

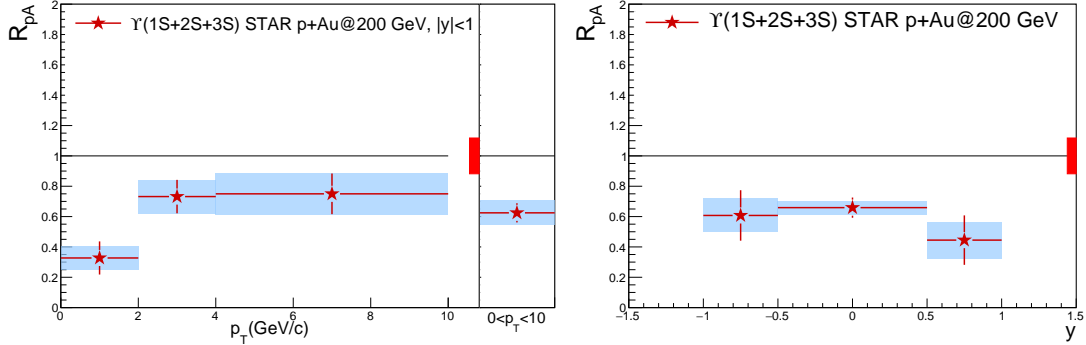


Figure 80: The nuclear modification factor R_{pAu} of $\gamma(1S+2S+3S)$ as a function of transverse momentum (left) and rapidity(right). The vertical and horizontal bar around data points denotes the statistical uncertainty and the bin with, respectively. The azure boxes around data points represent the systematic uncertainty. The red band on the right side around unity represents the common normalization uncertainties.

In Figure 81 our measurements are compared to the R_{pPb} of $\gamma(1S)$ from ATLAS experiment [80] measured in p+Pb collisions at $\sqrt{s_{NN}} = 5.02$ TeV within a rapidity range of $-2 < y < 1.5$. As one can see, the suppression of $\gamma(1S+2S+3S)$ at RHIC energy is similar as that at LHC energy, however at low p_T , the data tends to suggest a stronger suppression at RHIC than at LHC. The R_{pPb} of $\gamma(1S)$ was also measured by ALICE experiment at $\sqrt{s_{NN}} = 8.16$ TeV [81] with rapidity ranges of $-4.46 < y < -2.96$ and $2.03 < y < 3.53$ as shown in Figure 82. This comparison gives the similar conclusion as the comparison between STAR and ATLAS.

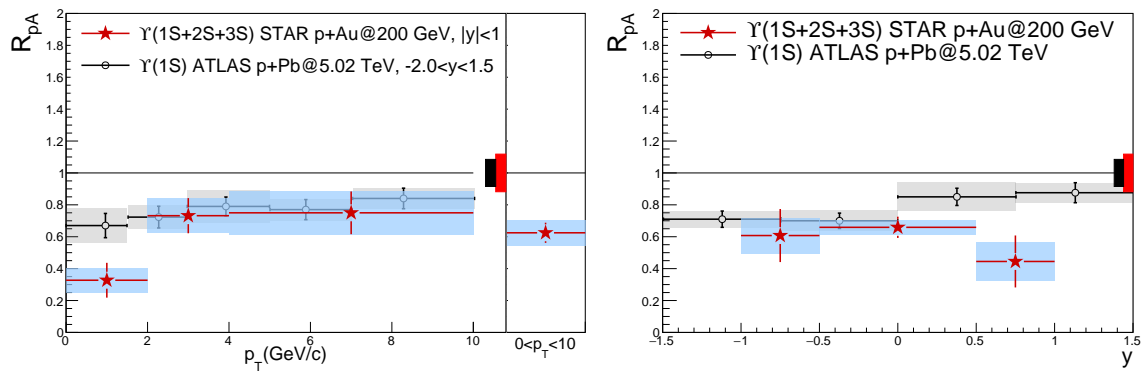


Figure 81: The R_{pAu} of $\Upsilon(1S+2S+3S)$ as a function of p_T and y from our measurements (red stars) are compared to results from ATLAS experiment [80] (open circles) measured in p+Pb collisions at $\sqrt{s_{NN}} = 5.02$ TeV within a rapidity range of $-2 < y < 1.5$. The boxes around data points represent the systematic uncertainty. The colored bands on the right side around unity represent the common normalization uncertainties.

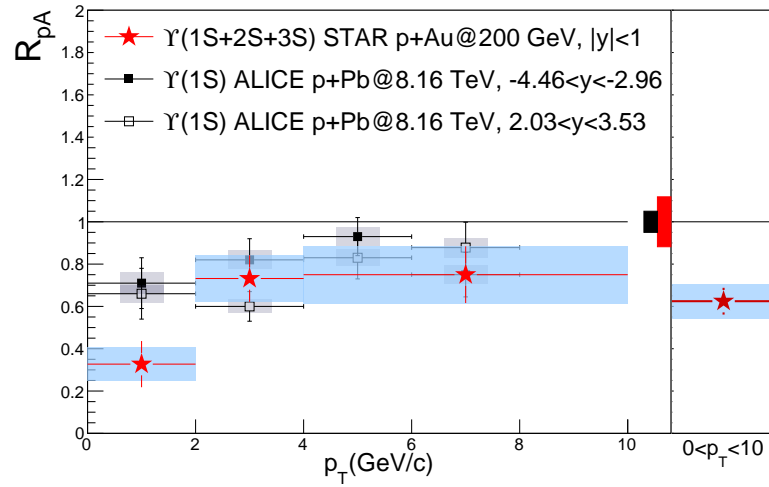


Figure 82: The cold nuclear modification factor R_{pA} of $\Upsilon(1S+2S+3S)$ as function of p_T from our measurements at 200 GeV are shown in red stars, and compared to results from ALICE experiment (filled squares for $-4.46 < y < -2.96$ and open squares for $2.03 < y < 3.53$) at $\sqrt{s_{NN}} = 8.16$ TeV [81], the shaded boxes around data points represent the systematic uncertainty. The colored bands on the right side around unity represent the common normalization uncertainties.

In Figure 83, our results are compared to the theoretical calculations. The blue hatched band is from the CEM calculations [79] based on the EPS09-nPDFs (the next-to-leading order nuclear parton distribution functions), where the band width is coming from the uncertainties of EPS09 parameterizations. This calculations predicts an enhancement with $R_{pAu} \sim 1.1$ at mid-rapidity mainly corresponding to the anti-shadowing effects. Recently, the TAMU model [82] extend their in-medium transport approach for the quarkonium production in nucleus-nucleus collisions to the proton-nucleus collisions. Besides the CNM effects from nPDFs, they also includes the nuclear absorption contribution with a absorption cross section of $\sigma_{abs.} = 0-3$ mb and the dissociation and regeneration within a rate-equation framework. The band width of their calculations is mainly coming from the EPS09-nPDFs parameterizations and the absorption cross section. Their prediction shows a better agreement with our experimental data although there is still clear difference at the low p_T .

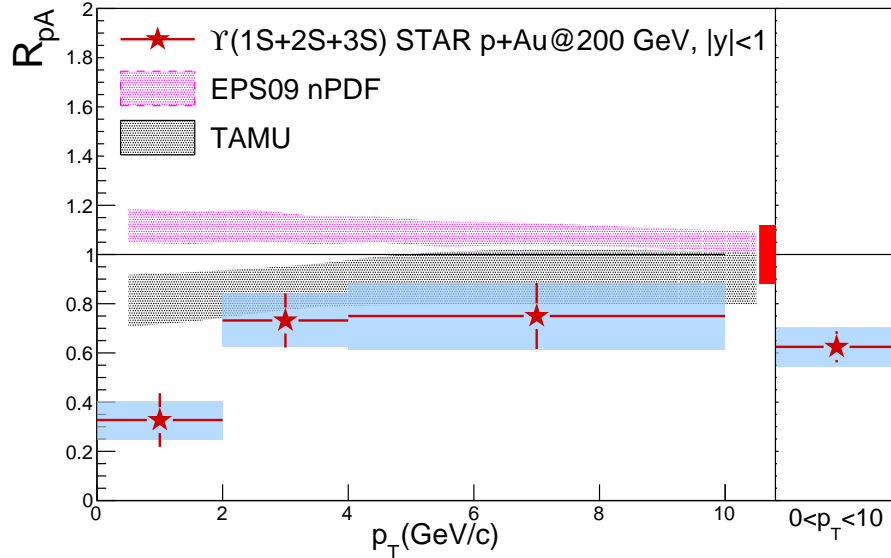


Figure 83: The new R_{pAu} (red stars) of $\Upsilon(1S+2S+3S)$ as a function of transverse momentum are compared to the theoretical prediction based on EPS09 nPDF done by R. Vogt [79] (blue shaded band) and the latest calculation from TAMU model [82] considering the nuclear absorption effects on top of nPDF effects (black shaded band). The statistical and systematic uncertainties are shown as vertical bars and shaded boxes respectively around the data points. The red band on the right side around unity represents the common normalization uncertainties.

In Figure 84, the R_{pAu} of $\Upsilon(1S+2S+3S)$ as a function of rapidity is compared to several theoretical predictions. The blue and black hatched bands are corresponding to the same calculations as described above. The gray dot-dashed line shows a calculation of R_{dAu} of $\Upsilon(1S+2S+3S)$ while combining the initial-state parton energy loss and the EPS09 nPDFs. In this model, the pre-bottomonia state of $b\bar{b}$ may lose energy through the gluo-bremsstrahlung radiation, while interacting with the cold nuclear matter in the nucleus, before they form a more stable bound state as a Υ meson. The energy loss of these $b\bar{b}$ will decrease their possibility

to form a Υ meson. This calculation is only valid for a rapidity range $y \gtrsim -1.2$ where the $b\bar{b}$ are close to the nucleus spectators. The red dot-dashed line represent predictions if only considering the energy loss contribution without the effects from EPS09 nPDFs. The comparison in Figure 83 and Figure 84, therefore, indicate that the model calculations only considering the nPDFs effect are disfavored by our experimental data, the additional cold nuclear matter effects (nuclear absorption...) are needed to be taken into account. Which is consistent with the observation of $J/\psi R_{pAu}$ in [83].

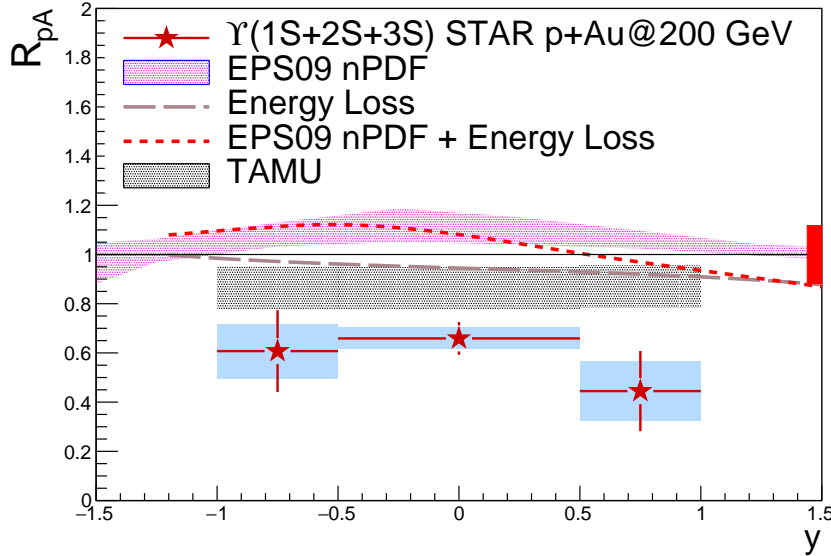


Figure 84: The new R_{pAu} (red stars) of $\Upsilon(1S+2S+3S)$ as a function of rapidity are compared to different theoretical model calculations. The blue hatched band shows predictions based on EPS09 nPDF done by R. Vogt [79]. Prediction only considering the initial-state energy loss effect is shown as a gray dashed line, while the prediction considering both initial-state energy loss and the EPS09 nPDF are shown as the red dot-dashed line [84]. The latest calculations from TAMU model [82] considering the nuclear absorption on top of nPDF effects is shown as black shaded band. The statistical and systematic uncertainties are shown as vertical bars and shaded boxes respectively around the data points. The colored band on the right side shows the common normalization uncertainties.

Figure 85 shows the R_{AA}^{1S} and R_{AA}^{2S+3S} as a function of N_{part} , combined from di-electron and di-muon channels, in Au+Au collisions at $\sqrt{s_{NN}} = 200$ GeV from the STAR experiment. As one can see, both $\Upsilon(1S)$ and $\Upsilon(2S+3S)$ shows a stronger suppression in semi-central and central collisions compared to the most peripheral collisions. Moreover, $\Upsilon(2S+3S)$ shows a similar

suppression as $\Upsilon(1S)$ at the peripheral collisions while a significant stronger suppression than $\Upsilon(1S)$ at the central collisions, which is consistent with the “sequential melting” expectation.

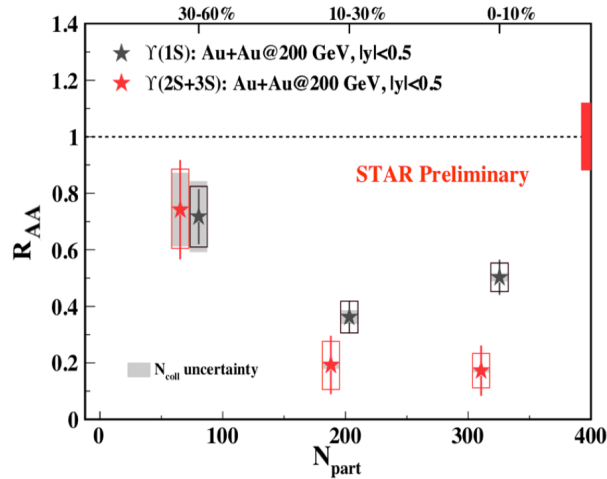


Figure 85: R_{AA}^{1S} (black stars) and R_{AA}^{2S+3S} (black stars) as a function of N_{part} , combined from di-electron and di-muon channels. The vertical bars shows the statistical uncertainty. The open boxes around data points shows the systematic uncertainty. The light gray bands represent the uncertainty from N_{coll} . The red band around unity on the right side shows the common normalization uncertainty from the Υ measurements in p+p collisions.

Our results are compared to the measurements from CMS experiment at LHC in Pb+Pb collision at $\sqrt{s_{NN}} = 2.76$ TeV [44] in Figure 86. In the left panel of Figure 86, the $\Upsilon(1S)$ shows a similar suppression at RHIC as at LHC. To interpret this observation, different factors need

to be considered carefully. As the collision energy at LHC is much higher than that at RHIC, the medium temperature at LHC should be higher than that at RHIC, which will lead to a higher dissociation rate of quarkonium at LHC than at RHIC. On the other hand, the bottom production rate is much higher at LHC than at RHIC, which results in a higher regeneration rate of quarkonium than at RHIC. There is a competition between the mechanisms of dissociation and regeneration here. Moreover, another factor also need to be considered is the feed-down contributions from the higher excited states. The fraction of high p_T $\Upsilon(1S)$ ($p_T > 8$ GeV/c) from feed-down contributions in p+p collisions at $\sqrt{s} = 1.8$ TeV, is measured to be $\sim 50\%$ by CDF experiment [85], and this fraction for all $\Upsilon(1S)$ from average experimental data is $\sim 33\%$ [86]. Since the measured $\Upsilon(1S)$ are the inclusive $\Upsilon(1S)$, the contribution from their feed-down source particles on the suppression of $\Upsilon(1S)$ need to be estimated while explaining the suppression of $\Upsilon(1S)$. The last factor need to be considered is the contribution from the CNM effects. As learned in the R_{pA} studies, the CNM effects on the Υ suppression are similar or slightly weaker at LHC than at RHIC. In the right panel, the $R_{AA}^{\Upsilon(2S+3S)}$ from STAR experiment are compared to $R_{AA}^{\Upsilon(2S)}$ and $R_{AA}^{\Upsilon(3S)}$ from CMS experiment. As the data shown, a similar suppression at semi-central and central collisions at RHIC and at LHC are observed, however at the peripheral collisions, there is an indication of less suppression at RHIC than at LHC.

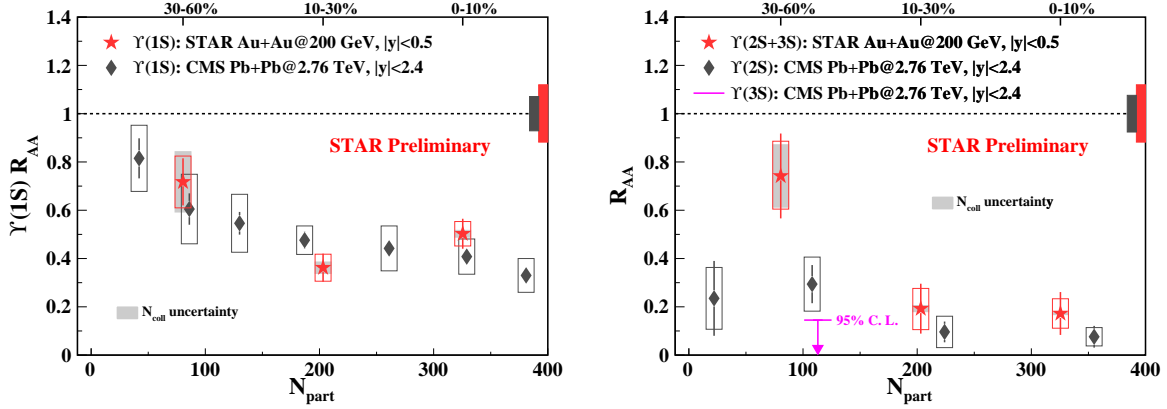


Figure 86: The left panel shows the comparison of R_{AA}^{1S} in Au+Au collisions at $\sqrt{s_{NN}} = 200$ GeV from STAR (red stars) and in Pb+Pb collision at $\sqrt{s_{NN}} = 2.76$ TeV from CMS [44] (black rhombus). The right panel shows the comparison of Υ excited states R_{AA} between STAR ($\Upsilon(2S+3S)$ shown in red stars) and CMS ($\Upsilon(2S)$ shown in black rhombus, $\Upsilon(3S)$ shown in down arrow denoting an upper limit with 95% C.L.). The vertical bars shows the statistical uncertainty. The open boxes around data points shows the systematic uncertainty. The light gray bands around STAR data points represent the uncertainty from N_{coll} . The colored bands around unity on the right side represent the common normalization uncertainty.

In Figure 87, our measured R_{AA}^{1S} and R_{AA}^{2S+3S} are also compared to the recent theoretical calculations. The first model is Rothkopf model, which used the lattice QCD vetted potential embedded in the hydro-dynamically evolving medium, assuming the initial temperature of QGP $T_0^{QGP} \simeq 439 - 442$ MeV and the melting temperatures for $\Upsilon(1S)$, $\Upsilon(2S)$, $\Upsilon(3S)$ are 600, 230,

170 MeV. The band width represents the uncertainty of this model calculations, which is mainly sourced from the potential parameterizations. This model did not consider the CNM or the regeneration effects in their calculations. The second model is the Rapp model, which introduce both quasi-free dissociation and gluo-dissociation mechanism in their calculations, and implied the binding energy predicted by the thermodynamic T-matrix calculations with the internal energy potentials. The model included the CNM effects and the regeneration effects in their calculations. The initial temperature of QGP $T_0^{\text{QGP}} = 313$ MeV, and the melting temperatures for $\Upsilon(1S)$, $\Upsilon(2S)$, $\Upsilon(3S)$ are 500, 240, 190 MeV. The main source for the theoretical band width of this model calculation is the CNM effects. From left panel of Figure 87, one can see both Rothkopf and Rapp model predictions are consistent with our data points within uncertainty. However, as shown in the right panel of Figure 87, Rothkopf model seems to underestimate the R_{AA}^{2S+3S} in the peripheral collisions while the Rapp model can well describe our data.

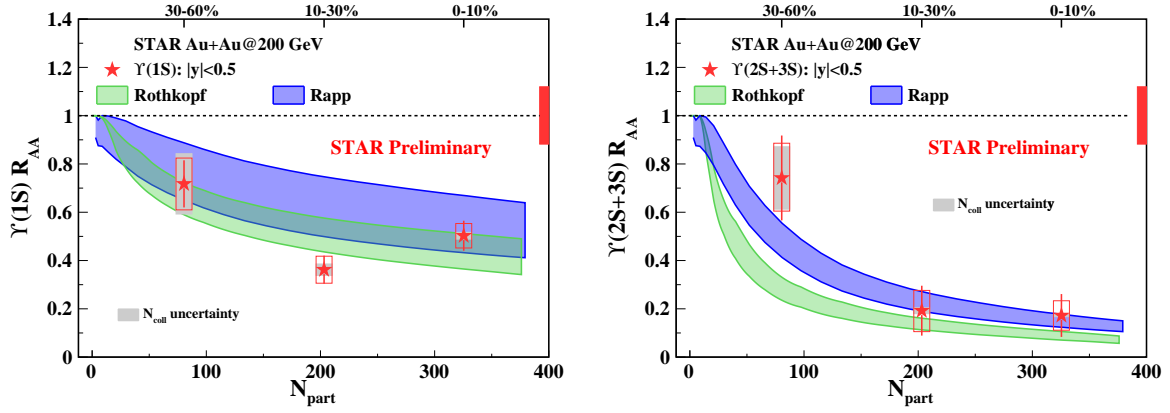


Figure 87: The R_{AA}^{1S} (left panel) and R_{AA}^{2S+3S} (right panel) from STAR measurements are compared to the Rothkopf Model [87] developed by Krouppa, Rothkopf and Strickland (green band), and to the Rapp Model [88] developed by Du, He and Rapp (blue band).

CHAPTER 6

CONCLUSIONS

In this thesis, we successfully measured the Υ productions via the $\Upsilon \rightarrow e^+e^-$ decay channel with the data taken in 2015 p+p collisions at $\sqrt{s} = 200$ GeV, 2015 p+Au collisions and 2011 Au+Au collisions at $\sqrt{s_{NN}} = 200$ GeV with the STAR experiment. In p+p collisions at $\sqrt{s} = 200$ GeV, we obtained the most precise measurement of $\Upsilon(1S+2S+3S)$ total production cross section at RHIC, which has a factor of 2 better precision than the previous published result. We also obtained the first differential production cross section of $\Upsilon(1S+2S+3S)$ as a function of transverse momentum p_T . The measured $\Upsilon(1S+2S+3S)$ cross section as a function of transverse momentum p_T and rapidity y are well consistent with the theoretical calculations from the NLO CEM model. The $\Upsilon(1S+2S+3S)$ measurements in p+p collisions provide a precise base line for the cold nuclear matter study in p+Au collisions and hot nuclear matter study in Au+Au collisions.

In p+Au collisions, we obtained the most precise cold nuclear modification factor R_{pAu} of $\Upsilon(1S+2S+3S)$ at RHIC. The R_{pAu} as a function of p_T and y are measured. A significant suppression of Υ production in p+Au collisions with respect to p+p collisions is observed, and the suppression tends to be stronger towards lower p_T but not clear rapidity dependence. The results are compared to the experimental results in p+Pb collisions at LHC energies. The $R_{pAu}^{1S+2S+3S}$ at RHIC shows a similar but slightly stronger suppression than the R_{pPb}^{1S} at LHC. The

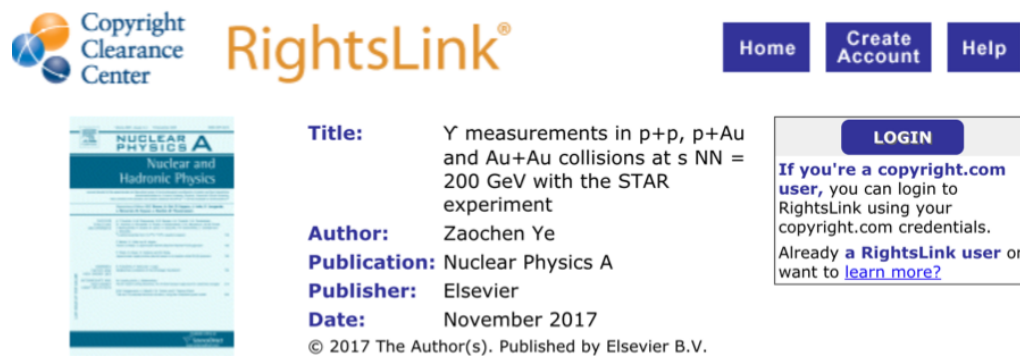
model calculations only considering the nPDFs and energy loss effects can not well describe our measured R_{pAu} data, additional CNM effects such as the nuclear absorption effect are favored.

In Au+Au collisions, the nuclear modification factor R_{AA} of $\Upsilon(2S+3S)$ and the R_{AA} as a function of p_T are measured for the first time at RHIC. As the results obtained from our analysis is consistent with that measured from the di-muon channel, the results from di-electron channel and di-muon channel are combined. The combined results of R_{AA}^{1S} and R_{AA}^{2S+3S} are the best results at RHIC. The $\Upsilon(2S+3S)$ shows a significant stronger suppression than the $\Upsilon(1S)$ in central collisions which is consistent with the “sequential melting” expectation. The $\Upsilon(1S)$ shows a similar suppression at RHIC and LHC while $\Upsilon(2S+3S)$ is less suppressed at RHIC than at LHC. The full understanding of this observation need to well consider the interplay cold and hot nuclear matter effects on the direct and feed-down contributions.

APPENDIX

COPYRIGHT POLICY

Figure 88 is the screen-shot of the online copyright statement of Nuclear Physics A for Zaochen's previous publication: " Υ measurements in p+p, p+Au and Au+Au collisions at $\sqrt{s_{NN}} = 200$ GeV with the STAR experiment", Nuclear Physics A, 967 (2017) 600-603). Figure 89 and Figure 90 is the screen-shot of online copyright statement of EPJ Web of Conferences for Xinjie Huang and Wangmei Zha's conference proceedings.



Copyright Clearance Center RightsLink[®] Home Create Account Help

Title: Υ measurements in p+p, p+Au and Au+Au collisions at $s_{NN} = 200$ GeV with the STAR experiment

Author: Zaochen Ye

Publication: Nuclear Physics A

Publisher: Elsevier

Date: November 2017

© 2017 The Author(s). Published by Elsevier B.V.

LOGIN

If you're a **copyright.com user**, you can login to RightsLink using your copyright.com credentials. Already a **RightsLink user** or want to [learn more?](#)

Please note that, as the author of this Elsevier article, you retain the right to include it in a thesis or dissertation, provided it is not published commercially. Permission is not required, but please ensure that you reference the journal as the original source. For more information on this and on your other retained rights, please visit: <https://www.elsevier.com/about/our-business/policies/copyright#Author-rights>

BACK

CLOSE WINDOW

Copyright © 2018 Copyright Clearance Center, Inc. All Rights Reserved. [Privacy statement](#). [Terms and Conditions](#).
Comments? We would like to hear from you. E-mail us at customercare@copyright.com

Figure 88: The screen-shot of the online copyright statement of Nuclear Physics A.

APPENDIX (Continued)

Open Access

Issue	EPJ Web Conf. Volume 171, 2018 17 th International Conference on Strangeness in Quark Matter (SQM 2017)
Article Number	18015
Number of page(s)	4
Section	Open and Hidden Heavy-Flavour (parallel session)
DOI	https://doi.org/10.1051/epjconf/201817118015
Published online	02 February 2018

EPJ Web of Conferences 171, 18015 (2018)
<https://doi.org/10.1051/epjconf/201817118015>

Quarkonium measurements in heavy-ion collisions with the STAR experiment

Xinjie Huang
 Tsinghua University, Beijing 100084, China

Published online: 2 February 2018

Abstract

In these proceedings, we present the latest measurements of J/ψ and Y by the STAR experiment. The J/ψ and Y production measured in p+p collisions provide new baselines for similar measurements in Au+Au collisions, while the measurements in p+Au collisions can help quantify the cold nuclear matter effects. The J/ψ v_2 is measured in both U+U and Au+Au collisions to place constraints on the amount of J/ψ arising from recombination of deconfined charm and anti-charm pairs. Furthermore, the nuclear modification factors for ground and excited Y states as a function of transverse momentum and centrality are presented, and compared to those measured at the LHC as well as to theoretical calculations.

© The Authors, published by EDP Sciences, 2018



This is an Open Access article distributed under the terms of the Creative Commons Attribution License 4.0, which permits unrestricted use, distribution, and reproduction in any medium, provided the original work is properly cited.

Figure 89: The screen-shot of the online copyright statement of EPJ Web of Conferences.

APPENDIX (Continued)

Open Access	
Issue	EPJ Web Conf. Volume 171, 2018 17 th International Conference on Strangeness in Quark Matter (SQM 2017)
Article Number	01004
Number of page(s)	8
Section	Highlights on Strangeness and Heavy-Flavour at Low pt
DOI	https://doi.org/10.1051/epjconf/201817101004
Published online	02 February 2018

EPJ Web of Conferences 171, 01004 (2018)
<https://doi.org/10.1051/epjconf/201817101004>

Recent highlights from STAR

Wangmei Zha*

Department of modern physics, University of Science and Technology of China, Hefei, 230026, China

* e-mail: wangmei@rcf.rhic.bnl.gov

Published online: 2 February 2018

Abstract

The Solenoidal Tracker at RHIC (STAR) experiment takes advantage of its excellent tracking and particle identification capabilities at mid-rapidity to explore the properties of strongly interacting QCD matter created in heavy-ion collisions at RHIC. The STAR collaboration presented 7 parallel and 2 plenary talks at Strangeness in Quark Matter 2017 and covered various topics including heavy flavor measurements, bulk observables, electro-magnetic probes and the upgrade program. This paper highlights some of the selected results.

© The Authors, published by EDP Sciences, 2018



This is an Open Access article distributed under the terms of the Creative Commons Attribution License 4.0, which permits unrestricted use, distribution, and reproduction in any medium, provided the original work is properly cited. (<http://creativecommons.org/licenses/by/4.0/>).

Figure 90: The screen-shot of the online copyright statement of EPJ Web of Conferences.

CITED LITERATURE

1. T. Matsui and H. Satz, “ J/ψ Suppression by Quark-Gluon Plasma Formation,” *Phys. Lett. B* **178**, 416 (1986). doi:10.1016/0370-2693(86)91404-8
2. sciencesprings, “Elementary particle in the Standard Model,” <https://sciencesprings.wordpress.com/2016/05/13/from-physicsworld-parallel-universe-search-focuses-on-neutrons/standard-model/>.
3. wikipedia, “Elementary particle and interactions in the Standard Model,” <https://or.wikipedia.org>.
4. BNL Nuclear Science, “Expansion of the Universe,” <http://rnc.lbl.gov/matis/BNL/upper-left.gif>
5. D. W. Duke and R. G. Roberts, “Deep Inelastic Scattering and Asymptotic Freedom: A Detailed Analysis and Confrontation,” *Nucl. Phys. B* **166**, 243 (1980). doi:10.1016/0550-3213(80)90227-8
6. C. A. Garcia Canal, “HERA has been closed, LHC is being opened: Near past and near future of particle physics,” *Braz. J. Phys.* **38**, 391 (2008). doi:10.1590/S0103-97332008000400004

7. F. Karsch, “Lattice QCD at high temperature and density,” *Lect. Notes Phys.* **583**, 209 (2002) [hep-lat/0106019].
8. C. Shen and U. Heinz, “The road to precision: Extraction of the specific shear viscosity of the quark-gluon plasma,” *Nucl. Phys. News* **25**, no. 2, 6 (2015) doi:10.1080/10619127.2015.1006502 [arXiv:1507.01558 [nucl-th]].
9. Czyz W, Maximon LC, *Annals Phys.* 52:59 (1969)
10. Glauber, R.J., “Lectures: in Theoretical Physics, ed. WE Brittin and LG Dunham,” New York: Interscience (1959).
11. Bia las A, Bleszy’nski M, Czy’z W. *Acta, Phys. Pol. B* 8:389 (1977)
12. Back BB, et al, *Phys. Rev. Lett.* 85:3100 (2000)
13. Arsene I, et al, *Nucl. Phys. A* 757:1 (2005)
14. Adcox K, et al, *Nucl. Phys. A* 757:184 (2005)
15. Back BB, et al, *Nucl. Phys. A* 757:28 (2005)
16. Adams J, et al, *Nucl. Phys. A* 757:102 (2005)

17. Ludlam TW, Pfoh A, Shor A. HIJET, “A Monte Carlo event generator for p nucleus and nucleus nucleus collisions,” A talk at BNL-51921 (1985)
18. Shor A, Longacre RS, Phys. Lett. B 218:100 (1989)
19. M. L. Miller, K. Reygers, S. J. Sanders and P. Steinberg, “Glauber modeling in high energy nuclear collisions,” Ann. Rev. Nucl. Part. Sci. **57**, 205 (2007) doi:10.1146/annurev.nucl.57.090506.123020 [nucl-ex/0701025].
20. M. Tanabashi et al. (Particle Data Group), Phys. Rev. D 98, 030001 (2018).
21. H. Fritzsch, “Producing heavy quark flavors in hadronic collisions-‘A test of quantum chromodynamics”, Physics Letters B, vol. 67, pp. 217–221, mar 1977.
22. V. Barger, W. Keung, and R. Phillips, “On psi and Upsilon production via gluons, Physics Letters B, vol. 91, pp.” 253–258, apr 1980.
23. V. Barger, W. Y. Keung, and R. J. N. Phillips, “Hadroproduction of J/ψ and Υ , Zeitschrift fur Physik C Particles and Fields,” vol. 6, pp. 169–174, jun 1980.
24. C. Chao-Hsi, “Hadronic production of J/ψ associated with a gluon,” Nuclear Physics B, vol. 172, pp. 425–434, jan 1980.

25. R. Baier and R. Ruckl, “Hadronic production of J/ψ and Υ : Transverse momentum distributions,” *Physics Letters B*, vol. 102, pp. 364–370, jun 1981.
26. E. L. Berger and D. Jones, “Inelastic Photoproduction of J/ψ and Upsilon by Gluons,” *Physical Review D*, vol. 23, pp. 1521–1530, apr 1981.
27. F. Abe *et al.* [CDF Collaboration], *Phys. Rev. Lett.* **79**, 572 (1997).
doi:10.1103/PhysRevLett.79.572
28. B. Gong, L.-P. Wan, J.-X. Wang, H.-F. Zhang, “Polarization for prompt J/ψ and $\psi(2S)$ production at the Tevatron and LHC.” *Phys. Rev. Lett.* 110, 042002 (2013).
arXiv:1205.6682[hep-ph]
29. M. Butenschoen, B.A. Kniehl, “ J/ψ polarization at Tevatron and LHC: nonrelativistic-QCD factorization at the crossroads.” *Phys. Rev. Lett.* 108, 172002 (2012). arXiv:1201.1872 [hep-ph]
30. K.-T. Chao, Y.-Q. Ma, H.-S. Shao, K. Wang, Y.-J. Zhang, “ J/ψ polarization at hadron colliders in nonrelativistic QCD.” *Phys. Rev. Lett.* 108, 242004 (2012). arXiv:1201.2675 [hep-ph]
31. E. Braaten and A. Nieto, “Next-to-leading order Debye mass for the quark - gluon plasma,” *Phys. Rev. Lett.* **73**, 2402 (1994) doi:10.1103/PhysRevLett.73.2402 [hep-ph/9408273].

32. H. Satz, “Colour deconfinement and quarkonium binding,” J. Phys. G **32**, R25 (2006)
doi:10.1088/0954-3899/32/3/R01 [hep-ph/0512217].
33. A. Adare *et al.* [PHENIX Collaboration], “Measurement of $\Upsilon(1S + 2S + 3S)$ production in
 $p + p$ and Au+Au collisions at $\sqrt{s_{NN}} = 200$ GeV,” Phys. Rev. C **91**, no. 2, 024913
(2015) doi:10.1103/PhysRevC.91.024913 [arXiv:1404.2246 [nucl-ex]].
34. K. Kovarik and T. Stavreva, “Probing gluon nuclear PDF with direct photon production
in association with a heavy quark,” arXiv:1107.3030 [hep-ph].
35. K. J. Eskola, H. Honkanen, V. J. Kolhinen and C. A. Salgado, “Global DGLAP fit analyses
of the npdf: Eks98 and hkm,” hep-ph/0302170.
36. K.J.Eskola, H.Paukkunen and C.A.Salgado, “Nuclear PDFs at NLO - status re-
port and review of the EPS09 results,” Nucl. Phys. A **855**, 150 (2011)
doi:10.1016/j.nuclphysa.2011.02.032 [arXiv:1011.6534 [hep-ph]].
37. B. Z. Kopeliovich, I. K. Potashnikova and I. Schmidt, Nucl. Phys. A **864**, 203 (2011)
doi:10.1016/j.nuclphysa.2011.06.024 [arXiv:1012.5648 [hep-ph]].
38. N. Brambilla, “NRQCD and Quarkonia,” eConf C0610161 (2006) 004, arXiv:hep-
ph/0702105 [hep-ph].

39. S. Gavin, M. Gyulassy, and A. Jackson, “Hadronic J/ψ suppression in ultrarelativistic nuclear collisions,” *Physics Letters B* 207 no. 3, (1988) 257 – 262.
<http://www.sciencedirect.com/science/article/pii/0370269388905710>.
40. S. Gavin and R. Vogt, *Phys. Rev. Lett.* 78, 1006 (1997).
41. A. Capella, A. Kaidalov, A. Kouider Akil, C. Gerschel, *Phys. Lett. B* 393, 431 (1997).
42. Z. w. Lin and C. M. Ko, “Upsilon absorption in hadronic matter,” *Phys. Lett. B* **503**, 104 (2001).
43. CMS Collaboration, S. Chatrchyan et al., “Indications of suppression of excited Υ states in Pb–Pb collisions at $\sqrt{s_{NN}} = 2.76$ TeV,” *Phys. Rev. Lett.* 107 (2011) 052302, [arXiv:1105.4894 \[nucl-ex\]](https://arxiv.org/abs/1105.4894).
44. S. Chatrchyan *et al.* [CMS Collaboration], “Observation of sequential Upsilon suppression in PbPb collisions,” *Phys. Rev. Lett.* **109**, 222301 (2012).
45. B. B. Abelev *et al.* [ALICE Collaboration], “Suppression of $\Upsilon(1S)$ at forward rapidity in Pb-Pb collisions at $\sqrt{s_{NN}} = 2.76$ TeV,” *Phys. Lett. B* **738**, 361 (2014) [doi:10.1016/j.physletb.2014.10.001](https://doi.org/10.1016/j.physletb.2014.10.001) [[arXiv:1405.4493 \[nucl-ex\]](https://arxiv.org/abs/1405.4493)].
46. S. Chatrchyan *et al.* [CMS Collaboration], “Event activity dependence of $Y(nS)$ production in $\sqrt{s_{NN}}=5.02$ TeV pPb and $\sqrt{s}=2.76$ TeV pp collisions,” *JHEP* **1404**, 103 (2014)

doi:10.1007/JHEP04(2014)103 [arXiv:1312.6300 [nucl-ex]].

47. L. Adamczyk *et al.* [STAR Collaboration], “Suppression of Upsilon Production in d+Au and Au+Au Collisions at $\sqrt{s_{NN}} = 200$,” Phys. Lett. B **735**, 127 (2014).
48. L. Adamczyk *et al.* [STAR Collaboration], “ Υ production in U + U collisions at $\sqrt{s_{NN}} = 193$ GeV measured with the STAR experiment,” Phys. Rev. C **94**, no. 6, 064904 (2016).
49. A. Adare *et al.* [PHENIX Collaboration], “ $\nu(1S + 2S + 3S)$ production in d+Au and p + p collisions at $\sqrt{s_{NN}} = 200$ GeV and cold-nuclear matter effects,” Phys. Rev. C **87**, no. 4, 044909 (2013).
50. AGS, “The Tandem Van de Graaff (Tandem), the Electron Beam Ion Source (EBIS) and the BNL Linear Accelerator (Linac)”, <https://www.bnl.gov/rhic/AGS.asp>
51. RHIC, “The Relativistic Heavy Ion Collider,” <https://www.bnl.gov/rhic/>
52. RHIC, “Twin accelerators,” <https://phys.org/news/2013-03-particles-science-big-benefits-society.html>
53. RHIC, “Superconducting Magnet at RHIC,” <https://www.bnl.gov/magnets/staff/gupta/-publications/pac99/tubr6.pdf>.

54. K.H. Ackermann et al. (STAR Collaboration), “STAR detector overview.” Nucl. Instr. Meth. A 499, 624 (2003).
55. M. Anderson *et al.*, “The Star time projection chamber: A Unique tool for studying high multiplicity events at RHIC,” Nucl. Instrum. Meth. A **499**, 659 (2003) doi:10.1016/S0168-9002(02)01964-2 [nucl-ex/0301015].
56. M. Anderson, R. Bossingham, F. Bieser, D. A. Cebra, E. L. Hjort, S. R. Klein, C. Q. Vu and H. Wieman, “A Readout system for the STAR time projection chamber,” Nucl. Instrum. Meth. A **499**, 679 (2003) doi:10.1016/S0168-9002(02)01965-4 [nucl-ex/0205014].
57. Kalman, R.E., “A New Approach to Linear Filtering and Prediction Problems,” Trans. ASME, J. Basic Eng., 1960, vol. 82 D, pp.35–45.
58. Kalman, R.E., “Contributions to the Theory of Optimal Control,” Bol. Soc. Mat. Mexicana, 1960, 5, pp. 102–119.
59. Kalman, R.E., “Mathematical Description of Linear Dynamical Systems,” SIAM J. Control, 1963, vol. 1, pp. 152–192.
60. Grigory, Presentation on IV International Conference on Particle Physics and Astrophysics: https://drupal.star.bnl.gov/STAR/system/files/Nigmatkulov_icppa2018_final.pdf

61. W. J. Llope *et al.*, “The TOFp/pVPD time-of-flight system for STAR,” Nucl. Instrum. Meth. A **522**, 252 (2004) doi:10.1016/j.nima.2003.11.414 [nucl-ex/0308022].
62. M. Shao *et al.*, “Beam test results of two kinds of multi-gap resistive plate chambers,” Nucl. Instr. Meth. A **492**, 344 (2002).
63. B. Bonner *et al.*, “A single Time-of-Flight tray based on multigap resistive plate chambers for the STAR experiment at RHIC.” Nucl. Instr. Meth. A **508**, 181 (2003).
64. STAR Collaboration, M. Beddo *et al.*, “The STAR barrel electromagnetic calorimeter,” Nucl. Instrum. Meth. A **499** (2003) 725–739.
65. D. Beavis *et al.*, “The STAR Heavy Flavor Tracker Technical Design Report,” <https://drupal.star.bnl.gov/STAR/starnotes/public/sn0600>.
66. G. Contin for STAR Collaboration, “The STAR Heavy Flavor Tracker and Upgrade Plan,” Quark Matter 2015 proceedings.
67. L. Ruan, *et al.*, “Perspectives of a Mid rapidity Dimuon Program at RHIC: A Novel and Compact Muon Telescope Detector,” J. Phys. G **36**, 095001 (2009).
68. W. J. Llope *et al.*, “The STAR Vertex Position Detector,” Nucl. Instr. Meth. A **759**, 23 (2014).

69. C. A. Whitten for STAR Collaboration, “The beambeam counter: A local polarimeter at star,” AIP Conference Proceedings 980 no. 1, (2008) 390–396.
70. STAR, “STAR Official Embedding Simulation Documentation,” <https://drupal.star.bnl.gov/STAR/comp/embedding>.
71. R. Brun, R. Hagelberg, M. Hansroul, J.C. Lassalle, “Geant: Simulation Program for Particle Physics Experiments. User Guide and Reference Manual,” CERN-DD-78-2-REV, CERN-DD-78-2.
72. STAR HIJING, “HIJING Simulation at STAR,” <https://www.star.bnl.gov/public/comp/simu/evgen/hijing.html>.
73. Yanfang, Liu, “Centrality Determination for p+Au Collisions at $\sqrt{s_{NN}} = 200$ GeV by the STAR Experiment,” <https://indico.cern.ch/event/433345/contributions/2358183/>.
74. C. Aidala *et al.* [PHENIX Collaboration], “Measurements of $\mu\mu$ pairs from open heavy flavor and Drell-Yan in p + p collisions at $\sqrt{s} = 200$ GeV,” [arXiv:1805.02448 [hep-ex]].
75. J. Adam *et al.* [STAR Collaboration], “J/ ψ production cross section and its dependence on charged-particle multiplicity in p + p collisions at $\sqrt{s} = 200$ GeV J/ ψ production cross section and its dependence on charged-particle multiplicity in p + p collisions at $\sqrt{s} = 200$ GeV,” Phys. Lett. B **786**, 87 (2018) doi:10.1016/j.physletb.2018.09.029 [arXiv:1805.03745 [hep-ex]].

76. STAR Collaboration, “Centrality and Glauber MC simulation in Run10 and Run11 Au + Au collisions,” <https://www.star.bnl.gov/protected/common/common2010/centrality/200GeV/index.html>.
77. L. Adamczyk *et al.* [STAR Collaboration], “Dielectron azimuthal anisotropy at mid-rapidity in Au+Au collisions at $\sqrt{s_{NN}} = 200$ GeV,” *Phys. Rev. C* **90**, no. 6, 064904 (2014) doi:10.1103/PhysRevC.90.064904 [arXiv:1402.1791 [nucl-ex]].
78. Z. Ye [STAR Collaboration], “ Υ measurements in p+p, p+Au and Au+Au collisions at $\sqrt{s_{NN}} = 200$ GeV with the STAR experiment,” *Nucl. Phys. A* **967**, 600 (2017). doi:10.1016/j.nuclphysa.2017.06.040
79. A. D. Frawley, T. Ullrich and R. Vogt, “Heavy flavor in heavy-ion collisions at RHIC and RHIC II,” *Phys. Rept.* **462**, 125 (2008).
80. M. Aaboud *et al.* [ATLAS Collaboration], “Measurement of quarkonium production in proton–lead and proton–proton collisions at 5.02 TeV with the ATLAS detector,” *Eur. Phys. J. C* **78**, no. 3, 171 (2018) doi:10.1140/epjc/s10052-018-5624-4 [arXiv:1709.03089 [nucl-ex]].
81. Wadut Shaikh, Biswarup Paul [ALICE Collaboration], “ Υ production in p+Pb Collisions at 8.16 TeV with ALICE at the LHC,” <https://indico.cern.ch/event/656452/contributions/2859762/attachments/1647543/>

2633723/QM2018_Upsilon_pPb8TeV_Wadut.pdf.

82. X. Du and R. Rapp, “In-medium bottomonium production in proton-nucleus collisions at RHIC”, Private Communication, 2018, arXiv:1808.10014 [nucl-th].
83. T. Todoroki [STAR Collaboration], “Measurements of charmonium production in p+p, p+Au, and Au+Au collisions at $\sqrt{s_{NN}} = 200$ GeV with the STAR experiment,” Nucl. Phys. A **967**, 572 (2017) doi:10.1016/j.nuclphysa.2017.04.020 [arXiv:1704.06251 [nucl-ex]].
84. F. Arleo and S. Peigne, “Heavy-quarkonium suppression in p-A collisions from parton energy loss in cold QCD matter,” JHEP **1303**, 122 (2013), and private communication.
85. T. Affolder *et al.* [CDF Collaboration], “Production of $\Upsilon(1S)$ mesons from χ_b decays in $p\bar{p}$ collisions at $\sqrt{s} = 1.8$ TeV,” Phys. Rev. Lett. **84**, 2094 (2000) doi:10.1103/PhysRevLett.84.2094 [hep-ex/9910025].
86. H. Woeri, “International Workshop on Heavy Quarkonium 2014,” <https://indico.cern.ch/event/278195/session/7/contribution/104/material/slides/0.pdf>.
87. B. Krouppa, A. Rothkopf and M. Strickland, “Bottomonium suppression using a lattice QCD vetted potential,” Phys. Rev. D **97**, no. 1, 016017 (2018), doi:10.1103/PhysRevD.97.016017, [arXiv:1710.02319 [hep-ph]].

88. X. Du, R. Rapp and M. He, “Color Screening and Regeneration of Bottomonia in High-Energy Heavy-Ion Collisions,” *Phys. Rev. C* **96**, no. 5, 054901 (2017), doi:10.1103/PhysRevC.96.054901, [arXiv:1706.08670 [hep-ph]].